RICE UNIVERSITY

Search for the anomalous chiral effects via charge-dependent azimuthal correlations in proton-nucleus and nucleus-nucleus collisions at the LHC

by

Zhoudunming Tu

A THESIS SUBMITTED
IN PARTIAL FULFILLMENT OF THE
REQUIREMENTS FOR THE DEGREE

Doctor of Philosophy

APPROVED, THESIS COMMITTEE:

Wei Li

Wei Li, Chair
Assistant Professor of Physics and
Astronomy

Frank Geurts
Associate Professor of Physics and
Astronomy

Stephen W. Semmes

Stephen Semmes
Noah Harding Professor of Mathematics

Houston, Texas

April, 2018

ABSTRACT

Search for the anomalous chiral effects via charge-dependent azimuthal correlations in proton-nucleus and nucleus-nucleus collisions at the LHC

by

Zhoudunming Tu

Searching for the chiral magnetic effect (CME) via the charge-dependent azimuthal correlations with respect to the reaction plane has been attempted in gold-gold collisions at the top Relativistic Heavy-Ion Collider (RHIC) energy $\sqrt{s_{_{NN}}} = 200$ GeV by the STAR Collaboration, and later in lead-lead collisions at the Large Hadron Collider (LHC) energy $\sqrt{s_{_{NN}}} = 2.76$ TeV by the ALICE Collaboration. The observation of the significant charge separation signal from the correlators was first believed to be consistent with a CME, where the strong initial magnetic field induced from the spectator protons can generate an electric current from the chirality imbalance in the chiral medium, and consequently lead to a charge separation effect for the final-state particles. One of the most important implications of searching for the CME, is to experimentally confirm the *chiral symmetry restoration* in heavy ion collisions at sufficiently high temperature. Taking a step further to the initial measurement of the CME, the STAR Collaboration at RHIC and the ALICE Collaboration at the LHC also measured the charge-dependent second-order Fourier coefficient as a function of event charge asymmetry, which has been found to be consistent with the scenario of a chiral magnetic wave (CMW), a long-wavelength collective excitation arising from the CME.

However, the experimental results from the STAR Collaboration were later found to be qualitatively consistent with some non-CME model calculations, which could be related to momentum conservation, local charge conservation coupled with anisotropy flow, and short-range correlations, e.g., jets and resonance decay. Due to the nature of the complicated background contribution in the conventional way of measuring the CME and CMW, the speculated background correlations have never been explicitly shown in the experimental data, which makes the question of whether there is an unambiguous CME signal a longstanding problem for the past decade. Motivated by the problem of the CME background, the work of this thesis is the *first attempt* of exploring the background correlation in the experimental data, with a novel idea of using the *small colliding systems*. In a high-multiplicity proton-nucleus (pA) collision, the magnetic field in the overlap region and its correlation with respect to the event plane angle, are expected to be much smaller than in nucleus-nucleus (AA) collisions. On the other hand, the azimuthal anisotropies of the final-state particles in small systems have been well established in the recent studies at the LHC, where a clear evidence of collectivity that is similar to AA collisions has been observed. Therefore, the small colliding systems, e.g., pA collisions, provide a perfect testing ground and baseline for searching the CME and its background correlations. In addition, new experimental strategies have been developed, e.g., correlators with respect to higher harmonics, and a stringent upper limit has been set on the possible CME signal at the LHC energy for both pA and AA collisions.

The contribution to the CME and CMW searches from the work of this thesis is highly significant in the community, where the quantitative measurements not only explicitly show the presence of backgrounds and set an upper limit on the CME at the LHC, but also provide a series of new measurements for the lower energy search. With a better understanding of the background correlations and new experimental approaches, the CME signal might be discovered in the upcoming isobaric run using the STAR detector at RHIC energy.

This is dedicated for my love, Estella Yu, and my parents, Jian Tu and Elin Zhou.

Contents

Chapter 1

Introduction

The fundamental questions how the universe came into being and what it is made of has always fascinated mankind. From those ancient eastern civilizations, *earth*, *water*, *fire*, and *wind*, have been thought to be their fundamental building "particles". Over the past hundreds of years, physicists came a long way to understand what the fundamental particles are, mostly how they interact with each other, and even have a hint about what happened billions of years ago. For example, the Standard Model precisely describes the interactions among elementary particles, e.g., quarks, leptons, and their force mediator bosons. Having been predicted more than 50 years ago, the Higgs boson was finally discovered at the Large Hadron Collider (LHC) [1, 2], a last piece of puzzle in the model, which explains the mechanism of how fundamental particles obtain their masses. Within the Standard Model, one of the pillars of our understanding is the theory of Quantum Chromodynamics (QCD) that quantitatively describes the underlying mechanism of *strong* interaction between quarks and gluons. A striking emergent phenomenon from QCD is that colored quarks and gluons are permanently confined within hadrons, known as *color confinement.* However, it is natural to ask whether we understand a complex system that is made of *many* quarks and gluons with strong interaction, which might be related to the early stage of the universe a few micro-seconds after the *Big Bang* [3]. The answer to this question is not entirely clear, because the first-principle QCD calculation is very hard to be performed in such complicated many-body system. To understand this strongly-interacting system of quarks and gluons, heavy ion physics has come into play and is mainly to study the macroscopic property of this system. In this Chapter, a brief description of QCD is introduced, followed by the basic idea of heavy ion physics. After that, a short experimental introduction on one of the key measurements of heavy ion physics, using the particle collider, will be reviewed.

1.1 Quantum Chromodynamics

As suggested by its name, Quantum Chromodynamics introduces a new fundamental degree of freedom, color charge, that quarks and gluons carry. There are a total of three colors, R, G, and B, behaving in an opposite way to the electric charge in Quantum Electrodynamics (QED) in terms of their dependence on the coupling. The original motivation of introducing the color charges was to remedy a statistics problem in constructing the wave function of Δ^{++}, a particle that has three u quarks with states of all spin up. Because of the requirement of anti-symmetric wave function of a fermion, a new degree of freedom, e.g., color, was needed. The three color charges of a quark form the fundamental representation of a $SU(3)$ symmetry group. The detail introduction of the theory are skipped in this thesis, but can be found otherwise in Refs [4–6].

One of the most important features of QCD, as opposed to QED, is the *asymptotic freedom*, demonstrated in Fig. 1.1. In QED, an electric charge would have a screening effect, caused by the vacuum polarization where the virtual electron-positron pair pops up and form a “cloud” of charge around it, resulting in the running coupling constant α_{EM} that is slowly decreasing as the separation of two charged particles increases. However, this qualitative behavior in QCD of the coupling constant, α_s, has been found to be opposite, where the α_s increases as the effective separation increases.

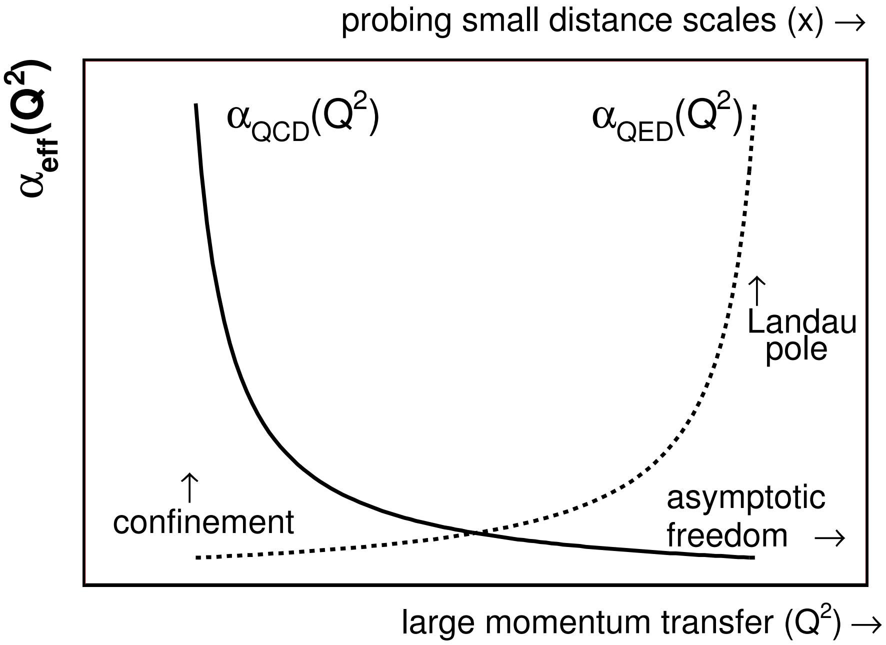

Figure 1.1 : Running coupling constant in QED and QCD [7].

This qualitative behavior of the coupling constant is so-called *asymptotically free.* As opposed to photons in QED, which do not carry electric charges, gluons in QCD carry bi-color charges and thus can be coupled to themselves. If a test color charge is placed in the vacuum, the vacuum polarization not only can split into quark and anti-quark ($q\bar{q}$) pair from a gluon, but also gluon-gluon pair. Effectively, this leads to an *antiscreening* effect, where an observer would essentially see “more” charges when far away and “less” when closer.

From the *asymptotic freedom* of the QCD, it is essentially much harder for two color charges, e.g., two quarks, to be separated more than 1 fm ($\alpha_s \approx 1$ at Λ_{QCD}) [8], which confines the quarks into a colorless bound state, so-called *color confinement.* Because of *color confinement*, no free quark has been found in nature. The potential energy of a $q\bar{q}$ would increase due to the strong coupling when they are being pulled away from each other, but instead of freeing the quarks, the potential energy would become large enough for them to break and instantaneously form new particles. This process can continue until the kinetic energy of the quarks are not enough to create new particles. Instead, the quarks and anti-quarks, with zero net color and low net momentum, will be bound together and form hadrons, e.g., baryon and meson.

1.2 Quark-Gluon-Plasma and QCD phase diagram

It is interesting to ask the question, is it ever possible to free the quarks and gluons from the hadronic matter? Based on *asymptotic freedom* in QCD, what happens if the hadronic matter gets squeezed into each other such that the mean distance between hadrons is on the order of much less than 1 fm? Or what happens if the hadronic matter gets heated up to very high temperature? To answer these questions, it leads us to the QCD phase diagram, shown in Fig. 1.2, which maps out the property of matter at different temperature and net baryon density. Therefore, at sufficiently high temperature or density, it is expected that the hadronic matter would be transitioned into a new state of matter, where deconfined quarks and gluons become the fundamental degrees of freedom, known as the "Quark-Gluon-Plasma" (QGP) [9–12]. In heavy ion physics, the main focus of the research is to explore the phase diagram of the QCD matter and understand the detail properties of the QGP.

In terms of the QCD phase diagram, there are still many questions and uncertainties that remained unknown, see Ref. [13] for a review. From numerical simulation using lattice QCD, a first-principle calculation, the high temperature and zero net baryon density region ($\mu_{\mathrm{B}} = 0$) has been found to be a *cross over*, the only thing that is derived from the first principle. For the low temperature and high baryon density region, phenomenological models [14] predict that there is a first-order phase

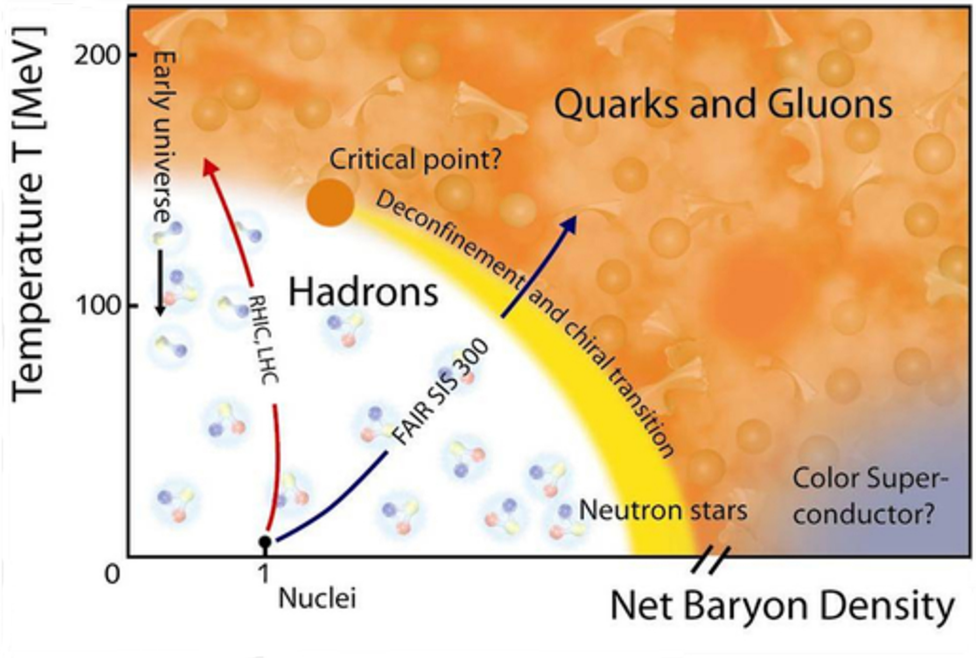

Figure 1.2 : QCD phase diagram.

transition. Therefore, somewhere in between, it is predicted that there should be a *Critical Point* that connects the cross over regime and the first-order phase transition between the hadronic matter and deconfined matter of quarks and gluons [13].

Chiral symmetry restoration In the non-Abelian group theory of QCD, the chiral symmetry is broken at zero or low temperature [15]. The spontaneous symmetry breaking of chirality effectively gives rise to the dynamical mass of quarks. Let's consider the following simple case. As known, the helicity is not conserved unless particles are massless and traveling at the speed of light. Because the gluon field is a vector field, the helicity conservation requires a left-handed quark (spin and momentum are anti-aligned) can only couple to a left-handed anti-quark and a right-handed quark with a right-handed anti-quark, when the mass of quark equals to zero. From quantum fluctuation, a real $q\bar{q}$ pair can pop up from the vacuum, where the two particles have opposite helicities. This already breaks the symmetry in the vacuum due to the interaction between left-handed quark and right-handed anti-quark or vice versa. If a test massless quark with right-handed (left-handed) helicity goes through the vacuum, it will immediately annihilate with the right-handed (left-handed) anti-quark, thus liberating the left-handed (right-handed) quark. From an observer point of view, this test quark spontaneously change its helicity and therefore it cannot be moving at the speed of light, and consequently gain its mass. Therefore, the mass generation of the quark is a consequence of the spontaneous chiral symmetry breaking. However, when the temperature increases, the vacuum condensate from real $q\bar{q}$ pair starts to vanish and the $q\bar{q}$ pair would have enough kinetic energy to be back into the vacuum, thus the helicity conserves as the quark would not be able to flip its helicity, and therefore chiral symmetry restored. In heavy ion physics, the signature of the chiral symmetry restoration might be able to be observed experimentally.

1.3 Relativistic heavy ion collisions

The QGP as introduced above, a deconfined state of matter with quarks and gluons, can be experimentally created and explored using relativistic heavy ion collisions. With powerful accelerators and particle colliders (see description in Chapter. 3), the heavy nuclei, e.g., gold (Au) and lead (Pb), can be accelerated to nearly the speed of light. Due to Lorentz contraction, the sphere-like heavy nuclei at rest would be contracted as a "pancake" with a transverse diameter of around 12-14 fm, and collide on each other at very high energies, creating a system that has very high temperature and energy density. A sequence of processes after the collision is described below [16], and is visualized in Fig. 1.3.

- Right after time $t = 0$, the maximum energy density occurs simply due to the

Lorentz contraction of the heavy nuclei, and the system is far from equilibrium. The transverse color field or charges that carried by the incident nuclei strongly interact with each other, producing particles like $q\bar{q}$ pair and gluons in the space between the two receding nuclei.

- At around 1 fm/c, the energy density of the system is still much higher than that of a typical hadron. At the LHC energy, the energy density can still be as high as 12 GeV per fm^3 [16], where lattice QCD shows that a thermalized system at a temperature of 300 MeV has around the same energy density, implying the quarks and gluons are far from independent. Instead, they are strongly interacting.

- Given by a strongly-interacting and possibly thermalized system (it is not in a consensus that whether it is at thermal equilibrium at all [17]), the system starts to develop a collective flow in the medium and expands like a hydrodynamic fluid with a very low shear viscosity over entropy density ($\eta/s \approx 1/4\pi$) [18,19].

- As the system expands and cools down, the average velocity of this fluid starts to build up and can be as fast as half of the speed of light. Until the system cools down to an energy density that is comparable to that of a hadron, e.g., 140 MeV, the quarks and gluons are combined together to form bound state of particles, therefore *hadronization* happens. At this point, it is known as *chemical freezeout*.

- Quarks and gluons are no longer present in the system, while the hadrons are just formed and relatively close to each other. They can still bounce around and scatter until they are very far apart, moving in their own direction without further interactions. At this moment, the system is regarded as *kinetic freezeout*.

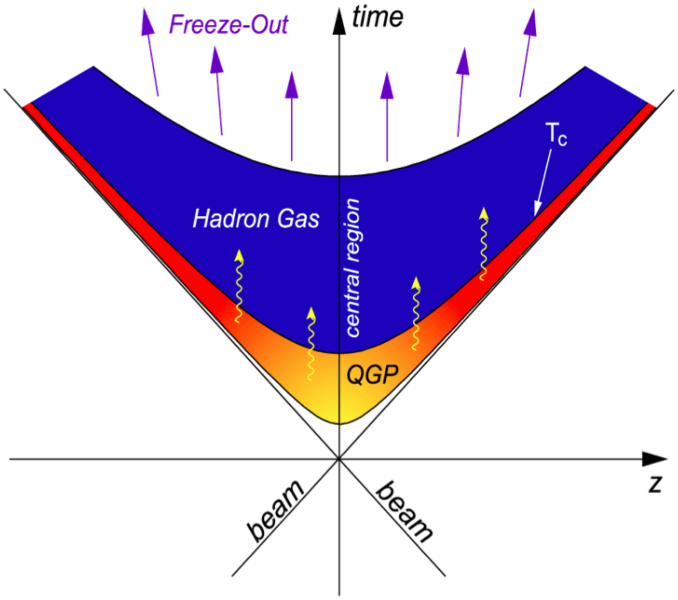

Figure 1.3 : QGP evolution.

Indeed, this is a very general description of what we believed about a typical heavy ion collision, however the knowledge of this process is far from complete, which is one of the main questions and challenges for heavy-ion physicists to find out. For example, in related to the work of this thesis, it is uncertain that at what time scale light quarks start to form, as well as that of the extremely strong magnetic field that is produced from the spectator protons (a more detail description of the magnetic field in the next section).

In Section. 1.3, it is only theoretically possible to create a QGP when the temperature and pressure are sufficiently high, but is there any experimental evidence? In other words, from relativistic heavy ion collisions, what observables or measurements can provide us the proof of the existence of a QGP? So far, a lot of experimental indications and indirect evidences led us to believe that there is indeed a strongly-interacting QCD medium with possible quarks and gluons degrees of freedom, which is consistent

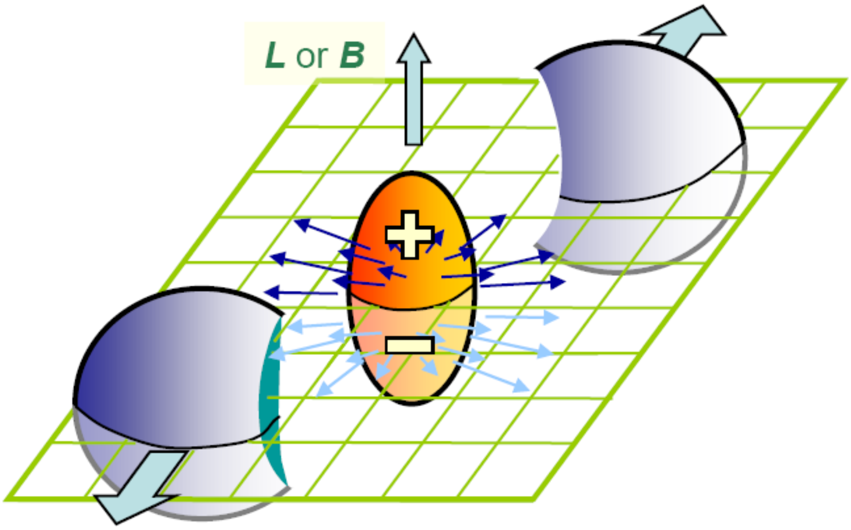

Figure 1.4 : Reaction plane in heavy ion collision [20].

with a QGP in terms of measurements, e.g., jet quenching [21–26], heavy quarkonia suppression [27–31], thermal photons [32–37], particle correlations [23–26,38–41], etc. For example, measurements of the Fourier harmonics of particle azimuthal distribution was believed to be one of the first evidences that the produced medium is a strongly-interacting system with possibly global or local thermal equilibrium. As two heavy nuclei collides, particularly in a noncentral collision (off-center collision like the one shown in Fig. 1.4), the overlap region is essentially an almond-shape football with an initial anisotropy in spatial space in the transverse plane. Due to this anisotropy, the expansion of the system with strongly-interacting particles would later transform the anisotropy from spatial space into momentum space, resulting in more particles produced along the short axis of this ellipse than the long axis in the transverse plane, illustrated in Fig. 1.4. The second-order Fourier harmonic, known as the elliptic flow (v_2), is ultimately a measure of this asymmetry of particle pro-

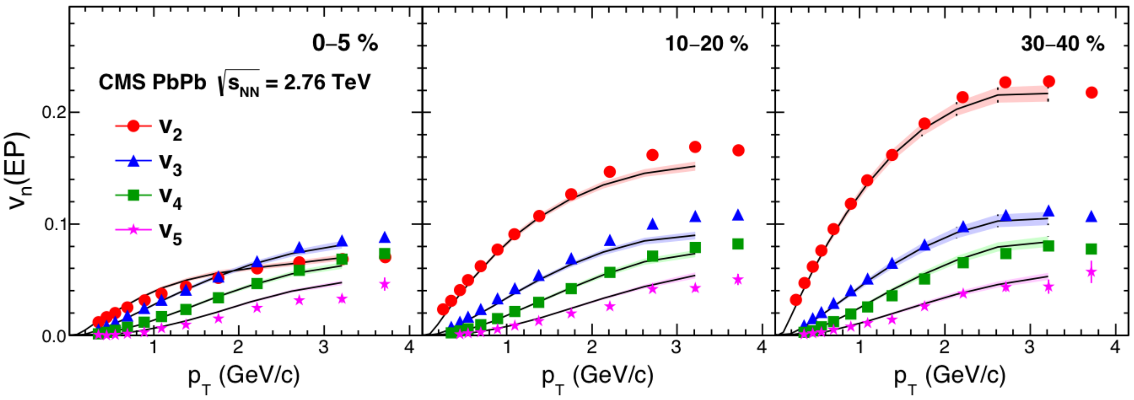

Figure 1.5 : Elliptic flow, v_2, as a function of p_{T} in PbPb collisions at $\sqrt{s_{NN}} = 2.76$ TeV at the LHC using CMS detector, together with a calculation based on hydrodynamic model with a Glauber-like initial condition and $\eta/s \approx 0.2$ [42].

duction in the azimuthal direction. In addition, together with hydrodynamic model, the result has been found to be consistent with a scenario that the medium has a very low shear viscosity over entropy density (an example of this study of using hydrodynamic models and compared with data is shown in Fig. 1.5 [42]), implying the system behaves like a "perfect" fluid. Not only the flow measurements point us to the direction of a strongly-interacting QGP, there are also many other observables and experimental efforts that indicate an agreement with this scenario. See Refs. [23–26] for a more complete experimental review. In particular, an exotic phenomenon of the chiral anomaly and the strong initial magnetic field is the focus of this thesis, which will be introduced in the next Chapter.

Chapter 2

Anomalous chiral effects in nuclear collisions

2.1 Introduction to anomalous chiral effects

In heavy ion collisions, the nucleons that are not participating the collision are regarded as *spectators*, as opposed to those *participants* that do participate in the collision. The spectator protons from the two incident nuclei, passing by each other close to the speed of light, generate two electric currents in opposite direction along the beam axis. Therefore, in the overlap region shown in Fig. 1.4, there is a very strong but time-dependent magnetic field up to 10^{15-20} Gauss pointing perpendicular to the reaction plane [43]. The magnitude of this strong initial magnetic field could be the strongest magnetic field so far in the observable universe. Regarding the formation and expansion of the QGP, effects that are related to the magnetic field are of extreme interests in heavy ion physics [44–48].

It has been predicted that the *Parity* (P) and *Charge-conjugate Parity* (CP) symmetry could be violated in strong interaction in local space-time due to the nontrivial topological gluon fluctuation in QCD vacuum [49–52]. These gluon fields, can do something very distinct to the chiral fermions, where they can change the chirality of the particles, namely transforming left- into right-handed fermion or vice-versa. In particular, the axial chiral chemical potential, μ_5, which is proportional to the difference in the number of left-handed and right-handed fermions, is used to characterize the imbalance of chirality in a system of fermions. This local symmetry

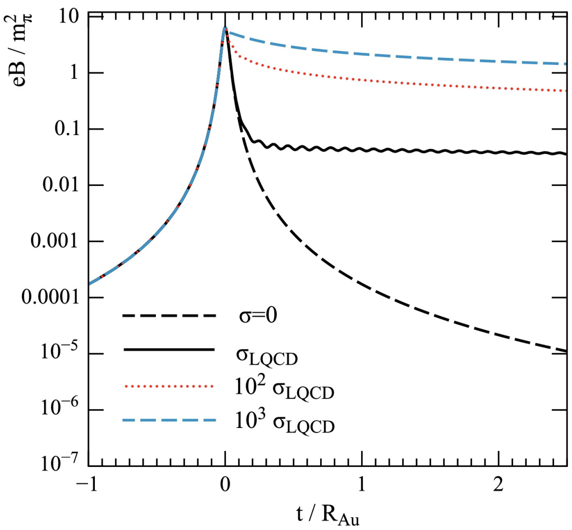

Figure 2.1 : Magnetic field induced by spectator protons in heavy ion collisions, in terms of the ratio to the pion mass, is shown as a function of time (scaled by the radius of gold nuclei) with different input electrical conductivities [43].

breaking is caused by the chiral anomaly [53, 54]. In heavy ion collisions, the quarks that produced in the QGP with chiral symmetry restoration, provide a perfect and unprecedented opportunity of studying this exotic phenomenon of local P and CP violation, via its interaction to the chiral quarks and the strong external magnetic field. In Fig. 2.1, the time-dependent magnetic field from the collisions, expressed in terms of the ratio with respect to the pion mass squared, is shown with different input values of electrical conductivity of the medium. As a consequence of this strong magnetic field, an electric current can be induced, which is forbidden by classical electrodynamics [55]. However, due to the nature of a chiral medium (e.g., QGP), it can be expressed as [56–58],

$$\vec{J} = \sigma_5 \vec{B}, \tag{2.1}$$

where the σ_5 is the chiral magnetic conductivity and is proportional to the μ_5. Finally,

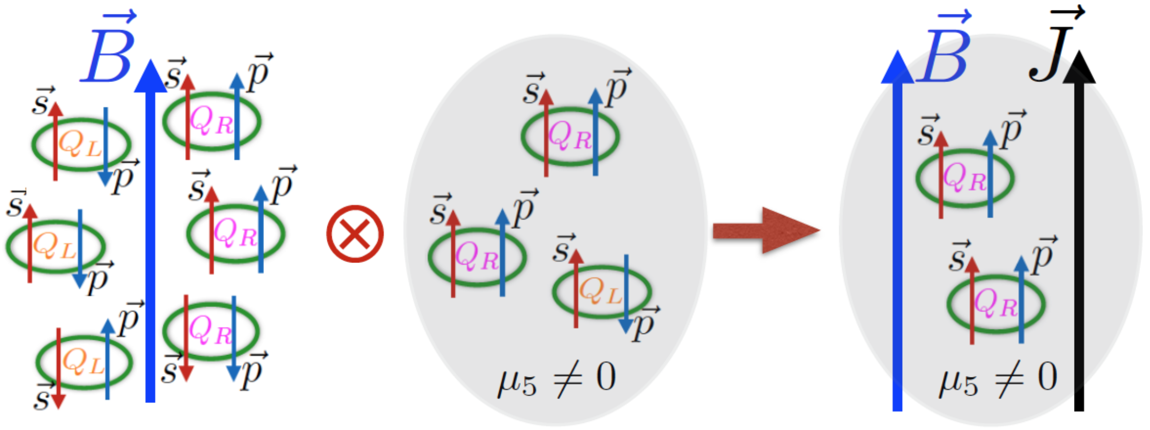

Figure 2.2 : Illustration of the CME. To be specific, the illustration is for just one kind of massless quarks with positive electric charge and for the case of $\mu_5 > 0$. For quarks with negative electric charge the quark current $\vec{J}$ is generated in the opposite direction (owing to the opposite spin polarization) but their contribution to the electric current would be the same as that from positively charged quarks. For $\mu_5 < 0$ the current will flip direction. [55]. Note that the convolution sign indicates the interplay between a global chirality conserved state with a magnetic field, and a local domain (indicated by the gray area) of chirality imbalance, resulting in an electric current in this local domain.

the electric current would result in an electric dipole of the QGP, and final-state particles with different charge signs would be separated with respect to the reaction plane, known as the "Chiral Magnetic Effect" (CME). The CME mechanism can be simplified in this following example.

In Fig. 2.2, let's assume the $\mu_5 > 0$, meaning there are more right-handed quarks than left-handed quarks (assuming quarks carry positive charge). Due to the spin polarization where the spin of the particle tends to align with the magnetic field ($\vec{B}$), it creates a correlation between the momentum of particles and the magnetic field. Therefore, the right-handed quarks will move along the $\vec{B}$-field, and because quarks also carry electric charge, it will lead to an electric current that pointing to the same direction as the $\vec{B}$-field. This also applies to quarks with negative electric charge,

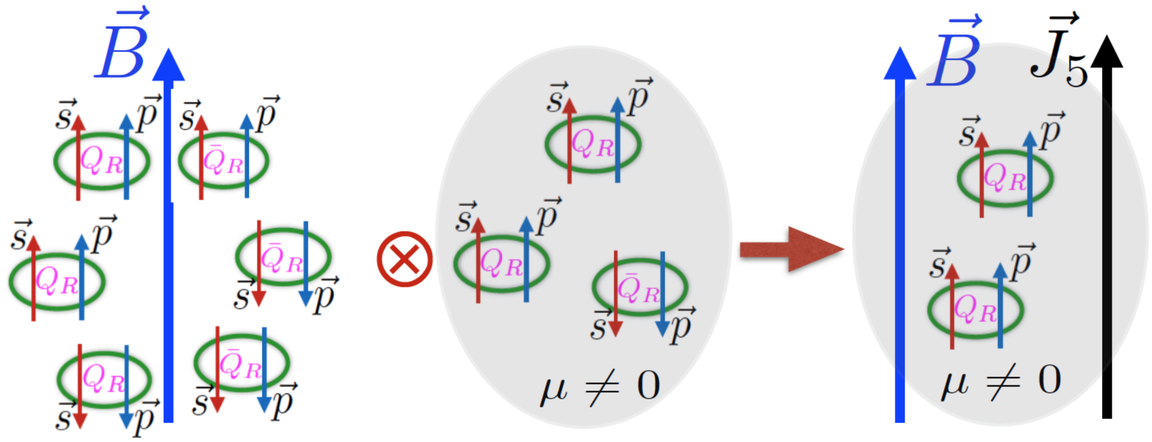

Figure 2.3 : Illustration of the CSE. To be specific, the illustration is for just one kind of right-handed (RH) quarks(with positive charge) and their anti-quarks (with negative charge) and for the case of $\mu > 0$ (i.e. more quarks than anti-quarks). For left-handed (LH) quarks (and anti-quarks) the LH quarks' current is generated in the opposite direction but their contribution to the axial current $\vec{J}_5$ would be the same as that of RH quarks. For $\mu < 0$ the current will flip direction. [55].

where the negatively-charged particles anti-align with the $\vec{B}$-field, and consequently move to the opposite direction of the $\vec{B}$-field but generate the same electric current just as the same as the positively-charged particles moving along the $\vec{B}$-field direction.

For each chiral fermion, in this case quark, it has corresponding vector current and axial current, J^μ and J_5^μ, respectively. In a similar fashion, instead of the vector current (electric current), the axial current (chiral charge current) can also be generated by an external magnetic field, which is a complementary phenomenon to the CME, known as the "Chiral Separation Effect" (CSE) [59,60]. Thus it can be expressed as,

$$\vec{J} = \sigma_s \vec{B}. \tag{2.2}$$

where σ_s is the CSE conductivity and is proportional to the (nonzero) vector chemical potential μ (instead of μ_5). A similar process of the CME can be applied for CSE, shown in Fig. 2.3.

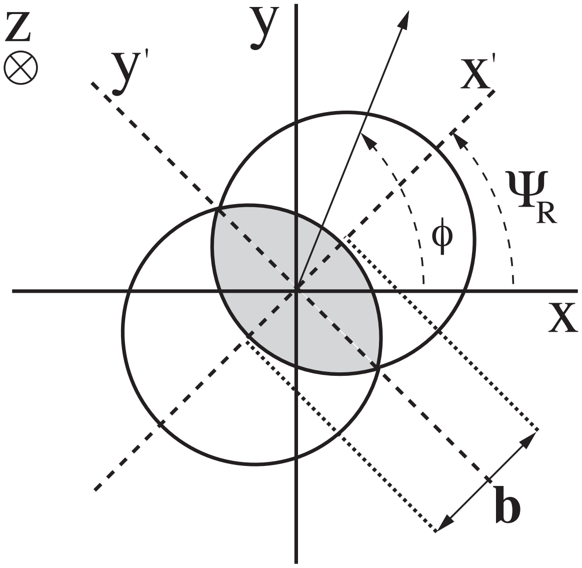

Figure 2.4 : The reaction plane angle Ψ_{R}, defined by the impact parameter direction with respect to X axis, is shown when the two heavy nuclei collide in a noncentral collision.

With this two complementary chiral effects, it is not hard to expect the coupling of these two and the collective excitation they form. The collective process can start with an axial density fluctuation, which implies a locally nonzero axial chiral chemical potential (μ_5) that leads to a CME current $\vec{J}$. The vector current will transport the vector charge (electric charge) along the $\vec{B}$-field direction, causing a fluctuation in the vector density locally. Similarly, this nonzero vector chemical potential would lead to a CSE current $\vec{J}_5$. This process then repeats over and over again, and mutually induces each other between the vector and the axial current. As a result, these density fluctuations propagate along the $\vec{B}$-field, forming a collective wave, known as the "Chiral Magnetic Wave" (CMW) [61, 62].

How to measure CME? Experimentally, the detection technique of these phenomenon was firstly proposed by Ref. [63]. The direct measurement of the CME is a challenge, because the μ_5 can be either positive or negative event-by-event and the nature of this fluctuation would result in an average of zero over all events. Therefore, a technique of measuring the correlation among particles with different charge signs was invented. The charge separation can be characterized by the P-odd sine term (a_1) in a Fourier decomposition of the particle azimuthal distribution [63] (an example of event plane with defined coordinates are shown in Fig. 2.4):

$$\frac{dN}{d\phi} \propto 1 + 2\sum_n \big(v_n \cos[n(\phi - \Psi_{\mathrm{R}})] + a_n \sin[n(\phi - \Psi_{\mathrm{R}})]\big), \tag{2.3}$$

where $\phi - \Psi_{\mathrm{R}}$ represents the particle azimuthal angle with respect to the reaction plane angle Ψ_{R} (determined by the impact parameter and beam axis), v_n and a_n denote the coefficients of P-even and P-odd Fourier terms, respectively. Although the reaction plane is not an experimental observable, it can be approximated by the second-order event plane, Ψ_{EP}, determined by the direction of the beam and the maximal particle density in the elliptic azimuthal anisotropy. An azimuthal correlator proposed to explore the first coefficient, a_1, of the P-odd Fourier terms characterizing the charge separation [63] is:

$$\begin{aligned}\gamma_{112} \equiv \langle \cos(\phi_\alpha + \phi_\beta - 2\Psi_{\mathrm{EP}}) \rangle &= \langle \cos(\phi_\alpha - \Psi_{\mathrm{EP}}) \cos(\phi_\beta - \Psi_{\mathrm{EP}}) \rangle \\ &\quad - \langle \sin(\phi_\alpha - \Psi_{\mathrm{EP}}) \sin(\phi_\beta - \Psi_{\mathrm{EP}}) \rangle \,. \end{aligned} \tag{2.4}$$

Here, α and β denote particles with the same or opposite charge sign and the brackets reflect an averaging over particles and events. Assuming particles α, β are uncorrelated except for their individual correlations with respect to the event plane, the first term on the right hand side of Eq. (2.4) becomes $\langle v_{1,\alpha} v_{1,\beta} \rangle$, which is generally small and independent of charge [20], while the second term is sensitive to charge separation and can be expressed as $\langle a_{1,\alpha} a_{1,\beta} \rangle$, which can be measured.

The measurement of this charge-dependent correlator, is expected to be negative for same-sign (SS) pair and positive for opposite-sign (OS) pair with similar magnitude [63]. While it is possible that the correlator of SS or OS would be contaminated by background correlation, e.g., directed flow (v_1) and momentum conservation, the charge-dependent component after taking a difference between OS and SS is expected to be proportional to the CME signal [63].

How to measure CMW? The propagation of the CMW leads to an electric quadrupole moment, where additional positive (negative) charges are accumulated away from (close to) the reaction plane [62]. This electric quadruple moment is expected to induce a charge-dependent variation of the second-order anisotropy coefficient (v_2) in the Fourier expansion of the final-state particle azimuthal distribution. More specifically, the v_2 coefficient will exhibit a linear dependence on the observed event charge asymmetry [62], $A_{\mathrm{ch}} \equiv (N_+ - N_-)/(N_+ + N_-)$, where N_+ and N_- denote the number of positively and negatively charged hadrons in each event, as follows;

$$v_{2,\pm} = v_{2,\pm}^{\mathrm{base}} \mp r A_{\mathrm{ch}}. \tag{2.5}$$

Here $v_{2,\pm}^{\mathrm{base}}$ represents the value in the absence of a charge quadrupole moment from the CMW for positively (+) and negatively (−) charged particles, and r denotes the slope parameter. In the presence of a CMW, the difference of v_2 values between positively and negatively charged particles will be proportional to A_{ch}.

2.2 Initial experimental efforts and their possible backgrounds

Almost a decay ago, the observation of charge-dependent azimuthal correlations with respect to the event plane (it was denoted as reaction plane at the time) in gold-gold (AuAu) collisions at $\sqrt{s_{_{NN}}}$ = 200 GeV at RHIC was reported by the STAR

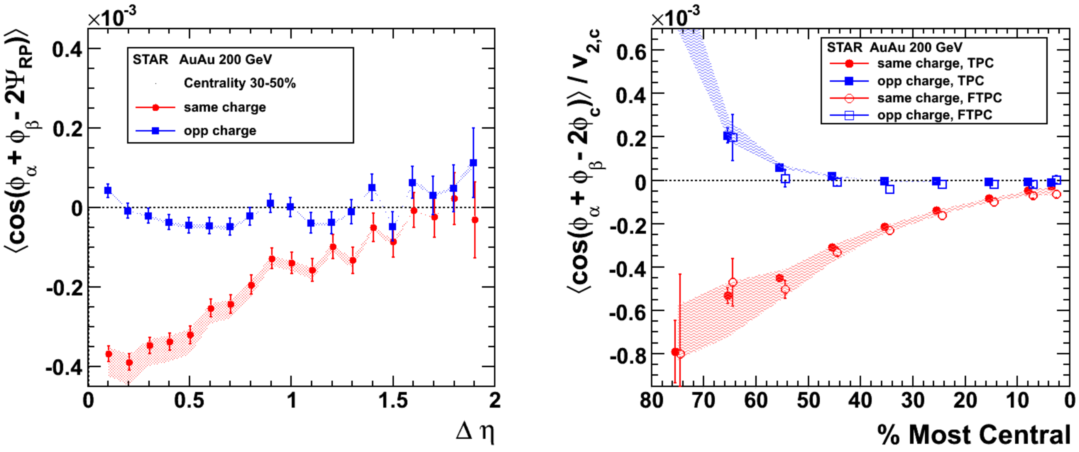

Figure 2.5 : The charge-dependent azimuthal correlator, γ, of same- and opposite-sign pairs are presented as a function of $\Delta\eta$ (left) and collision centrality (right) in AuAu collisions at $\sqrt{s_{NN}} = 200$ GeV, by STAR Collaboration [20].

Collaboration [20]. The result, shown in Fig. 2.5, presents a clear charge-dependence between SS and OS particles, as a function of the pseudorapidity separation of the two particles of interest. In addition, for the entire detector phase-space they can measure, the charge-dependent signal was also found to be dependent on the collision centrality (centrality is defined as the fraction of the total inelastic cross section, with 0% denoting the most central collisions), where the signal becomes larger in peripheral events. Most of these significant observations were in line with the scenario of a CME, because the nature of the fluctuations from vector and axial charge density in the QGP is expected to be short range and the magnitude of the magnetic field is larger in peripheral events than in central. A few years later, a similar measurement has been attempted by the ALICE Collaboration, where the same experimental observation was found with very weak energy dependence [64], shown as in Fig. 2.6.

However, right after the initial observation of the charge-dependent signal from STAR Collaboration, it is argued by Refs. [65–67] that the observed signal is also

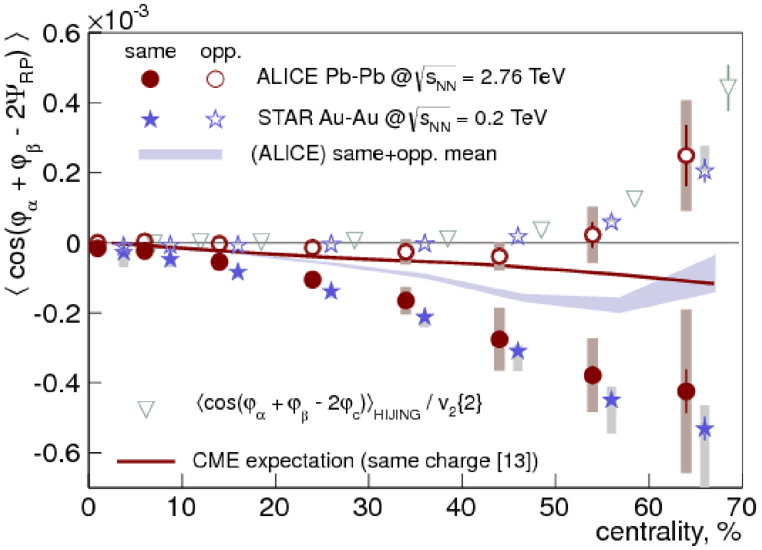

Figure 2.6 : The charge-dependent azimuthal correlator, γ, of same- and opposite-sign pairs are presented as a function of centrality in PbPb collisions at $\sqrt{s_{NN}} = 2.76$ TeV by ALICE Collaboration [64], and compared with the $\sqrt{s_{NN}} = 200$ GeV STAR data.

consistent with mechanisms that are not related to the CME. In particular, among the proposed mechanisms for background correlations, one source is related to the charge-dependent two-particle correlation from local charge conservation in decays of resonances or clusters (e.g., jets) [67]. By coupling with the anisotropic particle emission, an effect resembling charge separation with respect to the reaction plane can be generated. The observed characteristic range of the two-particle correlation in data is around one unit of rapidity, consistent with short-range cluster decays. In this mechanism of local charge conservation coupled with the elliptic flow, a background contribution to the three-particle correlator, γ_{112}, is expected to be [68]:

$$\gamma_{112}^{\text{bkg}} = \kappa_2 \left\langle \cos(\phi_\alpha - \phi_\beta) \right\rangle \left\langle \cos 2(\phi_\beta - \Psi_{\text{RP}}) \right\rangle = \kappa_2 \, \delta \, v_2. \tag{2.6}$$

Here, $\delta \equiv \langle \cos(\phi_\alpha - \phi_\beta) \rangle$ represents the charge-dependent two-particle azimuthal

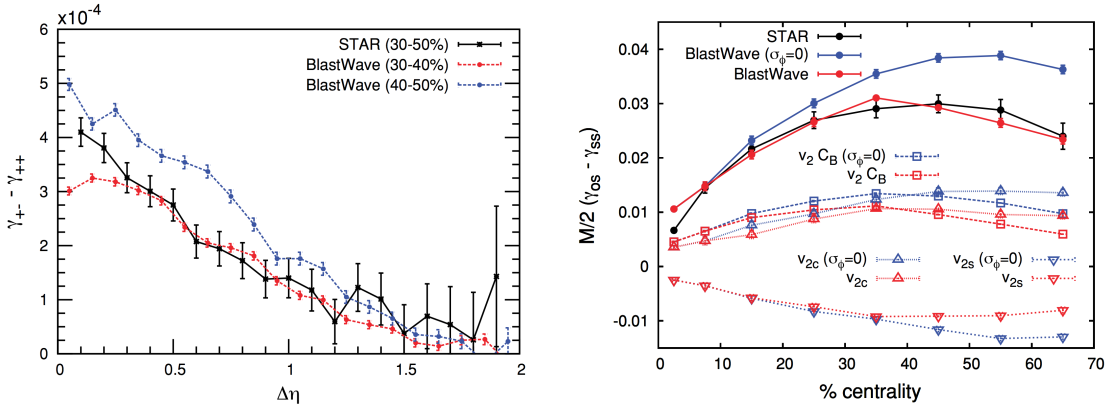

Figure 2.7 : Left: differential Parity Observable (γ-correlator) from STAR for 30-50% centrality (black solid) and blast-wave calculations for 30-40% (red dashed) and 40-50% centrality (blue dashed). The correlations decay in $\Delta\eta$ as balancing charges tend to be emitted in a narrow range of relative pseudorapidity. [67]. Right: Difference between opposite-sign and same-sign parity observable from STAR (black dots) and blast-wave calculations for realistic charge separation at freeze-out (red dots) and perfectly local charge conservation (blue dots). [67]

correlator and κ_2 is a constant parameter, independent of v_2, but mainly determined by the kinematics and acceptance of particle detection [68].

In Fig. 2.7, the charge-dependent correlator was found to be qualitatively consistent with the data with only local charge conservation and effects from particle interactions. For example, resonances decay conserves electric charge locally, and in principle, they should not have a preferred direction. However, if the system has a strong anisotropy flow, the resonances would be more likely to be squeezed in the in-plane direction than out-of-plane. Consequently, the decay particles that carry electric charge (mostly opposite charge) would be emitted in the (second-order) event plane. This mechanism will lead to a similar charge-dependent signal (OS-SS) using the Eq. 2.4, but not necessarily the individual OS and SS correlators [67]. The underlying correlations of the individual correlators from Eq. 2.4 are complicated, and can be related to many different physics, which is not a complete surprise for the

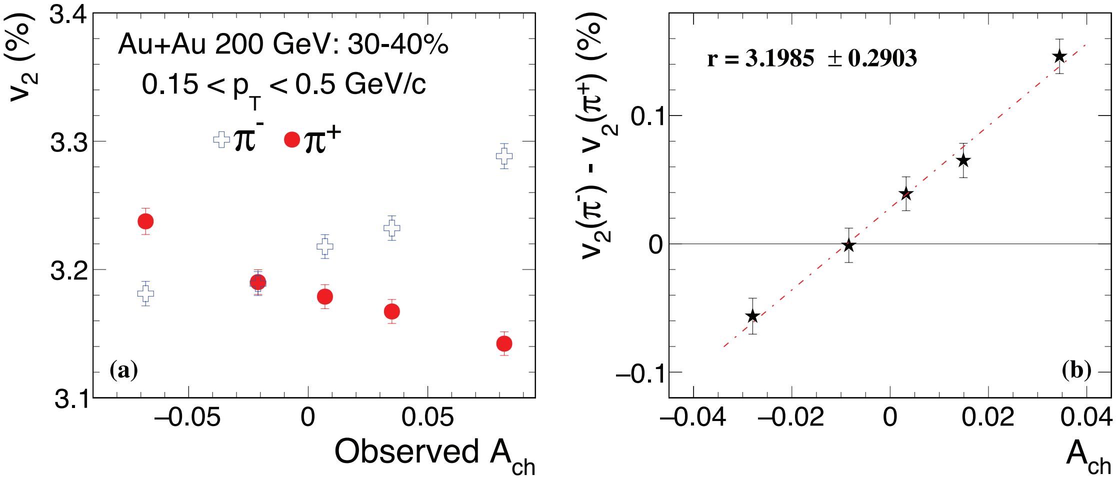

Figure 2.8 : The second-order Fourier harmonics, v_2, for positively- and negatively-charge pions (left) and their difference (right), are shown as a function of A_{ch} in AuAu collisions at $\sqrt{s_{NN}} = 200$ GeV in centrality range 30–40% by STAR Collaboration [69].

difference found in Ref. [67]. All of these studies, however, are based on theoretical models instead of experimental data.

On the other hand, similar experimental efforts have been attempted for studies of the CMW, using the technique that is described in Eq. 2.5. The charge-dependent second-order Fourier harmonic v_2 as a function of A_{ch} was measured in AuAu collisions at $\sqrt{s_{NN}} = 200$ GeV by STAR Collaboration [69]. The linear dependence on A_{ch} of $v_2^- - v_2^+$, shown in Fig. 2.8, was consistent with the picture of a CMW. As indicated by Eq. 2.5, the slope parameter r is proportional to the CMW, where the r has been extracted by linear fits in different centrality from the STAR data shown in Fig. 2.9. The centrality dependence, again, is consistent with the interpretation of the CMW because of a larger magnetic field is expected in noncentral collisions. In addition, this study has been further investigated using different theoretical calculations, where only models with a CMW can describe the data.

Similarly, the ALICE Collaboration also has reported a study in searching for

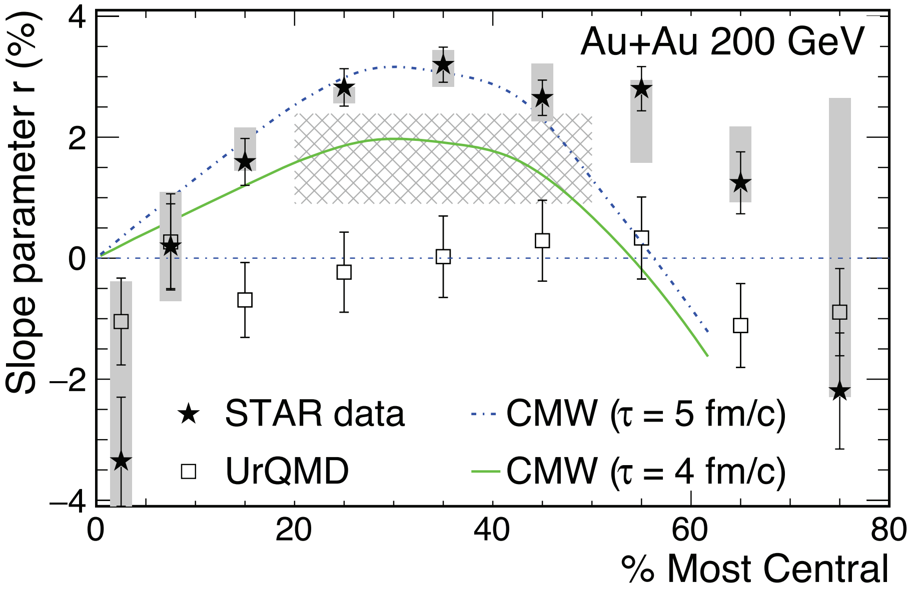

Figure 2.9 : The slope parameters of the v_2 as a function of centrality are shown in AuAu collisions at $\sqrt{s_{NN}}$ = 200 GeV by STAR Collaboration [69], with UrQMD calculations and CMW predictions.

the CMW, using a slightly different technique without measuring the true A_{ch} [70]. Note that the A_{ch} was not corrected for tracking efficiency in the STAR analysis in Ref. [69]. The experimental observation is in an agreement with the STAR data, where a clear charge-dependent signal has been observed for the second-order three-particle correlator. In addition, the three-particle correlator for higher order harmonics have been calculated, and a much reduced signal was found comparing to the second-order. Therefore, it is a hint that the data might be contaminated by some background correlations, but the CMW signal still dominates. Finally, the ALICE analysis had a direct comparison with the STAR data on the slope parameter as a function of centrality, where reasonable agreement has been observed at mid-central events shown in Fig. 2.10.

Not very long after the experimental data was presented, it is proposed that

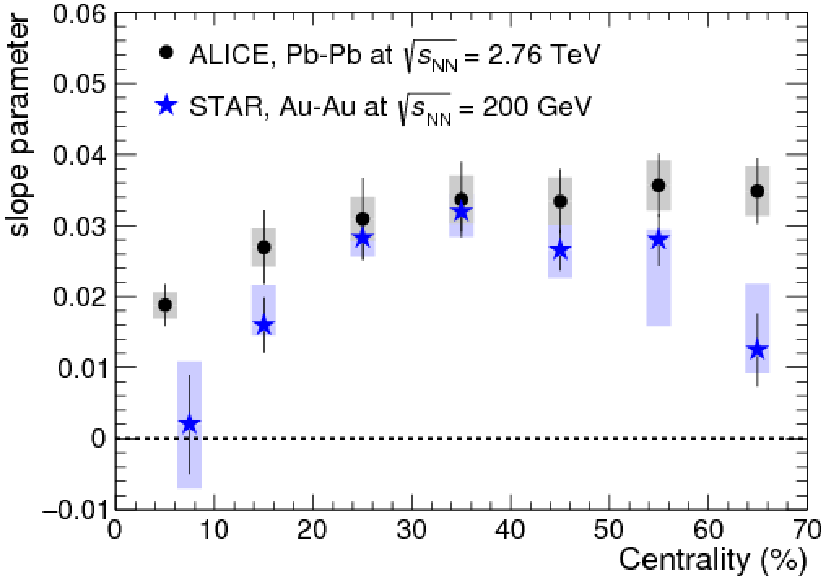

Figure 2.10 : The slope parameters of the v_2 as a function of centrality are shown in PbPb collisions at $\sqrt{s_{NN}} = 2.76$ TeV by ALICE Collaboration [70], and compared with the result from Ref. [69] at $\sqrt{s_{NN}} = 200$ GeV by STAR Collaboration.

(*again*) the experimental observation can be understood from an interplay between a local charge conservation effect and the detector acceptance [71, 72]. For example, it has been shown that local charge conservation in the decay of clusters or resonances can qualitatively describe the charge-dependent v_2 data [71]. Decay particles from a lower transverse momentum resonance tend to have a larger rapidity separation, resulting in a daughter more likely to fall outside the detector acceptance, leading to a nonzero A_{ch}. Hence, this process generates a correlation between A_{ch} and the average p_{T} of charged particles, and therefore also between A_{ch} and the v_2 coefficient, since v_2 depends on p_{T}. The local charge conservation mechanism also applies to all higher-order anisotropy Fourier coefficients (v_n). In Fig. 2.11, preliminary STAR data can be qualitatively reproduced by a hydro model with local charge conservation [71].

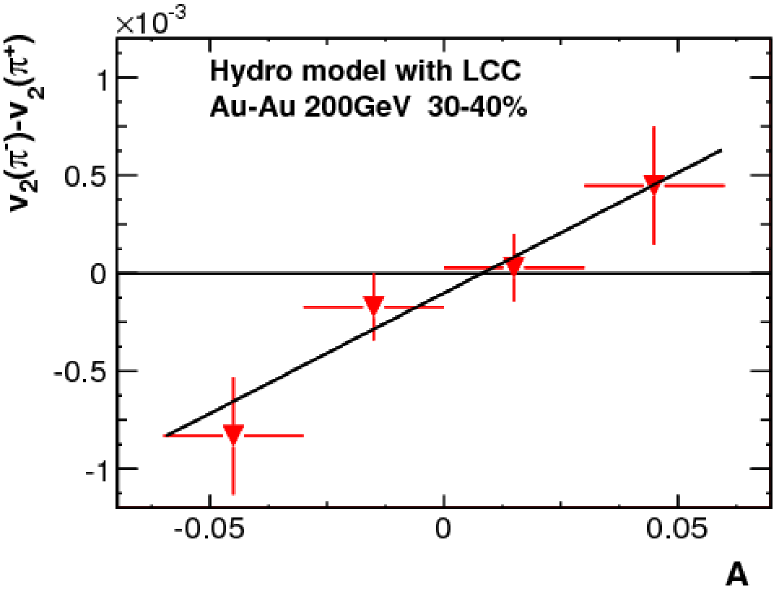

Figure 2.11 : The charge asymmetry dependence of π^+ and π^- elliptic flow coefficients in the hydrodynamic model followed by statistical emission with local charge conservation. [71]

2.3 Searching for anomalous chiral effects in small systems

The interpretation of the experimental results attempting to measure anomalous chiral effects, CME in particular, has been a decade-long standing problem due to its suspected background correlations. In terms of theoretical calculations, the difficulties are not only related to the strength of the CME signal, but also the detail mechanism of background correlations. For example, neither the μ_5 in the early stage of the collisions nor the lifetime of the initial magnetic field, can be directly calculated. On the other hand, short-range correlations, e.g., jets and resonance decays, are also complicated on their own. Therefore, in order to provide new insights into the understanding of anomalous chiral effects, new experimental approach is greatly needed.

Motivated by the idea of a classical electrodynamic homework problem from college physics, the magnetic field in the overlap region in a high-multiplicity proton-nucleus (pA) collision, by symmetry, is expected to be small if the proton goes through the center of the nucleus. As CME is a magnetic field-driven effect, the pA collision can be essentially become a system that only has pure backgrounds, effectively turning off the CME signal. Therefore, the underlying mechanism of the background can be studied experimentally, providing valuable informations to theoretical models. On the other hand, the comparison between pA and nucleus-nucleus (AA) collisions at the same multiplicity, can qualitatively show if there is a hint of the CME signal, where a larger charge separation signal is expected on top of the background correlations in AA collisions. If the magnitude of the charge-dependent signal is indeed *different* and larger in AA than in pA collisions, it is strongly suggesting a CME signal and the relative contribution of the signal and background correlations is possible to be determined. If the magnitude of the charge-dependent signal is similar between the two systems, then it is implying that the underlying mechanism in AA collisions is dominated by backgrounds instead of CME signal.

In the major work of this thesis, it is a first-time application of charge-dependent azimuthal correlation with respect to the event planes, and the A_{ch}-dependence of the second- and third-order Fourier harmonics, using proton-nucleus (pPb) data collected with the CMS detector at the LHC at $\sqrt{s_{_{NN}}} = 5.02$ TeV. High-multiplicity proton-proton (pp) and pPb collisions have been shown to generate large final-state azimuthal anisotropies, comparable to those in AA collisions [73–86]. However, the CME contribution to any charge-dependent signal is expected to be small in a high-multiplicity pPb collision, as the proton likely intersects the Pb nucleus at a small impact parameter. After a closer look from the Monte Carlo (MC) Glauber simulations, the magnitude of the magnetic field between pPb and lead-lead (PbPb) collisions, which is expected to be proportional to their ratio of impact parameters, has been found to be different by a factor of 3–4, shown in the left panel of Fig. 2.12. Consequently, the magnetic field in the proton-nucleus overlap region is expected to be smaller than in peripheral PbPb collisions at similar multiplicities [87]. Furthermore, based on MC Glauber calculations [88], the angle between the magnetic field direction and the event plane of elliptic anisotropy (approximated by the participant plane in MC Glauber simulation) is randomly distributed in pPb collisions, contrary to the case of PbPb collisions, which can be seen from Fig. 2.12 right. The high-multiplicity events in pPb collisions exhibit collective effects and bulk properties similar to those found in AA collisions [83, 85, 89] but possess very different strengths and configurations of the initial magnetic field. Thus, they can provide a new way, namely using the small system as a baseline, to explore the possible CME and CMW caused by the local strong parity violation.

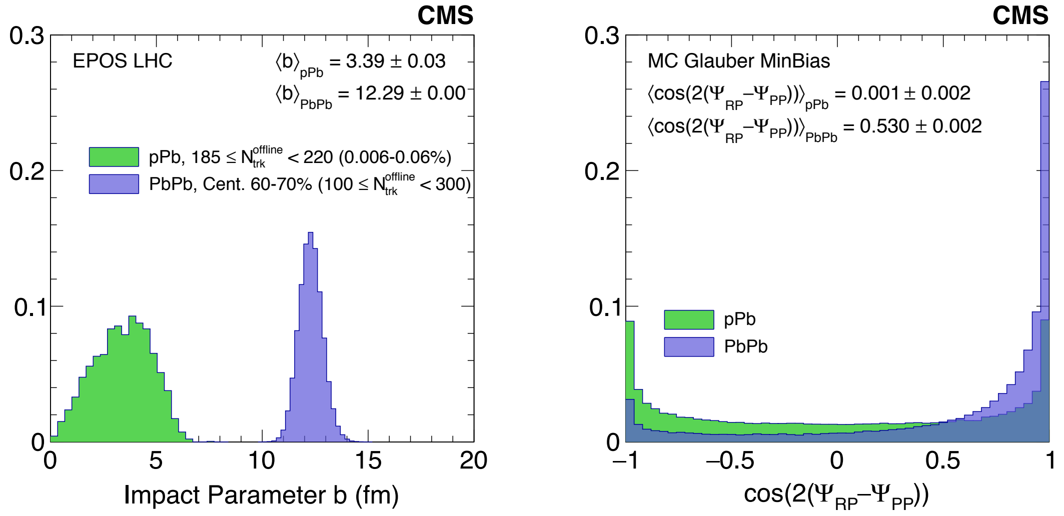

Figure 2.12 : Left: The impact parameter distributions from EPOS LHC simulation of pPb and PbPb collisions at $\sqrt{s_{_{NN}}}$= 5.02 TeV are presented. For pPb, the events with selection of top 0.006-0.06% of the multiplicity distribution are shown, equivalent to the multiplicity class $185 \leq N_{\text{trk}}^{\text{offline}} < 220$ in data. For PbPb, the events with centrality selection of 60-70% are shown, which is an equivalent to the multiplicity class $100 \leq N_{\text{trk}}^{\text{offline}} < 300$ in data. [87] Right: The cosine of the relative angle between the reaction plane, denoted as Ψ_{RP}, and the participant plane, denoted as Ψ_{PP}, from MC Glauber simulation of pPb and PbPb collisions at $\sqrt{s_{_{NN}}}$= 5.02 TeV are presented. [87]

2.4 New experimental strategies for quantitative analysis

Qualitatively showing the presence of background correlations can be achieved by using small systems, e.g., high-multiplicity pPb data at CMS. However, what is the underlying mechanism of the background correlation if it is found to be non-negligible in AA collisions? Although the background contribution from local charge conservation is proposed in Eq. (2.6) and has been long recognized [55, 67, 68], it is still not known to what extent background contributions account for the observed γ_{112} correlator. The main difficulty lies in determining the unknown value of κ_2 in a model-independent way. The other difficulty is to demonstrate directly the linear dependence on v_2 of $\gamma_{112}^{\mathrm{bkg}}$, which is nontrivial as one has to ensure the magnetic field, and thus the CME, does not change when selecting events with different v_2 values. Therefore, selecting events with a quantity that directly relates to the magnitude of v_2 is essential. Therefore, in this thesis, two new experimental approaches are introduced besides the new idea of using the high-multiplicity pPb data.

Higher-order harmonic three-particle correlator: in heavy ion collisions, the charge separation effect from the CME is only expected along the direction of the induced magnetic field normal to the reaction plane, approximated by the second-order event plane, Ψ_2. As the symmetry plane of the third-order Fourier term ("triangular flow" [90]), Ψ_3, is expected to have a weak correlation with Ψ_2 [91], the charge separation effect with respect to Ψ_3 is expected to be negligible. However, in terms of a background mechanism, e.g., local charge conservation effect coupled with anisotropic flow, it is not unusual to expect a reduced but nonzero charge-dependent correlation with respect to the Ψ_3, from a similar relation as in Eq. (2.6) with the third-order harmonics. By measuring the charge-dependent correlators with respect to both Ψ_2 and

Ψ_3, the unknown parameter κ_2 can be experimentally constrained as the parameter is expected to be harmonic-independent.

Event shape engineering (ESE): to establish directly a linear relationship between the γ_{112} correlators and v_n coefficients, the ESE technique [92] is employed. In a narrow centrality or multiplicity range (so that the magnetic field does not change significantly), events are further classified based on the magnitude of the event-by-event Fourier harmonic related to the anisotropy measured in the forward rapidity region. Within each event class, the γ_{112} correlators and v_n values are measured and compared to test the linear relationship. A nonzero intercept value of the γ_{112} correlators with a linear fit would reflect the strength of the CME.

With the implementation of a high-multiplicity trigger, the pPb data at $\sqrt{s_{_{NN}}} =$ 5.02 and 8.16 TeV sample gives access to multiplicities comparable to those in peripheral PbPb collisions (e.g., $\sim$55% centrality), allowing for a direct comparison of the two systems (in terms of final-state charged-particle multiplicity) with very different CME contributions in the overlap zone (See details for triggers in Chapter 4). Measurements of three-particle correlators, γ_{112} and higher harmonic correlator, and the two-particle correlator, are presented in different charge combinations as functions of the pseudorapidity (η) difference, the p_{T} difference, and the average p_{T} of correlated particles. Integrated over η and p_{T}, the event multiplicity dependence of three- and two-particle correlations is also presented in pPb and PbPb collisions. In pPb collisions, the particle correlations are explored separately with respect to the event planes that are obtained using particles with $4.4 < |\eta| < 5.0$ from the p- and Pb-going beam directions. The ESE analysis is performed for γ_{112} as a function of v_2 in both pPb and PbPb collisions.

2.5 Overview of this thesis

In Chapter 3, the LHC and CMS experiment are introduced, focusing on the most relevant detectors that are used in the work of this thesis. In Chapter 4, the introduction of triggers, e.g., the high-multiplicity trigger in pPb data, and data samples that were used in this work, are presented. In Chapter 5, the reconstruction algorithm of the physics objects used in this analysis and their performances, for example tracks and their efficiency, are going to be briefly mentioned with several related technical developments. In addition, the analysis selections on events and their classification in terms of charged-particle multiplicity are presented. In Chapter 6, the experimental strategies are described in detail, followed by the experimental results of searching for the CME. Similarly, the analysis techniques and the results of searching for the CMW are presented in Chapter 7. Finally, a conclusion is drawn and a future outlook is briefly discussed in Chapter 8.

Chapter 3

The Compact Muon Solenoid experiment at the Large Hadron Collider

The fundamental questions related to elementary particles, e.g., the Higgs boson, not only can be studied in terms of theoretical physics, but more importantly, via experiments using high energy particle collisions given by the enormous particle accelerator and colliders. Given by their tiny sizes, the elementary particles cannot simply be explored under the microscope and have a well defined experimental procedure to test their properties. Instead, particles like electron, proton, or even heavy nuclei, are needed to be collided into each other in order to study their fundamental properties, and the information of those collisions could be used to reveal the underlying physics of interactions among the elementary particles. In the analysis presented in this thesis, the experimental data were collected by one of the largest experiments in the world, the Compact Muon Solenoid (CMS) experiment at the Large Hadron Collider (LHC), European Organization for Nuclear Research (CERN). In this chapter, a brief introduction will be given for the LHC and the CMS experiment.

3.1 The LHC

At the foothill of Alps and Mount Jura, the LHC [93] accelerator ring is located at the boarder of Switzerland and France, close to the city of Geneva in Switzerland. The LHC is the largest and most powerful particle accelerator in the world. It is a two-ring superconducting hadron accelerator, which is the largest experimental facility at CERN. It is designed to collide proton beams at a highest energy of 7 TeV per beam (i.e. center-of-mass energy of $\sqrt{s}$= 14 TeV), and heavy ion beams with an energy of 2.76 TeV per nucleon for Pb nuclei. Instead of directly accelerating the particles from low to the maximum energy at the LHC, the process is optimized through a chain of acceleration from different boosting facility. A schematic overview of CERN accelerator complex is shown in Fig. 3.1, where the particles are accelerated as following:

- Proton: The protons from the H_2 source enter the LINAC2 linear accelerator and exit with an energy of 50 MeV. They are accelerated more in the Proton Synchrotron Booster (PSB) to 1.4 GeV. The Proton Synchrotron (PS) takes the protons from the PSB and continues to accelerate the protons to 25 GeV and injects them to the Super Proton Synchrotron (SPS). The SPS raises the proton energy again to 450 GeV and deliver them to the LHC ring where the maximum energy is achieved.
- Heavy ion: Currently, the LHC is capable to accelerate only the Pb and Xenon (Xe) nuclei. Starting from a source of vaporized lead, the Pb ions enter LINAC3 and get accelerated to an energy of 4.2 MeV. They are then collected and accelerated in the Low Energy Ion Ring (LEIR) to 72 MeV (shown in Fig. 3.2). After being injected to the PS from LEIR, the same route to maximum energy is taken as the protons.

There are a total of four experiments on the LHC ring, and altogether addressed as the *LHC experiments*. ATLAS and CMS are the two largest Collaborations in the world, focusing on high energy physics, e.g., Higgs physics, Standard Model physics, and physics beyond the Standard Model. ALICE experiment is the only dedicated

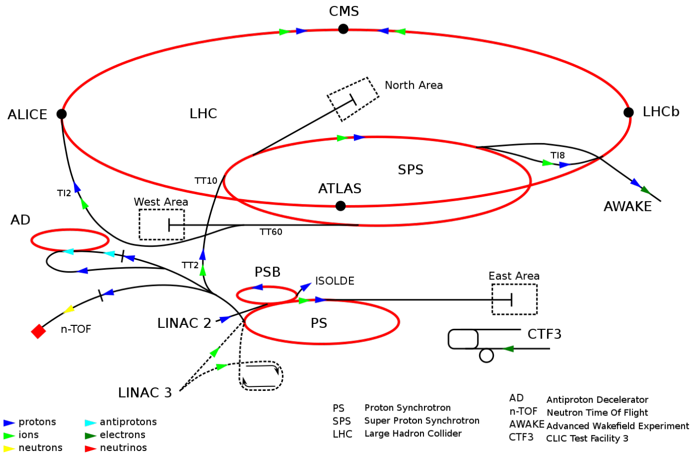

Figure 3.1 : The CERN accelerator complex [94].

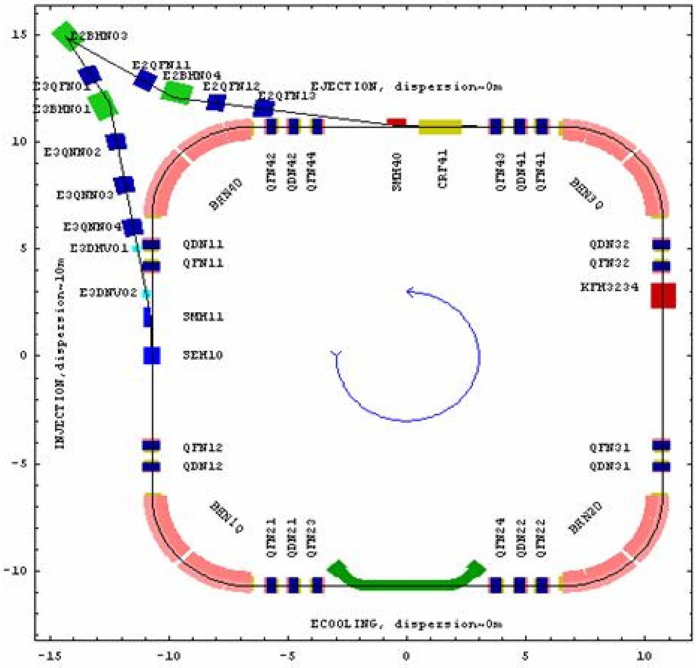

Figure 3.2 : The LEIR ion accelerator [94].

heavy ion experiment at the LHC, similar to the STAR experiment at RHIC at Brookhaven, NY, USA. LHCb is an experiment that focus on searching for the dark matter, and exotic particles. LHCb can be functioned as a collider mode or a fixed-target mode. In this thesis, the analysis are only based on the CMS experiment.

3.2 The CMS experiment

The CMS experiment locates at the furthest access point with respect to the main campus of CERN, the Meyrin site. It is a general purpose detector, whose main goal is to explore physics with very high energy, on the order of TeV. As part of its name, CMS is compact (still huge in size) with a solenoid structure of different layers, where sub-detectors are built in each layer for different purposes. Figure 3.3 shows a schematic view of CMS detector, the structure from inner to outer is formed including the following detector parts:

- The inner silicon tracking system, includes pixel and strip detector, can reconstruct particle's flight trajectory with good particle momentum and spatial resolution.
- The electromagnetic calorimeter (ECAL) allows accurate measurement of the energy of leptons and photons.
- The hadronic calorimeter (HCAL) allows precise measurement of the energy of hadrons.
- The solenoid magnet with a strong magnetic field of 3.8 Tesla (T) makes the determination of high momentum particle possible. It has the largest magnetic field in all collider experiments.
- The muon system provides excellent muon identification.

More detailed description on the sub-detector used in the analysis presented in this thesis will be given in Sec. 3.2.1 and Sec. 3.2.2.

A common coordinate system definition is crucial for data analysis using each sub-detector in a consistent way. The coordinate system adopted by CMS has a center at

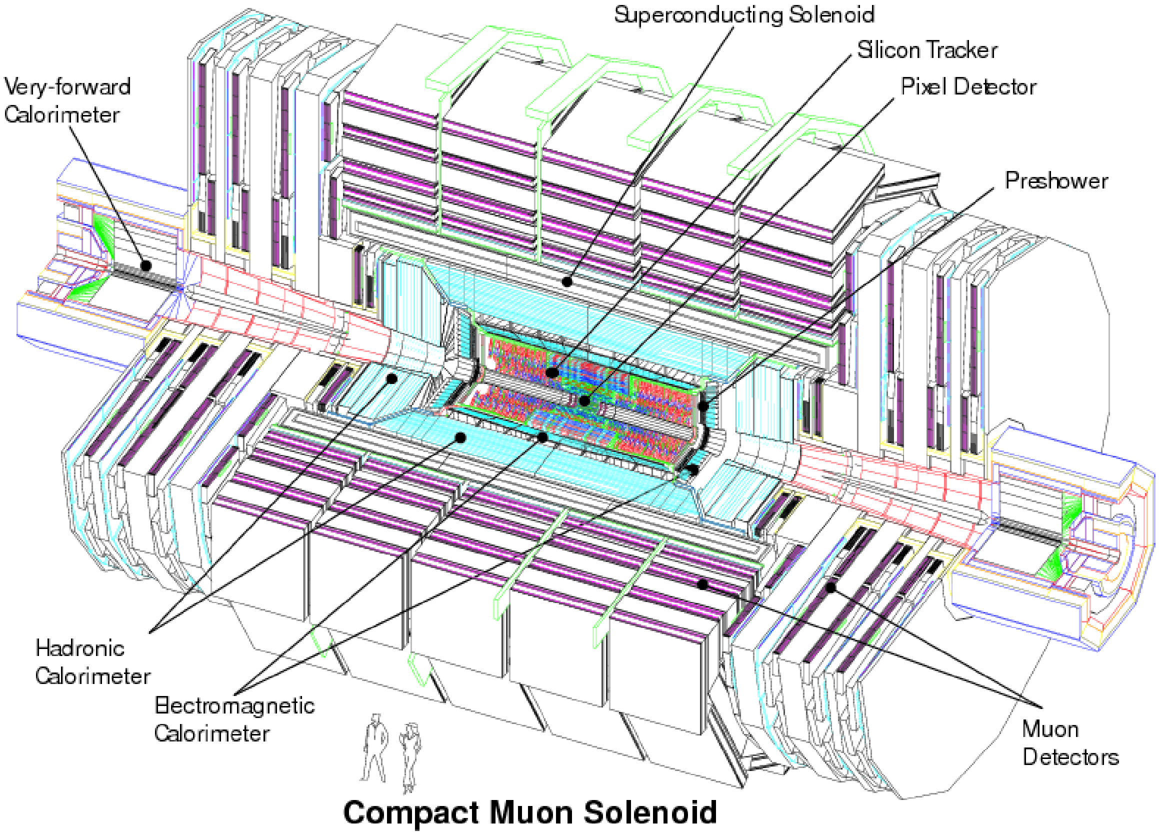

Figure 3.3 : A cutaway view of the CMS detector [95].

the nominal collision point inside the detector. The x-axis is defined to point towards the center of the LHC ring, the y-axis is defined to point straight upward and the z-axis is defined to point along counter clockwise direction of the LHC ring when looking from above. For the spherical coordinates, the azimuthal angle ϕ and the radial coordinate r are measured in the x-y plane relative to the x-axis. The polar angle θ is measured with respect to the z-axis.

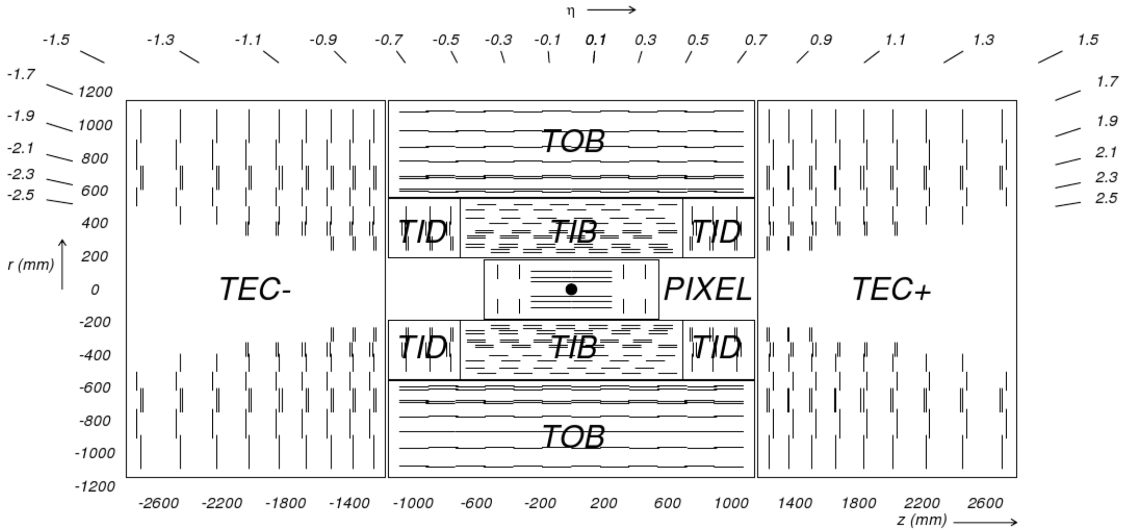

Figure 3.4 : View of the CMS tracker in the rz-plane [96]. Each line in the strip tracker represents a silicon strip detector, whereas lines in the pixel tracker represent ladders and petals on which the detectors are mounted in the barrel and endcaps, respectively.

3.2.1 Silicon tracking system

The silicon tracking system is designed for finding the position of collision vertex, trajectory of charged particles and their four-momentum information (described in Section 5.1). Therefore, it is the most important piece of detector for the analysis in this thesis.

The tracking system is composed of an inner silicon pixel detector and an outer silicon strip detector. Both of the two detectors cover a pseudorapidity range of $|\eta| < 2.5$. The layout of the tracking system is shown in Fig. 3.4.

Silicon pixel detector. The silicon pixel detector is the inner most detector of CMS, consisting of 3 concentric cylindrical barrel layers (in 2017 CMS has upgraded to 4 but the analysis in this thesis do not use the data recorded later than 2016) and two layers (upgraded to 3) of fan-blade disks at either end (shown in Fig. 3.5) [97]. It is designed to provide high precision 3D determinations of track trajectory points. The three barrel layers are located at radii of 4.3 cm, 7.3 cm and 10.2 cm to the interaction point, and have an active length of 53 cm. The two layers of disks cover the region between radii 4.8 cm and 14.4 cm, at longitudinal distance of 35.5 cm and 48.5 cm from the interaction point. This geometry layout ensures particle passage through 3 layers of detector in the region $|\eta| < 2.2$ and 2 layers of detector in the region $|\eta| < 2.5$. The entire pixel detector is composed of 1440 pixel modules with 65 million pixels. Each pixel, with an area of 100 μm × 150 μm, oriented in the azimuthal direction in the barrel and the radial direction in the forward disks. The electrons created by ionization during the passage of charged particles (track hits) in the barrel region are significantly Lorentz drifted in the 3.8 T magnetic field of CMS. This drift results in charge sharing on different readout modules. The weighted center of the charge distribution can be calculated from the analog readout which provides much better spatial resolution than a binary readout. To ensure the use of Lorentz drift at the forward disks, the blades are rotated by 20 degrees about their radial axes to produce a vertical component of magnetic field with respect to the electric field in the pixels. The entire pixel detector is operating at a temperature of -15°C to limit the impact of radiation damage and to minimize leakage current.

Silicon strip detector. As shown in Fig. 3.4, the silicon strip detector is composed of tracker inner barrel (TIB), tracker inner disk (TID), tracker outer barrel (TOB) and tracker outer endcap (TEC). A total of 15148 silicon strip modules with 10 million strips are arranged in 10 barrel layers extending outward to radii 1.1 m and 12 disks

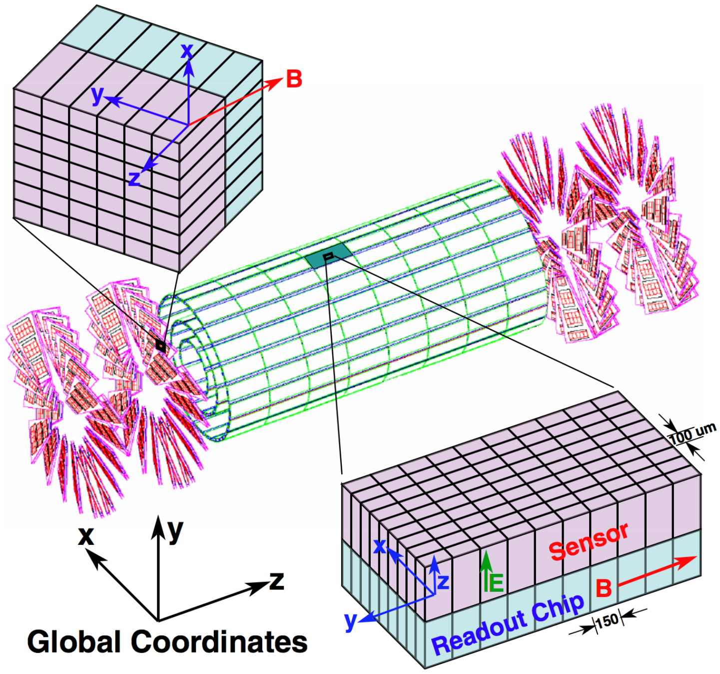

Figure 3.5 : View of the CMS silicon pixel tracker.

on each side of the barrel to cover the region $|\eta| < 2.5$. The active detector area is about 200 m^2 which makes it the largest silicon tracker ever built. Instead of providing 2D information of track hits in ϕ and z direction as the pixel detector, the silicon detector provides only 1D information. However, if two layers of strip detectors are placed on either side of a module with an angle, the double-sided module can obtain 2D information. Both single-sided (single line in Fig. 3.4) and double-sided modules (double line in Fig. 3.4) are used in the silicon detector at various physical locations, to maximize the performance with a limited material budget. Due to the complex layout of the silicon tracker, particle with different kinematics leave trajectories coincide with different number of layers. Particles passing through more layers have higher probability to be reconstructed then those passing through less layers, which results in a non-uniform track reconstruction efficiency as function of pseudorapidity which will be shown in Sec. 5.1.3.

These two sub-detectors are most important for the track and vertex reconstruction, which can be found in details in Chapter. 5.

3.2.2 Calorimeter system

The CMS calorimeter system aims to find the energies of all emerging particles in order to build up a complete picture of an event. The system provides precise measure of photon, electron and particles fragmented from a jet, and with the hermetic design which allows the measurements of missing transverse energy for neutrinos. From inner to outer, it is composed of Electromagnetic Calorimeter (ECAL) and Hadronic Calorimeter (HCAL).

Electromagnetic Calorimeter Used in finding Higgs and other new particles, electrons and photons are of particular interest among all particles emitted in a collision. The ECAL, which consists of a barrel section and two endcap disks, can measure the energy of particles deposited into the detector. In CMS, the ECAL is made of lead tungstate crystal, because it needs to handle the strong (3.8 T) magnetic field from the magnet and the high radiation level induced by collisions. It is highly transparent and produces light in fast, short and well-defined photon bursts in proportional to the energy of particle passing through, where the crystal is made of metal primarily but with a touch of oxygen in its crystalline form. The cylindrical barrel contains 61200 crystals formed into 36 modules with a depth of 25.8 radiation lengths (the crystal has radiation length of 0.89 cm). The flat endcap disks seal off the barrel at either end and are made up of around 15000 crystals with a depth of 24.7 radiation length. The barrel section covers $|\eta| < 1.479$ while the endcap disks extend the range to $|\eta| < 3$.

Hadron Calorimeter The HCAL measures the kinematic energy of hadrons. Using the technique of missing transverse energy, the presence of non-interacting neutral particles, e.g., neutrinos, can be measured indirectly using the HCAL. It is a sampling calorimeter made of repeating layers of dense absorber and tiles of plastic scintillator. An interaction occurs producing numerous secondary particles when a hadronic particle hits a plate of absorber. As the secondary particles flow through layers of absorbers they would produce more particles, which leads to a cascade. The particles pass through the alternating layers of active scintillators would cause them to emit light, which are collected up and amplified for a measurement of the initial particle's energy. Similar to ECAL, the HCAL consists of a barrel section and two endcap disks. The barrel reaches $|\eta|$ up to 1.3 while the endcap disks extend to $|\eta|$ of 3.

The HCAL has two hadronic forward calorimeters (HF) positioned at either end of CMS to cover the $|\eta|$ range of 2.9 to 5.2. The HF receives large fraction of particle energy contained in the collision, therefore the HF must be made very resistant to radiation. Thus, the HF was built with steel absorbers and quartz fibers where detection of signal is done with Cherenkov light produced in the fibers. The HF is very essential for heavy ion physics as it is used to select collision events at the trigger level (described in Chapter. 4), to determine centrality, and to reconstruct the event planes (described in Sec. 6.1).

Chapter 4

Data acquisition, triggers, and data samples

This chapter introduces the basic framework and mechanism of a triggering system at CMS experiment and its data acquisition (DAQ) system. Because of the high luminosity collisions and its increases over the years, trigger is one of the most important steps and selections on the data for all physics analysis, given by the rare collisions that are of interest and limitation on storing all the information for all events. In Sec. 4.1, the CMS triggering and DAQ system are briefly described, and followed by the details of triggers that are essential of making this analysis possible in Sec. 4.1.1 and Sec. 4.1.2. Finally, the data samples that are used, as well as some MC simulation samples, are briefly mentioned.

4.1 CMS triggering and data acquisition system

For nominal data taking, the LHC is delivering particle collision events at a rate on the order of MHz at the interaction point number 5 (P5), which is the location of the CMS experiment. Ideally, the more collisions the machine can deliver the better. However, in practice, it is impossible to store all the information with all collisions in the data storage center. Also, it is highly inefficient to record all the events because most of them are useless for physics analysis. Therefore, the triggering and DAQ system is to select events with a particular interest in real time, where only information that is useful for physics analysis would be stored.

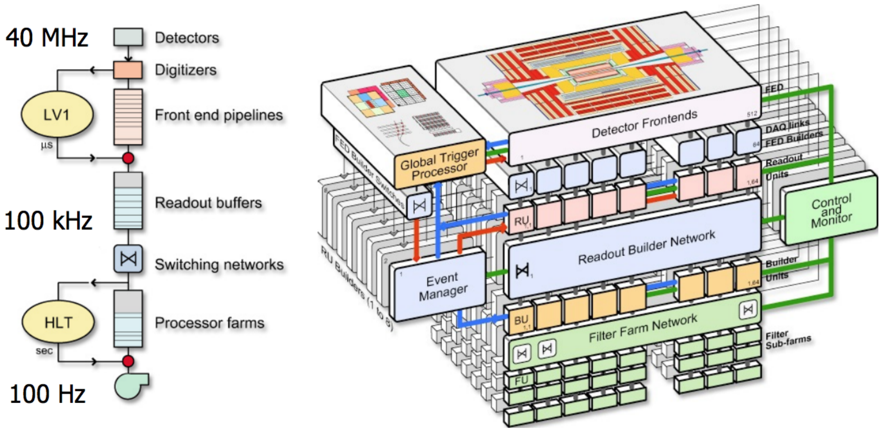

Figure 4.1 : Schematic of the functionality and data flow through the DAQ system. Take from Ref. [98].

Figure 4.1 shows a schematic of the function of the full trigger and DAQ system. The DAQ has the task to transport the data from about 650 front ends at the detector side, through the trigger system for processing and filtering of events, to the storage units. Based on the decision of the trigger system, an event is stored or skipped. The stored events are written to a temporary disk buffer before being transferred to the computing center (Tier 0) at CERN for offline processing.

In general, CMS experiment has two levels of trigger, Level 1 Trigger (L1) and High Level Trigger (HLT). The L1 is a hardware-based trigger, where information from the calorimeter, e.g., total transverse energy, can be used as a criteria of selecting or rejecting events. The output limit for the L1 is around 100 kHz. Events that pass the L1 trigger will enter the HLT, where the reconstruction of physics objects can be done in real time and only 400 Hz to 20 kHz can be recorded. Within the CMS collaboration, each physics analysis group design their own L1 triggers and HLT for physics, e.g., minimum-bias (MB) and high-multiplicity triggers used in this thesis.

4.1.1 Minimum-bias trigger

The MB trigger, as given by its name, is designed to select events with minimum physics input or selections, meaning that only events that are from an inelastic collision will be passed. Most of the physics topics require to have events that are hadronic instead of single or double diffractive, except for those who are interested in photon-nucleus collisions. Theoretically, the difference between elastic and inelastic collisions are trivial and well defined, however in experiment, only detector signals and responses can be used to determine whether an event is inelastic.

Thanks to the signature of inelastic collisions, usually there are detector activities (e.g., particle production) on both side of the detector along the beam axis, and most likely, it will be a collision vertex that can be reconstructed. Therefore, these signals can be used to design a MB trigger.

The mechanism of MB trigger is similar in pp, pPb, and PbPb collisions, where only certain thresholds are different. In pp or pPb collisions, only one side of the detector has enough amount of energy can fire the trigger, while both side of the detector have to have such condition in order to fire the trigger in PbPb collision. In addition, the detector condition changed over time and the MB trigger algorithm changed accordingly as well.

- 2013 pPb 5.02 TeV data taking: The relatively low pPb collision frequency (up to 0.2 MHz) provided by the LHC in the nominal run allowed the use of a track-based MB trigger, HLT_PAZeroBiasPixel_SingleTrack. Here, ZeroBias (ZB) refers to the crossing of two beams (bunch crossing) at CMS. For every few thousand pPb bunch crossings, the detector was read out from the L1 trigger and events were accepted at the HLT if at least one track (reconstructed with only the pixel tracker information) with $p_{\mathrm{T}} > 0.4$ GeV was found. The trigger had a efficiency of 99% for hadronic inelastic collisions.

- 2015 PbPb 5.02 TeV data taking: The MB events are triggered by a coincidence from both side of the HF detector ($3 < |\eta| < 5$). During the run, before and after run 263155, the threshold of the MB trigger on each side of the HF has been changed. The trigger name is HLT_HIL1MinimumBiasHF1AND_v1 and HLT_HIL1MinimumBiasHF2AND_v1, respectively.
- 2016 pPb 8.16 TeV data taking: a similar track-based MB trigger was used as in 2013, HLT_PAZeroBias_SinglePixelTrack_v1. The trigger had a efficiency of 97% for hadronic inelastic collisions, where a single pixel track with $p_{\mathrm{T}} > 0.4$ GeV within $|\eta| < 2.4$ is required.

As the most important trigger, MB trigger is investigated at the beginning of the data taking. For example, in the case of pPb run at 8.16 TeV, the MB trigger efficiency is studied as a function of the HF detector threshold in terms of ADC count, shown in Fig. 4.2. The first few runs were analyzed, where the MB signal efficiency is defined as the number of events passed the threshold at 17 ADC over all events that pass the ZB and a single pixel track. On the other hand, the detector noise that could mis-fire the trigger can be studied via the single bunch data, denoted as BPTXPlus or BPTXMinus, where only one bunch is filled with beam but with the other completely empty. Using the same definition, the noise level or noise "efficiency" can be plotted as a function of HF threshold. Note that the trigger is studied with at least one side of the HF fires and both sides of the HF fire, denoted as "OR" and "AND", respectively.

The MB trigger efficiency is also studied after the data has been taken. For the

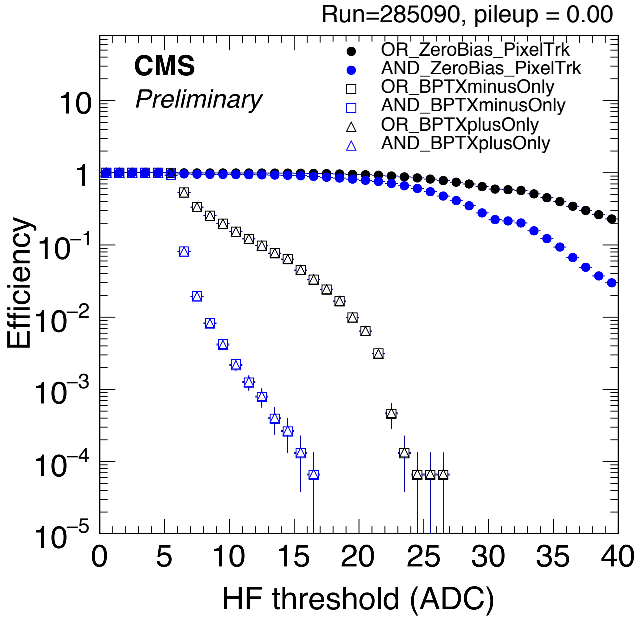

Figure 4.2 : MB signal and noise efficiency as a function of HF ADC count is shown for the run 285090 in pPb 8.16 TeV collisions.

recent pPb 8.16 TeV data, the efficiency of this MB trigger was studied using two approaches, while one based on ZB data and another one using MC events.

The MB trigger efficiency from data is defined as the ratio of the number of events that fire the trigger over the number of ZB events. This can be calculated in every event activity bin, where the event activity can be the number of good quality tracks in such event, or the sum of the transverse energy in the HF towers in the $|\eta| > 4$ region or any other event characterization variable. To obtain an unbiased measurement of the efficiency, the background events must be subtracted from the ZB sample. In Fig. 4.3, a comparison of data of noncolliding bunches with paired bunches is shown as a function of the number of tracks (with $p_{\mathrm{T}} > 0.4$ GeV) associated to the vertex. The background events contribute mainly to the zero tracks bin, so if we exclude this bin from the efficiency measurement, the ZB sample can be considered clean.

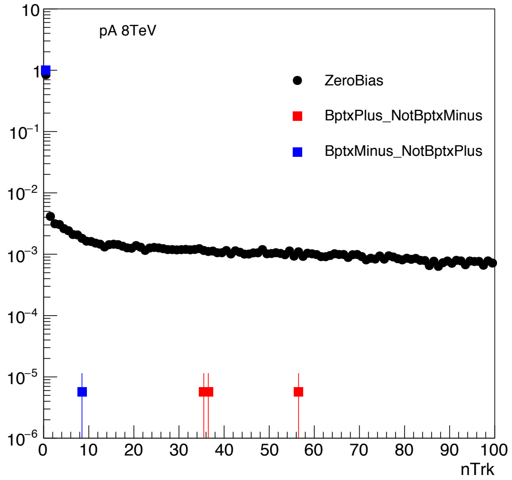

Figure 4.3 : Paired (coincidence of BPTX) and unpaired bunches (BPTX XOR) as a function of the number of tracks associated to the vertex

For the comparison of the ZB and MB samples, the corresponding L1 and HLT trigger prescales must be taken into account. In the top panel of Fig. 4.4 the comparison of the distributions of tracks in the two samples, weighted by the prescales in an event-by-event basis, is shown. In the bottom panel the MB turn-on curve as a function of the number of tracks is presented. The MB trigger is 100% efficient for events with 9-10 tracks ($p_{\mathrm{T}} > 0.4$ GeV). The integrated MB trigger efficiency for events with at least one track (with $p_{\mathrm{T}} > 0.4$ GeV) is found to be around 97%.

The efficiency measurement in MC events is defined as the ratio of the number of events that fire the MB trigger over the number of generated events. In Fig. 4.5 we show the trigger turn-on curves for the tracks and transverse energy in the forward calorimeter obtained from HIJING generator at 8.16 TeV. The integrated MB trigger efficiency at 5.02 TeV is 93.8% (from EPOS), and at 8.16 TeV is 93.8%-98.7% (from EPOS or HIJING).

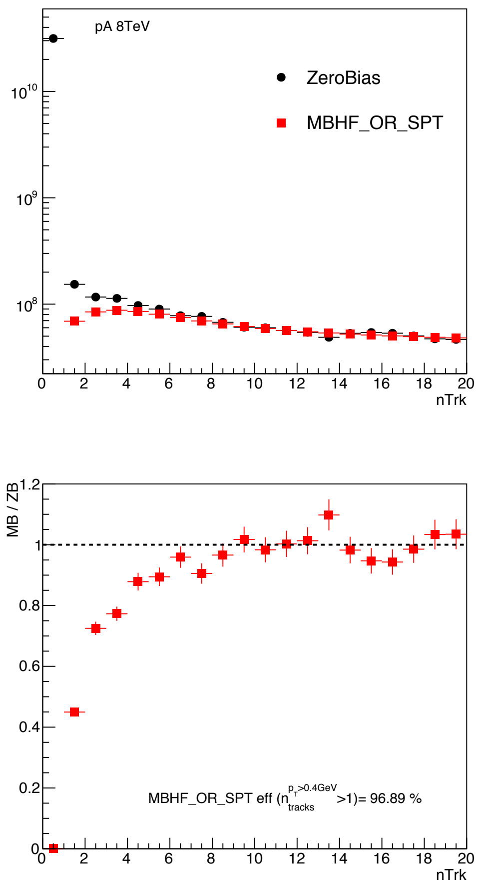

Figure 4.4 : Top: Comparison of the tracks distributions in zerobias and minimum-bias samples weighted by their corresponding L1 and HLT prescales. Bottom: Minimum-bias trigger turn-on curve as a function of tracks. The trigger efficiency for events with at least one track with p_{T} >0.4 GeV is shown in the figure.

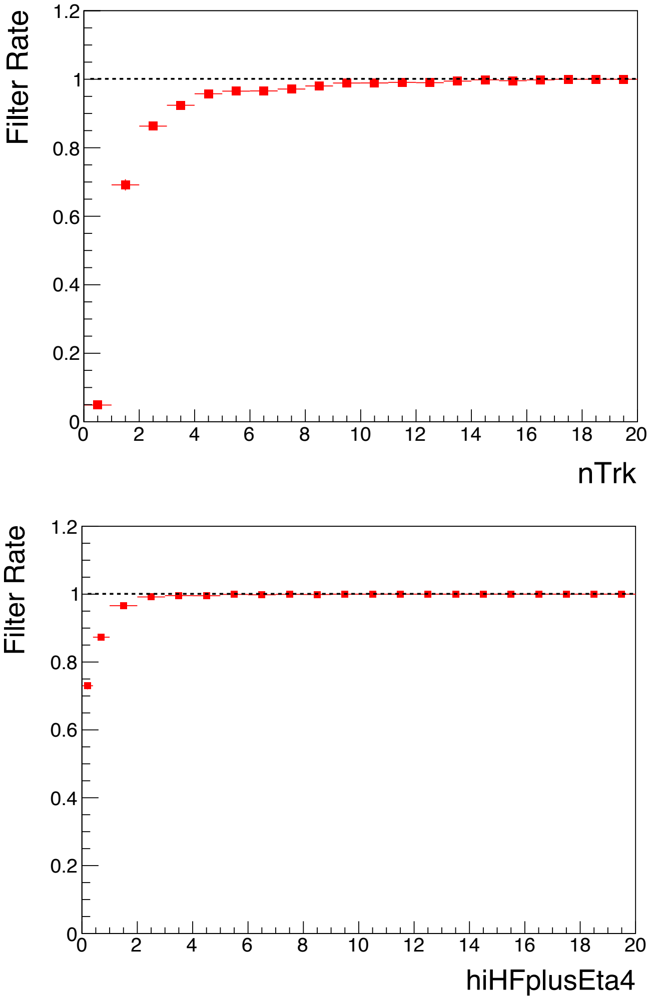

Figure 4.5 : The MB efficiency from HIJING generator at 8.16 TeV as a function of the number of tracks (left) and the transverse energy (in units of GeV) deposited in the plus side of the forward calorimeter at $|\eta| > 4$, denoted as “hiHFplusEta4” in the axis label.

4.1.2 High-multiplicity trigger

The high-multiplicity trigger, was firstly employed in 2009, for the pp collisions at 7 TeV. After the initial success, this trigger was found to be useful and necessary for a wide range of physics in small systems, e.g., pp and pPb collisions. The purpose of this trigger is to record a large number of events, focusing on the high event charged-particle multiplicity range (number of tracks that greater than 185 in a single collision, for instance), where an event with multiplicity 185 happens only one in ten million for pPb collisions.

The high-multiplicity trigger involves two major parts:

- L1: A trigger decision is firstly made on the scalar sum of total transverse momentum at L1 (L1_ETT) over the CMS calorimetry, including ECAL and HCAL, in order to to select events with high multiplicity. During 2009-2010 pp data taking, the HF energy is also included in the calculation of E_{TT}. Starting from the 2016 pPb 8.16 TeV run, a new algorithm has been implemented on the L1 trigger. Instead of using total transverse momentum, the number of active energy towers (each tower with a energy greater than 0.5 GeV) is used.

- HLT: As track reconstruction becomes available at HLT level, number of reconstructed pixel tracks is used to filter out high multiplicity events. However, a simple counting of all reconstructed pixel tracks would lead to significant contributions from pileup events (events with more than one inelastic collisions per bunch crossing), instead of a single event with high charged-particle multiplicity. To reduce the number of pileup, the trigger proceeds with the following sequences: the reconstructed pixel tracks with $p_{\mathrm{T}} > 0.4$ GeV, which originates within a cylindrical region of 15 cm half length and 0.2 cm in transverse radius with respect to the average collision point, are used to reconstruct vertices. The trigger then counts the number of pixel tracks with kinematic cuts of $|\eta| < 2.4$ and $p_{\mathrm{T}} > 0.4$ GeV, within a distance of 0.12 cm in z-direction to the vertex associated with highest number of tracks. The position of vertices along the nominal interaction point along the beam axis is required to be within ±15cm range.

Most of the high-multiplicity triggers are similar. Below, only a detail description of the high-multiplicity trigger in pPb at 8.16 TeV is presented. In pPb collisions at 8.16 TeV, the events in the charged multiplicity ranges above 120 were selected on HLT using dedicated triggers with charged particle multiplicities thresholds of: 120, 150, 185, 250, and 280. The first two thresholds were seeded by L1 MB triggers, while the others were seeded by tower count (TC) trigger in barrel ECAL and HCAL detectors, where events were selected if passing a criteria in the number of active towers. An active tower was defined as a trigger tower (ECAL+HCAL) with a transverse energy greater than 0.5 GeV. It was used TC > 115 or 120 for multiplicity between 185 and 250 and TC > 145 or 150 for multiplicity above 250. The reason for the usage of two TC thresholds for the same multiplicity range is related with the observation of a considerable variation in the noise level of HCAL during data-taking, which showed some dependence with the LHC filling scheme for the energy considered for TC. This non-uniformity in the trigger performance was taken into account in the analysis, and no significant effect has been observed.

The multiplicity thresholds at HLT are defined on a set of tracks selected with:

- $p_{\mathrm{T}} > 0.4$ GeV
- $|\eta| < 2.4$

- $\mathrm{MinSepZ_{pixel}} < 0.12$
- $\mathrm{MinSepZ_{full}} < 0.15$,

where $\mathrm{MinSepZ_{pixel}}$ and $\mathrm{MinSepZ_{full}}$ represent the minimum separation in longitudinal direction between the vertex and tracks that are reconstructed using only the pixel detector and using the full tracker, respectively. In addition, an event selection based on the number of pixel tracks (ranging from 40 to 140, depending on the full-tracker track multiplicity thresholds) and vertex distance of within 15 cm in longitudinal direction with respect to the detector origin, are applied. The trigger performance can be found in Appendix. C.1, where the multiplicity ranges for the analysis are required to have at least a trigger efficiency above 95%.

4.2 Data and Monte Carlo samples

4.2.1 Data samples

The analysis of the CME and CMW in pPb and peripheral PbPb collisions are performed using the data recoded by CMS experiment, which were certified by the data certification team. Data are defined as good for physics analysis if all sub-detectors, trigger and physics objects (tracking, electron, muon, photon and jet) show the expected performance. Table C.1 in Appendix. C.2 summaries the detailed information of the data samples used in this work.

The data samples were taken in 2013 and 2016 for 5.02 and 8.16 TeV pPb collisions, respectively, and the PbPb collisions at 5.02 TeV was recorded during the dedicated heavy-ion run in 2015. The total integrated luminosity is about 35 nb^{-1} for 5.02 TeV pPb collisions, 174 nb^{-1} for 8.16 TeV pPb collisions, and 530 $\mu\mathrm{b}^{-1}$ for 5.02 TeV PbPb collisions.

4.2.2 Monte Carlo generators and samples

The reconstruction performance of various physics objects, charged tracks in this work, can be tested using the MC generators. There are two parts that are important for the MC samples. First of all, in order to study the reconstruction algorithm under realistic conditions with reasonable underlying physics, MC generators need to “simulate” the data with similar particle production. In addition, the detector condition is also required to apply on the simulation under detector simulation. In this thesis, three different MC generators are used to determine the tracking performance, e.g., efficiency and mis-reconstruction rate, event selection efficiency, pileup rejection and charge asymmetry correction.

- HIJING: The Heavy Ion Jet INteraction Generator (HIJING) [99] is used for understanding tracking performance and charge asymmetry corretion in pPb collisions. HIJING 1.0 is used to reproduce the particle production with multiple nucleon-nucleon collisions.

- EPOS: The EPOS LHC Generator [100] is used as cross-check for charge asymmetry correction in pPb collisions, as well as tracking efficiency correction. Besides the description of particle production with multiple nucleon-nucleon collisions, it also has an implementation of collective flow.

- HYDJET: HYDJET++ [101] is a MC event generator to simulate relativistic heavy ion collisions considered as a superposition of the soft, hydro-type state and the hard state resulting from multi-parton fragmentation. The HYDJET sample is also used to derive the tracking efficiency correction table in different charged-particle multiplicity.

In addition to description of particle production, it is also critical to have a good simulation of the detector. The detailed MC simulation of the CMS detector response is based on GEANT4 [102]. Particles from generators are propagated through detector and the simulated detector signals are processed as if they are real data.

Chapter 5

Track reconstruction and event selections

5.1 Track reconstruction

Track, the spatial trajectory of a particle, can be reconstructed using a modern particle tracking detector, e.g., the tracking system in CMS experiment. Almost all physics analysis need to use information of tracks that produced from the collisions. As briefly introduced in Chapter. 3, the primary function of silicon detector is to reconstruct tracks, and the process of this reconstruction is denoted as "tracking". The tracking algorithm in CMS uses the information from the hits that produced by the particle going through the silicon detector layers, where the spatial position of those hits on the layers can be used to build a track. The particles that can be reconstructed have to be charged particle, so that they can be deflected by the strong magnetic field provided in CMS experiment. The tracking algorithm used is known as the Combinatorial Track Finder (CTF) [103], which is an extension of the Kalman Filter [104].

In the analysis of this work, the pPb and PbPb data are both reconstructed using the standard tracking algorithm, similar as was done on the pp data. However, because of a busy environment that produced by PbPb collisions, the tracking becomes a challenge in the central events. A typical central event can produce up to 10000-20000 tracks, where the number of combinations using all the hit information becomes very large and therefore takes a very long time. Therefore, the PbPb data can only be reconstructed using the pp or pPb algorithm up to 30% centrality. In this section, the idea of the basic tracking algorithm is introduced, followed by the tracking performance in pPb and PbPb collisions.

5.1.1 Iterative tracking

The dedicated tracking algorithm is essentially to solve the problem of the large combinatorial. The basic idea of *iterative tracking* is to break the whole process into smaller steps. The initial iterations are to search for tracks that are easiest to find (e.g., of relatively large p_{T}, and produced near the interaction region). After each iteration, hits associated with tracks that have already been used are removed, thereby reducing the combinatorial complexity, and simplifying subsequent iterations in a search for more difficult classes of tracks (e.g., low-p_{T}, or greatly displaced tracks) [103].

After all the iterations completed, the final step is to merge all the tracks that have been found by each iterations, where the information of which iteration one track was originated can be found using a variable called “OriginalAlgo”. As for the merging, it is not uncommon to have two iterations to find the same track because early iterations use only hits from the pixel layers, and later iterations may pick up the hits that produced by the same track in the strip layers. Therefore, if two tracks from different iterations share a certain fraction of hits, these two tracks are merged into one and added to the iteration with a higher track quality. If the same track quality has been found, the earlier iteration will be assigned to the track’s “algo” variable, different from its “OriginalAlgo”. In heavy ion events, the iterations with low p_{T} search window, or displaced with respect to the primary vertex take longer time than those primarily for high p_{T} particles. The details of the pp algorithm can be found in Ref. [103], where the PbPb algorithm can be found in Appendix. C.3.

5.1.2 Track selection

In the analysis presented in this thesis, the official CMS *highPurity* [103] tracks are used. For further selections, a reconstructed track was considered as a primary-track candidate if the transverse impact parameter significance, $d_{\mathrm{xy}}/\sigma(d_{\mathrm{xy}})$, and the longitudinal impact parameter significance, $d_{\mathrm{z}}/\sigma(d_{\mathrm{z}})$, are both less than 3 with respect to the best primary vertex. The best primary vertex is the vertex that has the largest number of tracks, or best χ^2probability if the same number of tracks is found. In order to remove tracks with poor momentum estimates, the relative uncertainty of the momentum measurement $\sigma(p_{\mathrm{T}})/p_{\mathrm{T}}$ was required to be less than 10%. In addition, the number of hits that associated with the pixel layer is required to be larger than zero in order to suppress the track splitting when the pseudorapidity difference of two tracks are very small. Primary tracks that fall in the kinematic range of $|\eta| < 2.4$ and $p_{\mathrm{T}} > 0.3$ GeV were selected in the analysis to ensure a reasonable tracking efficiency and low fake rate.

5.1.3 Track reconstruction performance

The performance of the track reconstruction is evaluated based on the matching of selected reconstructed tracks and generator level particles. In CMS criteria, a track is matched to a generator level charged particle if 75% of reconstructed hits associated to the track are compatible with hits created in the simulation of a particle going through the detector. In order to quantify the performance of track reconstruction, several quantities are defined:

- Efficiency: The fraction of primary particles from generator which are matched to at least one reconstructed track. Here, primary particle is defined to be charged particles produced in the collision or are decay products of particles with a mean proper lifetime of less than 1 cm/c.

- Fake rate: The fraction of reconstructed tracks that do not match any primary particles at generator level.
- Multiple reconstruction rate: The fraction of generator level primary particles which match to more than one reconstructed tracks.
- Non-primary reconstruction fraction: The fraction of reconstructed tracks matched to a non-primary particle at generator level, which is created by interactions of the primary particles with the detector.

The track reconstruction performance is more reliable when efficiency is closer to 1 and fake rate, multiple reconstruction and non-primary reconstruction rate are closer to 0. Figs. 5.1- 5.4 shows track reconstruction performance in pseudorapidity (η) and transverse momentum (p_{T}) based on MC samples from HIJING pPb simulations at $\sqrt{s_{_{NN}}} = 5.02$ TeV. The performance is similar in pp collisions since identical reconstruction algorithm is used. Inelastic nuclear interactions are the main source of tracking inefficiency. The formation of a track can be interrupted if a hadron undergoes a large-angle elastic nuclear scattering. Hence the hadron can be reconstructed as a single track with fewer hits, or as two separate tracks, or even not be found at all. Such efficiency loss is higher at large η regions with large material content.

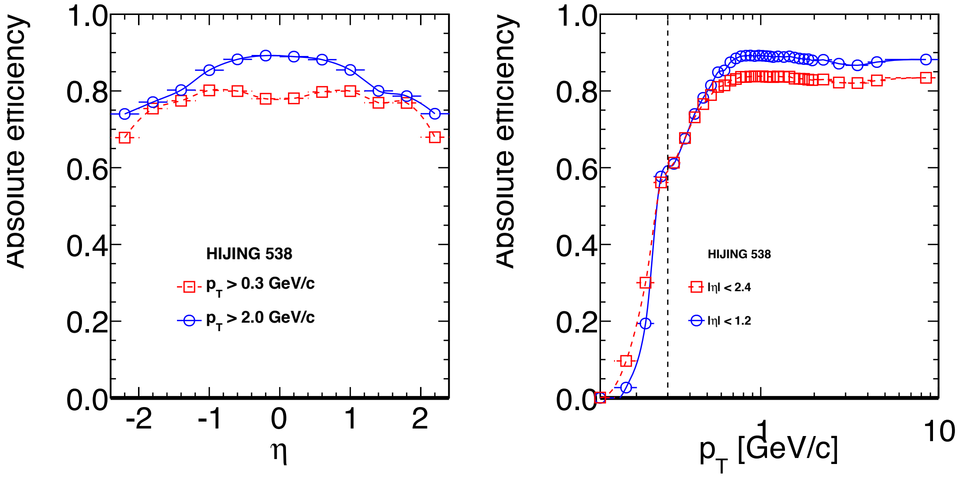

Figure 5.1 : Projections of the tracking efficiency as a function of η (left) and p_T (right). The dashed line shows the lower p_{T} limit (0.3 GeV/c) used in the analysis.

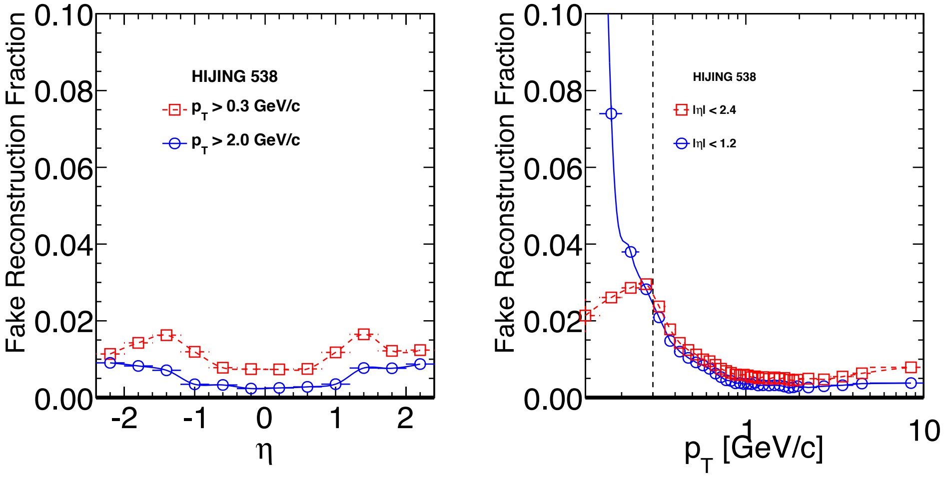

Figure 5.2 : Projections of the fake track fraction as a function of η (left) and p_T (right). The dashed line shows the lower p_{T} limit (0.3 GeV/c) used in the analysis.

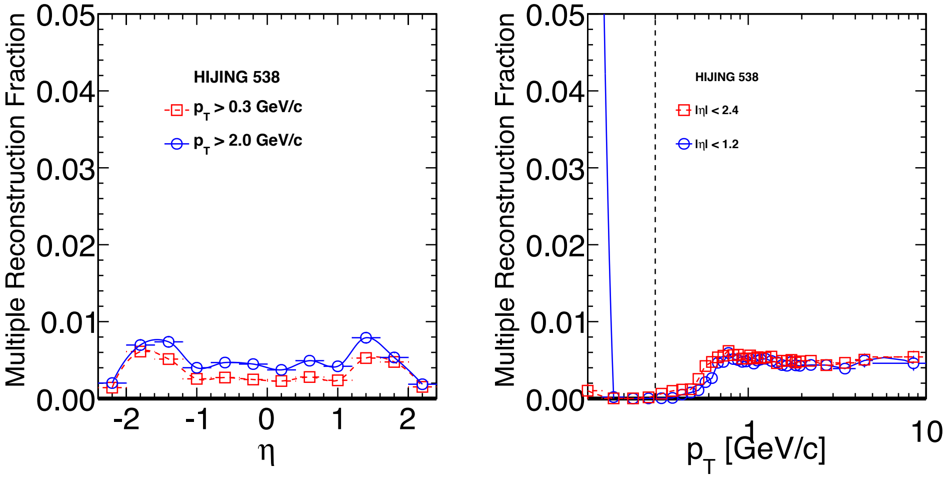

Figure 5.3 : Projections of the multiple reconstruction fraction as a function of η (left) and p_T (right). The dashed line shows the lower p_{T} limit (0.3 GeV/c) used in the analysis.

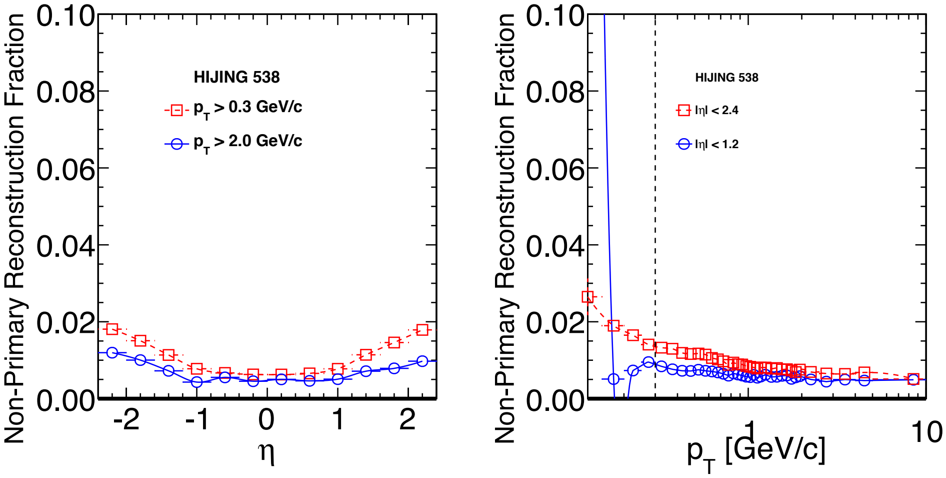

Figure 5.4 : Projections of the non-primary reconstruction fraction as a function of η (left) and p_T (right). The dashed line shows the lower p_{T} limit (0.3 GeV/c) used in the analysis.

Not only tracking performance in pPb collisions has been looked into, the PbPb performances are also investigated using both pp and PbPb reconstruction algorithm, in different ranges of charged-particle multiplicity. As expected, the pp tracking algorithm generally outperforms the PbPb algorithm, in terms of tracking efficiency or fake rate. Moreover, the multiplicity dependence has been studied in details. In MC sample with a pp reconstruction, the centrality is not a good variable to classify events as it is certainly different from that of the data, due to the detector noise in the calorimeters. Therefore, instead of studying the tracking performance in ranges of centrality, the charged-particle multiplicity has been used when pp tracking algorithm is applied. The results that are presented in this thesis are tracking efficiency corrected. The detail tracking performance and their comparisons of pp and PbPb tracking algorithm can be found in Appendix. C.4.

5.1.4 Jet core iteration development

Before the jet core iterative tracking, the pixel clusters are applied with a splitting algorithm to improve the cluster resolution around a very high p_{T} jet. Due to the high occupancy of a very high p_{T} jet, e.g., two small clusters could be merged into a large cluster, which affects the tracking performance in the later track finding. Splitting the clusters around a defined jet axis, i.e., the transverse momentum of jet greater than 100 GeV and $\delta R < 0.1$, where $\delta R = \sqrt{\delta\eta^2 + \delta\phi^2}$, can recover some merged clusters. In heavy ion collisions, this technique cannot be directly applied without background subtraction on the jet because the pixel cluster splitting step would be simply run everywhere besides the real high p_{T} jet, which results in a large amount of memory consumption and timing. Therefore, before the pixel cluster splitting, the background subtraction has been applied on the calorimeter jets, "akPU4CaloJets", to select on real high p_{T} energy jet regions in order to perform the splitting. The background subtraction is a standard heavy-ion procedure in jet reconstruction. The split clusters from the pixel cluster splitting are used to feed all tracking iterations that listed in Table. C.2.

The jet core iterative tracking is taken place after the 4 global iterative tracking. However, note that the tracking outputs would not be any different if jet core iterative tracking is run earlier or any other orders because all the clusters inside of the defined jet cone are used for track seeding instead of using the after-removal clusters from the previous iterations. In other words, no cluster removal step is applied within the jet core. The seeding pattern in heavy-ion jet core iterative tracking is different from that in the pp tracking algorithm. Pixel triplets (a set of three hits) are used instead of pairs since large amount of memory is needed for pairs (much more combinations) and this is currently not tolerable in heavy-ion reconstructions.

Moreover, while using all the pixel clusters without cluster removal from previous iteration, jet core iterative tracking might produce duplicate tracks from earlier iterations. Track merger is run at the very last step in the tracking sequence and the standard track merger has been applied. More specifically, if one track is found in both pixel triplet step and jet core step, depending on their hits information, a proper score would be assigned for each track and a higher score will win the algorithm bit of that track. Similar as was described in Sec. 5.1.1.

The performance figures again are mainly focusing on the tracking efficiency and fake reconstruction rates, which are shown in Fig. 5.5 by using a dijet embedded sample with leading jet p_{T} above 370 GeV. The jet p_{T} is required to be greater than 100 GeV and $|\eta| < 1.0$. Only tracks with p_{T} greater than 10 GeV are used in jet core iterative tracking. For both the tracking efficiency and fake reconstruction rates, with pixel cluster splitting and jet core iterative tracking are compared before and after their implementation. In addition, the tracking efficiency and fake reconstruction rates are calculated from the complete sequence of tracking instead of jet core iterative tracking alone.

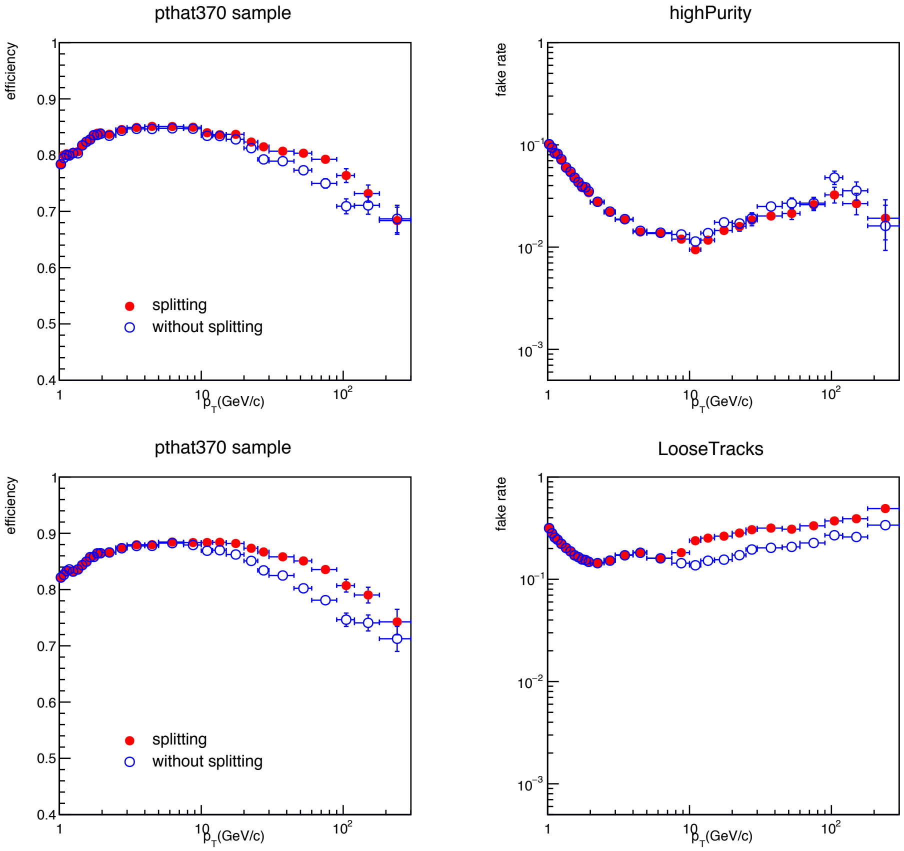

Figure 5.5 : The tracking efficiency and fake reconstruction rates are shown with track quality high purity (top) and loose (bottom). The jet p_{T} is greater than 100 GeV/c and $|\eta| < 1.0$. For both the tracking efficiency and fake reconstruction rates, the comparison between splitting plus jet core iterative tracking and without is presented.

As mentioned above, in heavy-ion jet core iterative tracking, pixel triplets is used for seeds instead of pixel pairs. The same tracking performance is shown in Fig. 5.6, with using pixel pairs. By comparing Fig. 5.6 and the top figure in Fig. 5.5, there is no huge difference between using pixel triplets and pixel pairs has been observed.

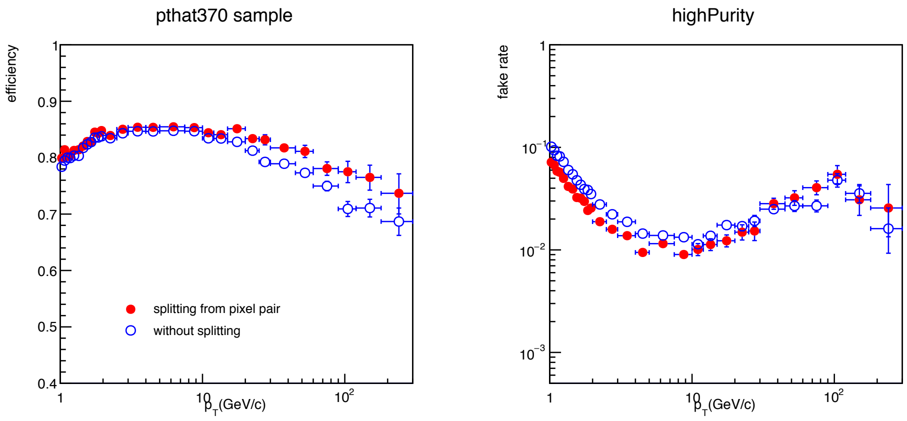

Figure 5.6 : The tracking efficiency and fake reconstruction rates are shown with with track quality high purity and compared between with and without pixel cluster splitting with jet core iterative tracking. The jet p_{T} is greater than 100 GeV/c and $|\eta| < 1.0$. Instead of using pixel triplets as seeds, pixel pairs is used when producing the tracking performance.

In Fig. 5.7, tracking efficiency and fake reconstruction rates are shown with high purity track selection and with all the dijet p_{T} hat samples combined, weighted by the corresponding jet p_{T} cross sections. The default option, pixel cluster splitting and jet core iterative tracking, is shown with only pixel cluster splitting and only jet core iterative tracking. Overall, the improvement mostly comes from the additional jet core iterative tracking instead of pixel cluster splitting.

Finally, the timing of each iteration together with pixel cluster splitting step is studied. In Fig. 5.8, the timing, defined as second per event, is shown as a function

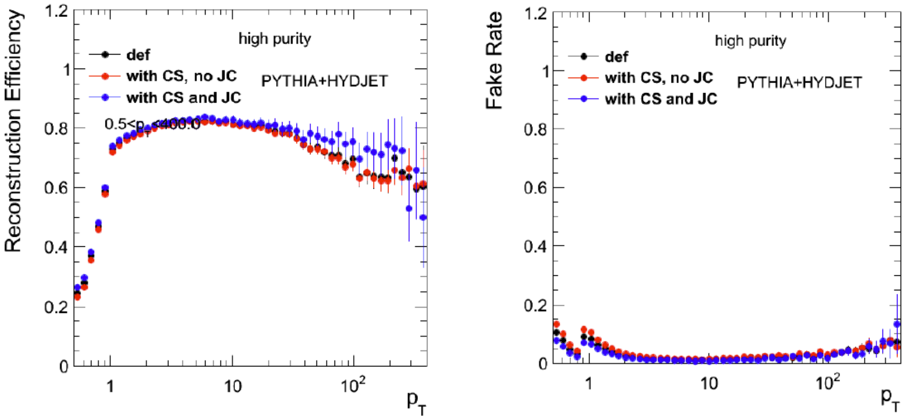

Figure 5.7 : The tracking efficiency and fake reconstruction rates are shown with all the p_{T} hat samples combined. The jet p_{T} is greater than 100 GeV and $|\eta| < 1.0$. For both the tracking efficiency and fake reconstruction rates, the comparison between the default option, pixel cluster splitting and jet core iterative tracking, and with only pixel cluster splitting and only jet core iterative tracking are presented.

of HF energy. The timing goes up when the HF energy goes up corresponding to the longer timing process in more central events. The relative timing between different iterations are compared and it is shown that the pixel cluster splitting and jet core iterative tracking do not increase the reconstruction time significantly. Therefore, these two developments were implemented for the PbPb reconstruction algorithm since 2015.

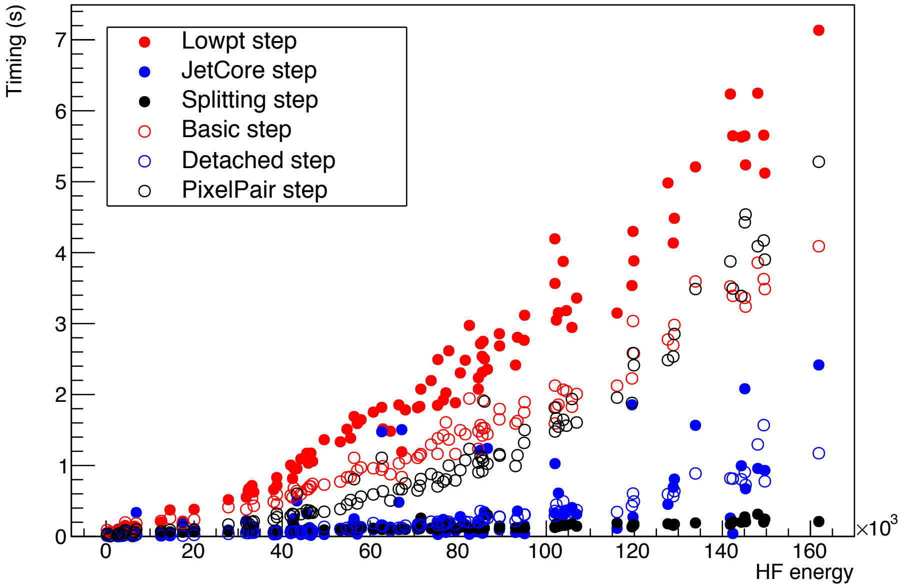

Figure 5.8 : The timing of each heavy-ion track reconstruction iterations is presented. The unit time per event is plotted as a function of HF energy.

5.2 Offline selection of collision events

Based on the triggered events, e.g., MB or high-multiplicity events, offline analysis event selections are applied in order to further reject events that are not hadronic, or from beam-gas collisions in the beam pipe.

In pPb collisions, in order to select non-single-diffractive (NSD) events, a coincidence of at least one calorimeter tower of more than 3 GeV in total energy on both side of the Forward Calorimeter (HF) in CMS, between $3.0 < |\eta| < 5.0$ units. For event track multiplicity greater than 10, the fraction of high-purity tracks is required to be less than 25% in order to remove the beam-induced background events. In addition, events are also required to at least have a valid reconstructed primary vertex, with at least two tracks associated with it, where this vertex has to be within ±15 cm in the beam direction and a radius of $\rho < 0.15$ cm in the transverse direction with respect to the average transverse positions of all vertices.

In PbPb collisions, similar event selections are applied. Instead of only one calorimeter tower, it requires at least 3 towers with each above 3 GeV on both side of the HF between $3.0 < |\eta| < 5.0$ units.

Among those pPb interactions simulated with the EPOS [105] and HIJING [99] event generators, which have at least one primary particle with total energy $E > 3$ GeV in both η ranges of $-5 < \eta < -3$ and $3 < \eta < 5$, the above criteria are found to select 97–98% of the events for pPb.

For example, in order to estimate the efficiency of the online and offline selection on data (MB trigger and event selection), the 8 TeV HIJING turn-on curves (trigger plus event selection) are used to weight the data events passing the trigger and event selection conditions. In Fig. 5.9 we show the tracks distribution of selected events together with the distribution of selected events weighted by the MC efficiency. The data selection efficiency is computed from the ratio of the integrals of the weighted and unweighted selected samples. The resulting trigger and event selection efficiency was found to be about 98%.

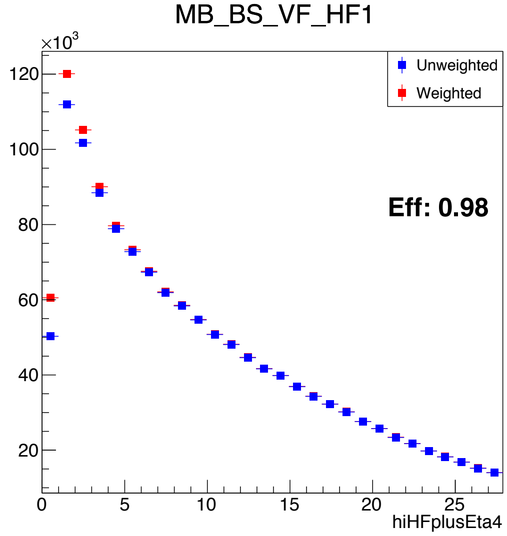

Figure 5.9 : Distribution of transverse energy in the forward calorimeter, denoted as “hiHFplusEta4” in the axis label in units of GeV. The estimation of the minimum bias and trigger selection efficiency is performed from the ratio of the number of events in the selected sample with the selected sample weighted by the MC efficiency

In pPb collision, the pileup effect has been largely removed by separating the primary vertex (for physics analysis) with all other vertices. The detail algorithm can be found in Appendix. C.5. The pileup effect in PbPb collisions has been found to be negligible.

5.3 Multiplicity classification

Most of the analysis has been performed in bins of track multiplicity, similarly to what was done in Ref. [73, 77, 83].

The full track multiplicity range is divided into many different multiplicity bins: [0,20), [20,30), [30,40), [40,50), [50,60), [60,80), [80,100), [100,120), [120,150), [150,185), [185,220), [220,260), [260,300), [300, 350). The fractions of total number of events for each multiplicity bin, as well as the average track multiplicity before and after corrections, are summarized in Table 5.1 for pPb data. The uncertainties on $\left\langle N_{\text{trk}}^{\text{corrected}} \right\rangle$ come from track quality cuts and from the tracking efficiency correction procedure, a total systematic uncertainty of 3.2%.

In order to compare directly the pPb and PbPb systems using event selections based on the multiplicity of the collisions, a subset of data from peripheral PbPb collisions collected during the 2011 LHC heavy-ion run with a minimum bias trigger were reanalyzed using the same track reconstruction algorithm as the one employed for pPb collisions. The selection of events and tracks is the same as for the present pPb analysis although a different trigger is used. A description of the 2011 PbPb data can be found in Ref. [106]. The average $N_{\text{trk}}^{\text{offline}}$ and $N_{\text{trk}}^{\text{corrected}}$ values, and corresponding average PbPb collision centrality, as determined by the total energy deposited in the HF calorimeters [107], are listed in Table 5.2 for each $N_{\text{trk}}^{\text{offline}}$ bin. Similarly, the uncertainties on $N_{\text{trk}}^{\text{corrected}}$ come from track quality cuts and from the tracking efficiency correction procedure, a total of 3.2%. To optimize statistical precision of the results, multiplicity classes are combined together as needed.

In PbPb collisions, in order to compare with other experiment, the data is also divided into classes based on centrality for the mid-central events (30–50%). The corresponding average $N_{\text{trk}}^{\text{offline}}$ and $N_{\text{trk}}^{\text{corrected}}$ are given in the Table 5.1.

Table 5.1 : Fraction of the full event sample in each multiplicity bin and the average multiplicity per bin for pPb data. The multiplicity of offline reconstructed tracks, $N_{\mathrm{trk}}^{\mathrm{offline}}$, was counted within the kinematic cuts of $|\eta| < 2.4$ and $p_T > 0.4$ GeV. The third and forth columns list the average values of $N_{\mathrm{trk}}^{\mathrm{offline}}$ as well as the average of $N_{\mathrm{trk}}^{\mathrm{corrected}}$, the event multiplicity corrected for all detector and algorithm inefficiencies.

Multiplicity bin ($N_{\mathrm{trk}}^{\mathrm{offline}}$)	Fraction	$\left\langle N_{\mathrm{trk}}^{\mathrm{offline}} \right\rangle$	$\left\langle N_{\mathrm{trk}}^{\mathrm{corrected}} \right\rangle$
MB	1.00	40	50±2
$[0, 20)$	0.31	10	12±1
$[20, 30)$	0.14	25	30±1
$[30, 40)$	0.12	35	42±2
$[40, 50)$	0.10	45	54±2
$[50, 60)$	0.09	54	66±3
$[60, 80)$	0.12	69	84±4
$[80, 100)$	0.07	89	108±5
$[100, 120)$	0.03	109	132±6
$[120, 150)$	0.02	132	159±7
$[150, 185)$	4×10^{-3}	162	195±9
$[185, 220)$	5×10^{-4}	196	236±10
$[220, 260)$	6×10^{-5}	232	280±12
$[260, 300)$	3×10^{-6}	271	328±14
$[300, 350)$	1×10^{-7}	311	374±16

Table 5.2 : Average centrality under standard definition based on HF total energy in each multiplicity bin and the average multiplicity per bin for PbPb data. The multiplicity of offline reconstructed tracks, $N_{\text{trk}}^{\text{offline}}$, was counted within the kinematic cuts of $|\eta| < 2.4$ and $p_T > 0.4$ GeV. The third and forth columns list the average values of $N_{\text{trk}}^{\text{offline}}$ as well as the average of $N_{\text{trk}}^{\text{corrected}}$, the event multiplicity corrected for all detector and algorithm inefficiencies.

Multiplicity bin ($N_{\text{trk}}^{\text{offline}}$)	<Centrality> ± RMS (%)	$\left\langle N_{\text{trk}}^{\text{offline}} \right\rangle$	$\left\langle N_{\text{trk}}^{\text{corrected}} \right\rangle$
$[0, 20)$	92±4	10	13±1
$[20, 30)$	86±4	24	30±1
$[30, 40)$	83±4	34	43±2
$[40, 50)$	80±4	44	55±2
$[50, 60)$	78±3	54	68±3
$[60, 80)$	75±3	69	87±4
$[80, 100)$	72±3	89	112±5
$[100, 120)$	70±3	109	137±6
$[120, 150)$	67±3	134	168±7
$[150, 185)$	64±3	167	210±9
$[185, 220)$	62±2	202	253±11
$[220, 260)$	59±2	239	299±13
$[260, 300)$	57±2	279	350±15
$[300, 350)$	55±2	324	305±18

Table 5.3 : The selected centrality interval and the corresponding average multiplicity per interval for PbPb data is shown. The multiplicities $N_{\text{trk}}^{\text{offline}}$ and $N_{\text{trk}}^{\text{corrected}}$ are determined for $|\eta| < 2.4$ and $p_{\text{T}} > 0.4$ GeV before and after efficiency corrections, respectively.

Centrality interval (%)	$\left\langle N_{\text{trk}}^{\text{offline}} \right\rangle$	$\left\langle N_{\text{trk}}^{\text{corrected}} \right\rangle$
30–35	1258	1573±69
35–40	1026	1283±56
40–45	811	1014±45
45–50	625	781±34

Chapter 6

Search for chiral magnetic effect in pPb and PbPb collisions

This chapter presents measurements of charge-dependent azimuthal correlation in pPb collisions at $\sqrt{s_{_{NN}}}$= 5.02 TeV and 8.16 TeV, taken by CMS detector in 2013 and 2016, respectively. The results are compared to semi-peripheral PbPb collision at $\sqrt{s_{_{NN}}}$= 5.02 TeV, with similar charged-particle multiplicities. The charge-dependent correlation, using two- and three-particle correlators that are described in this chapter, are explored as a function of pseudorapidity difference ($|\Delta\eta|$) between two charged particles, transverse momentum difference ($|\Delta p_{\mathrm{T}}|$), and the average p_{T} of two charged particles ($\overline{p}_{\mathrm{T}}$). In addition, the charge-dependent correlators are also investigated as a function of centrality and event multiplicity, averaged over $|\Delta\eta| < 1.6$ between the two charged particles. Besides the conventional three-particle correlator with respect to the second-order event plane γ_{112}, a new correlator with respect to the third-order event plane, γ_{123}, is developed, where this correlator is expected to be CME free (introduced in Chapter 2.4) and would be useful to constrain the background correlation in a data-driven way. In order to explicitly observe the flow-driven background and to see if there is any hint of CME signal, the two- and three-particle correlators are presented as a function of v_2, where an event shape engineering technique is used in order to vary the v_2 without changing event multiplicity or centrality. Finally, an upper limit of the CME fraction at LHC energies is derived for both pPb and PbPb collisions.

The majority of the work presented in this chapter is published in Refs. [87, 108].

6.1 Analysis techniques of charge-dependent azimuthal correlations with respect to the event planes

1. Three-particle correlator with respect to the second-order event plane: the traditional method of measuring the CME is to use the γ-correlator (γ and γ_{112} are used interchangeably in this thesis), which was introduced in Sec. 2.1, and therefore not repeated. Note that the three-particle correlator is calculated using the Q-vectors, and the particle c to reconstruct the event planes are selected in the forward region to suppress the short-range nonflow correlations. The details of the correlator can be found in the Sec. 6.1.1.

2. Higher-order harmonic three-particle correlator: by constructing a charge-dependent correlator with respect to the third-order event plane,

$$\gamma_{123} \equiv \langle \cos(\phi_\alpha + 2\phi_\beta - 3\Psi_3) \rangle , \tag{6.1}$$

charge-dependent background effects unrelated to the CME can be explored. In particular, in the context of the local charge conservation mechanism, the γ_{123} correlator is also expected to have a background contribution, with

$$\gamma_{123}^{\text{bkg}} = \kappa_3 \langle \cos(\phi_\alpha - \phi_\beta) \rangle \langle \cos 3(\phi_\beta - \Psi_3) \rangle = \kappa_3 \, \delta \, v_3, \tag{6.2}$$

similar to that for the γ_{112} correlator as given in Eq. (2.6). As the κ_2 and κ_3 parameters mainly depend on particle kinematics and detector acceptance effects, they are expected to be similar, largely independent of harmonic event plane orders. The relation in Eq. (6.2) can be generalized for all "higher-order harmonic" three-particle correlators, $\gamma_{1,n-1;n} = \kappa_n \, \delta \, v_n$. Derivation of Eq. (6.2) as well as generalization to all higher-order harmonics can be found in Appendix A.1, which follows similar steps as for that of Eq. (2.6) given in Ref. [68]. One caveat here is that when averaging over a wide η and p_{T} range, the κ_n value may also depend on the η and p_{T} dependence of the v_n harmonic, which is similar, but not exactly identical between the v_2 and v_3 coefficients [42, 83].

By taking the difference of correlators between same- and opposite-sign pairs (denoted as $\Delta\gamma_{112}$ and $\Delta\gamma_{123}$ among three particles, and $\Delta\delta$ between two particles) to eliminate all charge-independent background sources, the following relation is expected to hold if the charge dependence of three-particle correlators is dominated by the effect of local charge conservation coupled with the anisotropic flow:

$$\frac{\Delta\gamma_{112}}{\Delta\delta \, v_2} \approx \frac{\Delta\gamma_{123}}{\Delta\delta \, v_3}. \tag{6.3}$$

Therefore, an examination of Eq. (6.3) will quantify to what extent the proposed background from charge conservation contributes to the γ_{112} correlator, and will be a critical test of the CME interpretation in heavy ion collisions.

3. Event shape engineering (ESE): to establish directly a linear relationship between the charge-dependent part of γ_{112} correlator, $\Delta\gamma_{112}$, the ratio, $\Delta\gamma_{112}/\Delta\delta$, and v_2 coefficient, the ESE technique [92] is employed. A linear function would be fitted to the $\Delta\gamma_{112}$ and $\Delta\gamma_{112}/\Delta\delta$ as a function of v_2 in a narrow multiplicity or centrality range, the finite intercepts can be extracted, as well as an upper limit on the v_2-independent component fraction.

6.1.1 Calculations of two- and three-particle correlators using Q-vectors

Without directly reconstructing the event plane, the expression given in Eq. (2.4) can be alternatively evaluated using a three-particle correlator with respect to a third particle [20, 109], $\langle \cos(\phi_\alpha + \phi_\beta - 2\phi_c) \rangle / v_{2,c}$, where $v_{2,c}$ is the elliptic flow anisotropy of particle c with inclusive charge sign. The three-particle correlator is measured via the scalar-product method of Q vectors. A complex Q vector for each event is defined as $Q_n \equiv \sum_{i=1}^{M} w_i e^{in\phi_i}/W$, where ϕ_i is the azimuthal angle of particle i, n is the Fourier harmonic order, M is the number of particles in the Q_n calculation in each event, w_i is a weight assigned to each particle for efficiency correction, and $W = \sum_{i=1}^{M} w_i$ represents the weight of the Q vector. In this way, the three-particle correlator can be expressed in terms of the product of Q vectors, i.e., $Q_{1,\alpha}$ and $Q_{1,\beta}$, when particles α and β are chosen from different detector phase-space regions or carry different charge signs,

$$\gamma = \gamma_{112} = \frac{\langle \cos(\phi_\alpha + \phi_\beta - 2\phi_c) \rangle}{v_{2,c}} = \frac{\left\langle Q_{1,\alpha} Q_{1,\beta} Q^*_{2,\mathrm{HF}\pm} \right\rangle}{\sqrt{\frac{\left\langle Q_{2,\mathrm{HF}\pm} Q^*_{2,\mathrm{HF}\mp} \right\rangle \left\langle Q_{2,\mathrm{HF}\pm} Q^*_{2,\mathrm{trk}} \right\rangle}{\left\langle Q_{2,\mathrm{HF}\mp} Q^*_{2,\mathrm{trk}} \right\rangle}}}, \tag{6.4}$$

where the angle brackets on the right-hand side denote an event average of the Q-vector products, weighted by the product of their respective total weights W. Here $Q_{2,\mathrm{trk}}$ is the charge inclusive Q_2 vector of all particles in the tracker region, and $Q_{2,\mathrm{HF}\pm}$ denotes the Q_2-vector for particles c detected in the HF towers. When particles α and β are of the same sign and share the same phase space region (denoted as $\alpha = \beta$), an extra term is needed to remove the contribution of a particle pairing with itself, so evaluation of the three-particle correlator is modified as

$$\gamma_{112} = \frac{\langle \cos(\phi_\alpha + \phi_\beta - 2\phi_c) \rangle}{v_{2,c}} = \frac{\left\langle Q_{112} Q^*_{2,\mathrm{HF}\pm} \right\rangle}{\sqrt{\frac{\left\langle Q_{2,\mathrm{HF}\pm} Q^*_{2,\mathrm{HF}\mp} \right\rangle \left\langle Q_{2,\mathrm{HF}\pm} Q^*_{2,\mathrm{trk}} \right\rangle}{\left\langle Q_{2,\mathrm{HF}\mp} Q^*_{2,\mathrm{trk}} \right\rangle}}}, \tag{6.5}$$

where the Q_{112} is defined as,

$$Q_{112} \equiv \frac{\left(\sum\limits_{i=1} w_i \mathrm{e}^{i\phi_i} \right)^2 - \sum\limits_{i=1} w_i^2 \mathrm{e}^{i2\phi_i}}{\left(\sum\limits_{i=1} w_i \right)^2 - \sum\limits_{i=1} w_i^2}, \tag{6.6}$$

and the denominator of Eq. (6.6) is the respective event weight associated with Q_{112}.

In the numerators of Eqs. (6.4) and (6.5), the particles α and β are identified in the tracker, with $|\eta| < 2.4$ and $0.3 < p_\mathrm{T} < 3$ GeV, and are assigned a weight factor w_i to correct for tracking inefficiency. The particle c is selected by using the tower energies and positions in the HF calorimeters with $4.4 < |\eta| < 5.0$. This choice of η range for the HF towers imposes an η gap of at least 2 units with respect to particles α and β from the tracker, to minimize possible short-range correlations. To account for any occupancy effect of the HF detectors resulting from the large granularities in η and ϕ, each tower is assigned a weight factor w_i corresponding to its $E_\mathrm{T}$value when calculating the Q vector. The denominator of the right-hand side of Eqs. (6.4) and (6.5) corresponds to the $v_{2,c}$ using the scalar-product method [20,109], with $Q_{2,\mathrm{trk}}$ and $Q_{2,\mathrm{HF}\pm}$ denoting Q_2 vectors obtained from the tracker and the two HF detectors (positive and negative η side) with the same kinematic requirements as for the numerator. The three-particle correlator is evaluated for particles α and β carrying the same sign (SS) and opposite sign (OS). The SS combinations, $(+,+)$ and $(-,-)$, give consistent results and are therefore combined. For pPb collisions, the three-particle correlator is also measured with particle c from HF+ and HF−, corresponding to the p- and Pb-going direction, respectively. For symmetric PbPb collisions, the results from HF+ and HF− are consistent with each other and thus combined.

The higher-order harmonic three-particle correlator, γ_{123}, defined in Eq. (6.1), is evaluated in exactly the same way as the γ_{112} correlator as follows when particles α and β do not overlap,

$$\gamma_{123} = \frac{\langle\cos(\phi_\alpha + 2\phi_\beta - 3\phi_c)\rangle}{v_{3,c}} = \frac{\left\langle Q_{1,\alpha} Q_{2,\beta} Q^*_{3,\mathrm{HF}\pm}\right\rangle}{\sqrt{\frac{\left\langle Q_{3,\mathrm{HF}\pm} Q^*_{3,\mathrm{HF}\mp}\right\rangle \left\langle Q_{3,\mathrm{HF}\pm} Q^*_{3,\mathrm{trk}}\right\rangle}{\left\langle Q_{3,\mathrm{HF}\mp} Q^*_{3,\mathrm{trk}}\right\rangle}}}, \tag{6.7}$$

with higher-order Q vectors for particles α and β of SS and OS. Similarly to Eq. (6.5) when particles α and β can overlap, the γ_{123} can be evaluated via

$$\gamma_{123} = \frac{\langle\cos(\phi_\alpha + 2\phi_\beta - 3\phi_c)\rangle}{v_{3,c}} = \frac{\left\langle Q_{123} Q^*_{3,\mathrm{HF}\pm}\right\rangle}{\sqrt{\frac{\left\langle Q_{3,\mathrm{HF}\pm} Q^*_{3,\mathrm{HF}\mp}\right\rangle \left\langle Q_{3,\mathrm{HF}\pm} Q^*_{3,\mathrm{trk}}\right\rangle}{\left\langle Q_{3,\mathrm{HF}\mp} Q^*_{3,\mathrm{trk}}\right\rangle}}}, \tag{6.8}$$

where Q_{123} is defined as

$$Q_{123} \equiv \frac{\left(\sum\limits_{i=1} w_i \mathrm{e}^{i\phi_i} \sum\limits_{i=1} w_i \mathrm{e}^{i2\phi_i}\right) - \sum\limits_{i=1} w_i^2 \mathrm{e}^{i3\phi_i}}{\left(\sum\limits_{i=1} w_i\right)^2 - \sum\limits_{i=1} w_i^2}, \tag{6.9}$$

and the respective event weight associated with Q_{123} is the denominator of Eq. (6.9).

Similarly, the charge-dependent two-particle correlator, $\delta \equiv \langle\cos(\phi_\alpha - \phi_\beta)\rangle$, is also evaluated with Q vectors as $\delta = \left\langle Q_{1,\alpha} Q^*_{1,\beta}\right\rangle$ when particles α and β are chosen from different detector phase-space regions (or from particles with opposite charge signs), or otherwise,

$$\delta = \left\langle \frac{\left(\sum\limits_{i=1} w_i \mathrm{e}^{i\phi_i} \sum\limits_{i=1} w_i \mathrm{e}^{-i\phi_i}\right) - \sum\limits_{i=1} w_i^2}{\left(\sum\limits_{i=1} w_i\right)^2 - \sum\limits_{i=1} w_i^2} \right\rangle, \tag{6.10}$$

and the respective event weight is the denominator of Eq. (6.10).

The effect of the nonuniform detector acceptance is corrected by evaluating the cumulants of Q-vector products [110]. While the correction is found to be negligible for the γ_{112} and δ correlators, there is a sizable effect of 5–10% correction to the γ_{123} correlator.

6.1.2 Event shape engineering

In the ESE analysis, within each multiplicity range of pPb or centrality range of PbPb data, events are divided into different q_2 classes, where q_2 is defined as the magnitude of the Q_2 vector. In this analysis, the q_2 value is calculated from one side of the HF region within the range $3 < \eta < 5$ for both pPb and PbPb collisions (weighted by the tower E_{T}), where in pPb collisions only the Pb-going side of HF is used because of the poor resolution from a relatively low charged-particle multiplicity on the proton-going side. In each q_2 class, the v_2 harmonic is measured with the scalar product method using a common resolution term ($v_{2,c}$) as in the γ_{112} correlator. Therefore, the v_2 from the tracker region can be expressed in terms of the Q-vectors as

$$v_2 = \frac{\left\langle Q_{2,\alpha} Q^*_{2,\mathrm{HF}\pm} \right\rangle}{\sqrt{\frac{\left\langle Q_{2,\mathrm{HF}\pm} Q^*_{2,\mathrm{HF}\mp} \right\rangle \left\langle Q_{2,\mathrm{HF}\pm} Q^*_{2,\mathrm{trk}} \right\rangle}{\left\langle Q_{2,\mathrm{HF}\mp} Q^*_{2,\mathrm{trk}} \right\rangle}}}, \tag{6.11}$$

where particles from the HF are selected from the same region as particle c in the γ_{112} correlator.

In PbPb collisions, the particle c in the γ_{112} correlator is taken from the HF detector that is at the opposite η side to the one used to calculate q_2. However, the results are in good agreement with those where the particle c for γ_{112} and q_2 is measured from the same side of the HF detector, which can be found in Appendix A.2. In pPb collisions, the particle c in the γ_{112} correlator with respect to the Pb- and p-going sides is studied, when q_2 is measured only in the Pb-going side. The results are found to be independent of the side in which the particle c is detected (shown in Fig. 6.15 upper panel).

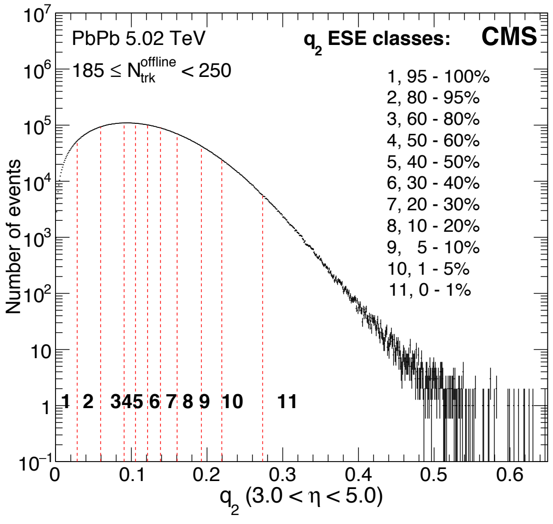

Figure 6.1 : The q_2 classes are shown in different fractions with respect to the total number of events in multiplicity range $185 \leq N_{\text{trk}}^{\text{offline}} < 250$ in PbPb (left) and pPb (right) collisions at $\sqrt{s_{NN}} = 5.02$ and 8.16 TeV, respectively.

In Fig. 6.1, the HF q_2 distributions are shown for PbPb and pPb collisions in the multiplicity range $185 \leq N_{\text{trk}}^{\text{offline}} < 250$, where most of the high-multiplicity pPb events were recorded by the high-multiplicity trigger in this range. As indicated by the vertical dashed lines, the distribution is divided into several intervals with each corresponding to a fraction of the full distribution, where 0–1% represents the highest q_2 class. For each q_2 class, the three-particle γ_{112} is calculated with the default kinematic regions for particles α, β, and c, and the v_2 harmonics from the tracker ($|\eta| < 2.4$) are also obtained by the scalar-product method [111]. The pPb and PbPb results are presented in Section 6.3.3 for both SS and OS pairs, as well as the differences found for the two charge combinations.

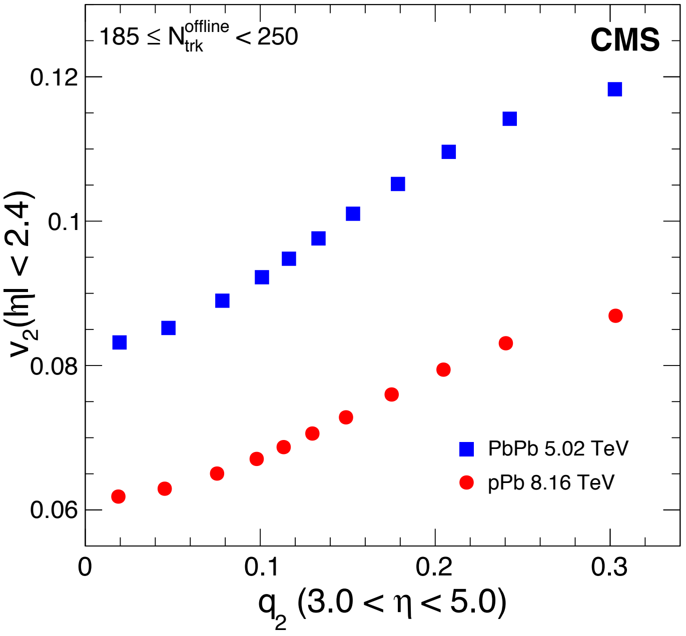

Figure 6.2 : The correlation between the tracker v_2 and the HF q_2 is shown for pPb and PbPb collisions at collisions at $\sqrt{s_{NN}} = 8.16$ and 5.02 TeV, respectively.

In Fig. 6.2, the v_2 values for tracker particles as a function of the average q_2 in each HF q_2 class are shown. A proportionality close to linear is seen, indicating the two quantities are correlated because of the initial-state geometry [112].

6.2 Results of charge-dependent azimuthal correlation with respect to the second-order event plane in pPb and PbPb collisions at $\sqrt{s_{NN}}$= 5.02 TeV

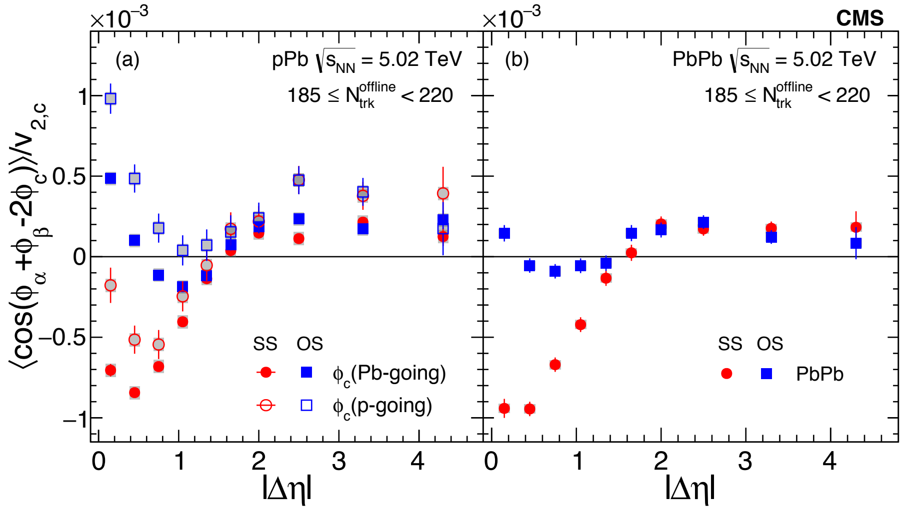

Figure 6.3 : The same (SS) and opposite sign (OS) three-particle correlator as a function of $|\Delta\eta| \equiv |\eta_\alpha - \eta_\beta|$ for $185 \leq N_{\text{trk}}^{\text{offline}} < 220$ in (a) pPb and (b) PbPb collisions at $\sqrt{s_{NN}} = 5.02$ TeV. The pPb results obtained with particle c in Pb-going (solid markers) and p-going (open markers) sides are shown separately. Statistical and systematic uncertainties are indicated by the error bars and shaded regions, respectively.

Measurements of the charge-dependent three-particle correlator are shown in Fig. 6.3 as a function of the pseudorapidity difference ($|\Delta\eta| \equiv |\eta_\alpha - \eta_\beta|$) between charged particles α and β with the same and opposite signs, in the multiplicity range $185 \leq N_{\text{trk}}^{\text{offline}} < 220$ for pPb and PbPb collisions at $\sqrt{s_{NN}} = 5.02$ TeV. The pPb data are obtained with particle c in the Pb- and p-going sides separately. In both pPb and PbPb systems, a charge dependence of the three-particle correlator is observed for $|\Delta\eta|$ up to about 1.6. In this range, the SS correlators show significant negative values as $|\Delta\eta|$ decreases, while the OS correlators become positive towards $|\Delta\eta| \approx 0$. For $|\Delta\eta| > 1.6$, the SS and OS correlators converge to a common positive value, which is weakly dependent on $|\Delta\eta|$ up to about 4.8 units. Similar $|\Delta\eta|$ dependence of the three-particle correlator has been reported at $\sqrt{s_{NN}} = 0.2$ TeV [109] and 2.76 TeV [64], measured up to $|\Delta\eta| \approx 1.6$. In pPb collisions, three-particle correlators obtained with particle c from the p-going side are shifted toward more positive values than those from the Pb-going side by approximately the same amount for both the SS and OS pairs. The Pb-going side results for the pPb collisions are of similar magnitude as the results for PbPb collisions. The common shift of SS and OS correlators between the p- and Pb-going side reference (c) particle, may be related to sources of correlations that are charge-independent, such as directed flow and the momentum conservation effect, the latter being sensitive to the difference in multiplicity between p- and Pb-going directions.

To explore the multiplicity or centrality dependence of the three-particle correlator, an average of the results in Fig. 6.3 over $|\Delta\eta| < 1.6$ (charge-dependent region) is taken, where the average is weighted by the number of particle pairs in each $|\Delta\eta|$ range. The resulting $|\Delta\eta|$-averaged three-particle correlators are shown in Fig. 6.4 as a function of $N_{\mathrm{trk}}^{\mathrm{offline}}$ for pPb (particle c from the Pb-going side) and PbPb collisions at $\sqrt{s_{NN}} = 5.02$ TeV. Up to $N_{\mathrm{trk}}^{\mathrm{offline}} = 300$, the pPb and PbPb results are measured in the same $N_{\mathrm{trk}}^{\mathrm{offline}}$ ranges. The centrality scale on the top of Fig. 6.4 relates to the PbPb experimental results. Within uncertainties, the SS and OS correlators in pPb and PbPb collisions exhibit the same magnitude and trend as a function of event multiplicity. The OS correlator reaches a value close to zero for $N_{\mathrm{trk}}^{\mathrm{offline}} > 200$, while the SS correlator remains negative, but the magnitude gradually decreases as $N_{\mathrm{trk}}^{\mathrm{offline}}$ increases. Part of the observed multiplicity (or centrality) dependence is understood

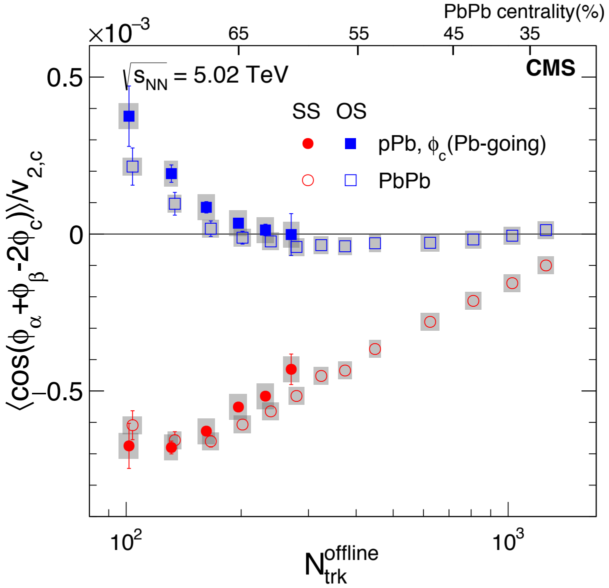

Figure 6.4 : The same sign (SS) and opposite sign (OS) three-particle correlator averaged over $|\eta_\alpha - \eta_\beta| < 1.6$ as a function of $N_{\mathrm{trk}}^{\mathrm{offline}}$ in pPb and PbPb collisions at $\sqrt{s_{NN}} = 5.02$ TeV are shown. Statistical and systematic uncertainties are indicated by the error bars and shaded regions, respectively.

as a dilution effect that falls with the inverse of event multiplicity [20]. The notably similar magnitude and multiplicity dependence of the three-particle correlator observed in pPb collisions relative to that in PbPb collisions again indicates that the dominant contribution of the signal is not related to the CME. The results of SS and OS three-particle correlators as functions of centrality in PbPb collisions at $\sqrt{s_{NN}} = 5.02$ TeV are also found to be consistent with the results from lower energy AA collisions [20, 64].

To eliminate sources of correlations that are charge independent (e.g., directed flow, v_1) and to explore a possible charge separation effect generated by the CME, the difference of three-particle correlators between OS and SS is shown as a function of $|\Delta\eta|$ in the multiplicity range $185 \leq N_{\mathrm{trk}}^{\mathrm{offline}} < 220$ (Fig. 6.5 (a)) and as a function

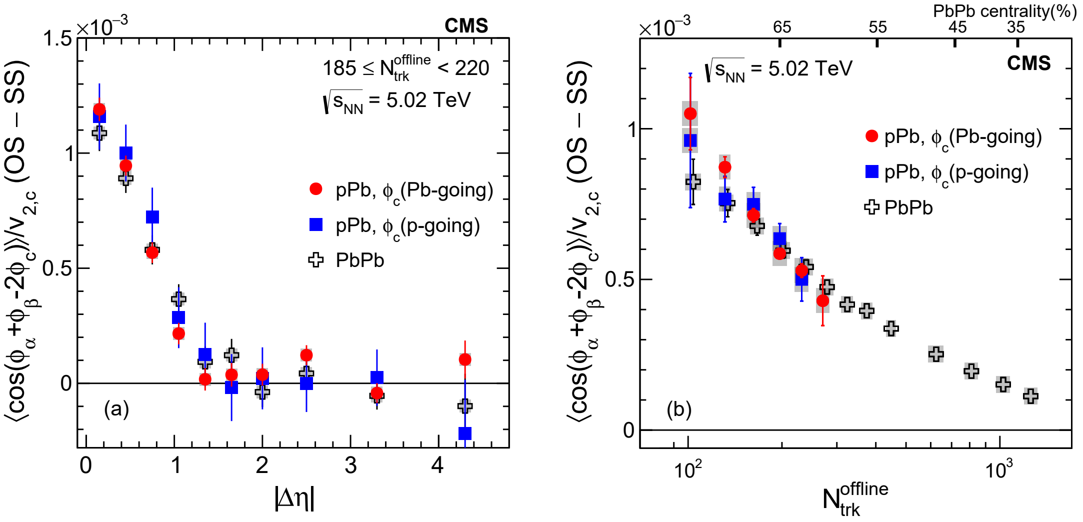

Figure 6.5 : The difference of the opposite sign (OS) and same sign (SS) three-particle correlators (a) as a function of $|\eta_\alpha - \eta_\beta|$ for $185 \leq N_{\mathrm{trk}}^{\mathrm{offline}} < 220$ and (b) as a function of $N_{\mathrm{trk}}^{\mathrm{offline}}$, averaged over $|\eta_\alpha - \eta_\beta| < 1.6$, in pPb and PbPb collisions at $\sqrt{s_{NN}} = 5.02$ TeV. The pPb results are obtained with particle c from Pb- and p-going sides separately. Statistical and systematic uncertainties are indicated by the error bars and shaded regions, respectively.

of $N_{\mathrm{trk}}^{\mathrm{offline}}$ averaged over $|\Delta\eta| < 1.6$ (Fig. 6.5 (b),) for pPb and PbPb collisions at $\sqrt{s_{NN}} = 5.02$ TeV. After taking the difference, the pPb data with particle c from both the p- and Pb-going sides, and PbPb data, show nearly identical values. The charge-dependent difference is largest at $|\Delta\eta| \approx 0$ and drops to zero for $|\Delta\eta| > 1.6$, and also decreases as a function of $N_{\mathrm{trk}}^{\mathrm{offline}}$. The striking similarity in the observed charge-dependent azimuthal correlations strongly suggests a common physical origin. In PbPb collisions, it was suggested that the charge dependence of the three-particle correlator as well as its $|\Delta\eta|$ dependence are indications of the charge separation effect with respect to the event plane due to the CME [20, 64]. However, as argued earlier, a strong charge separation signal from the CME is not expected in a very high-multiplicity pPb collision. The similarity seen between high-multiplicity pPb and peripheral PbPb collisions challenges the attribution of the observed charge-dependent correlations to the CME. Note that there is a hint of a slight difference between pPb and PbPb in the slopes of the $N_{\mathrm{trk}}^{\mathrm{offline}}$ dependence in Fig. 6.5 (b), where the systematic uncertainties are point-to-point correlated. This difference is worth further investigation.

6.3 Results of charge-dependent azimuthal correlation with respect to the second- and third-order event plane in pPb at $\sqrt{s_{NN}}$= 8.16 TeV and PbPb collisions at $\sqrt{s_{NN}}$= 5.02 TeV

6.3.1 Charge-dependent two- and three-particle correlators

Measurements of the charge-dependent three-particle (γ_{112}, γ_{123}) and two-particle (δ) correlators are shown in Fig. 6.6 as functions of the $|\Delta\eta|$ between SS and OS particles α and β, in the multiplicity range $185 \leq N_{\mathrm{trk}}^{\mathrm{offline}} < 250$ for pPb collisions at $\sqrt{s_{NN}} = 8.16$TeV and PbPb collisions at 5.02 TeV. The SS and OS of δ correlators are shown with different markers to differentiate the two-particle correlation from the three-particle correlation with a particle c in the forward rapidity. The pPb data are obtained with particle c in the Pb- and p-going sides separately. The multiplicity range $185 \leq N_{\mathrm{trk}}^{\mathrm{offline}} < 250$ for PbPb data roughly corresponds to the centrality range 60–65%.

Similar to the observation reported in Ref. [87], the three-particle γ_{112} (Figs. 6.6a and 6.6b) and γ_{123} (Figs. 6.6c and 6.6d) correlators show a charge dependence for $|\Delta\eta|$ up to about 1.6, in both pPb (5.02 [87] and 8.16 TeV) and PbPb (5.02 TeV) systems. Little collision energy dependence of the γ_{112} data for pPb collisions is found

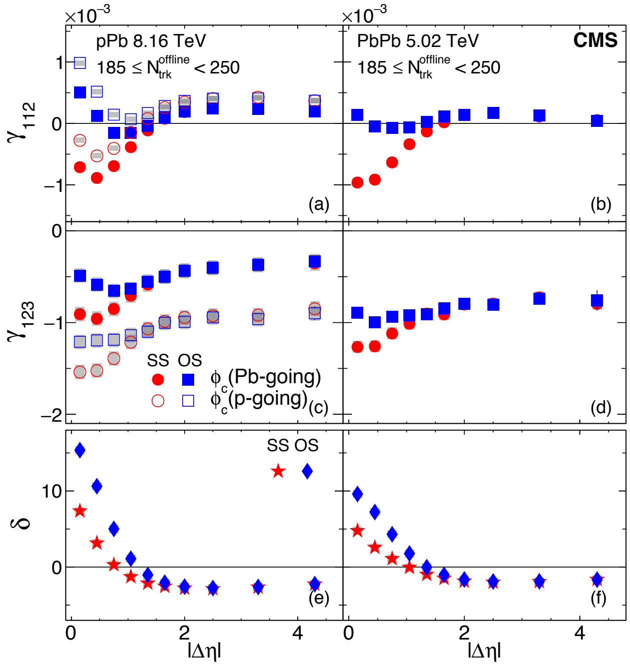

Figure 6.6 : The SS and OS three-particle correlators, γ_{112} (upper) and γ_{123} (middle), and two-particle correlator, δ (lower), as a function of $|\Delta\eta|$ for $185 \leq N_{\text{trk}}^{\text{offline}} < 250$ in pPb collisions at $\sqrt{s_{NN}} = 8.16$ TeV (left) and PbPb collisions at 5.02 TeV (right). The pPb results obtained with particle c in Pb-going (solid markers) and p-going (open markers) sides are shown separately. The SS and OS two-particle correlators are denoted by different markers for both pPb and PbPb collisions. Statistical and systematic uncertainties are indicated by the error bars and shaded regions, respectively.

from $\sqrt{s_{NN}} = 5.02$TeV to 8.16 TeV within uncertainties (as will be shown later in Figs. 6.9 and 6.11 as a function of event multiplicity). For $|\Delta\eta| > 1.6$, the SS and OS correlators converge to a common value, which is weakly dependent on $|\Delta\eta|$ out to about 4.8 units. In pPb collisions, the γ_{112} correlator obtained with particle c from the p-going side is shifted toward more positive values than that from the Pb-going side by approximately the same amount for both the SS and OS pairs. This trend is reversed for the higher-order harmonic γ_{123} correlator, where the Pb-going side data are more positive than the p-going side data. The Pb-going side results for the

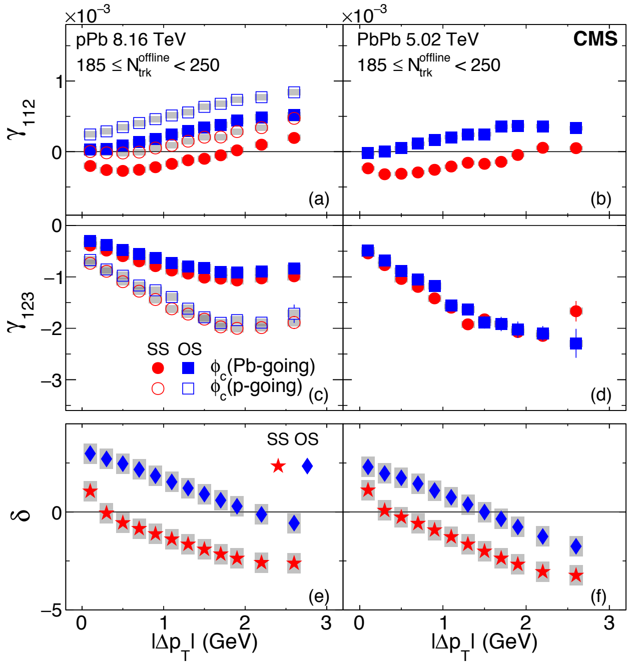

Figure 6.7 : The SS and OS three-particle correlators, γ_{112} (upper) and γ_{123} (middle), and two-particle correlator, δ (lower), as a function of $|\Delta p_{\mathrm{T}}|$ for $185 \leq N_{\mathrm{trk}}^{\mathrm{offline}} < 250$ in pPb collisions at $\sqrt{s_{NN}} = 8.16$ TeV (left) and PbPb collisions at 5.02 TeV (right) collisions. The pPb results obtained with particle c in Pb-going (solid markers) and p-going (open markers) sides are shown separately. The SS and OS two-particle correlators are denoted by different markers for both pPb and PbPb collisions. Statistical and systematic uncertainties are indicated by the error bars and shaded regions, respectively.

γ_{112} correlator for the pPb collisions are of similar magnitude as the results for PbPb collisions, although a more pronounced peak structure at small $|\Delta\eta|$ is observed in pPb collisions. The common shift of SS and OS correlators between the p- and Pb-going side reference (c) particle may be related to sources of correlation that are charge independent, such as directed flow (the first-order azimuthal anisotropy in Eq. (2.3)) and the momentum conservation effect, the latter being sensitive to the difference in multiplicity between p- and Pb-going directions. The two-particle δ correlators (Figs. 6.6e and 6.6f) for both SS and OS pairs also show a decreasing trend as $|\Delta\eta|$

increases and converge to the same values at $|\Delta\eta| \approx 1.6$, similar to that for the three-particle correlators. The values of both OS and SS δ correlators are found to be larger in pPb than in PbPb collisions at similar multiplicities. As the δ correlator is sensitive to short-range jet-like correlations, reflected by the low-$|\Delta\eta|$ region, this effect may be related to the higher-p_{T} jets or clusters in pPb compared to PbPb collisions at similar multiplicities, as suggested in Ref. [83], because of short-range two-particle $\Delta\eta$–$\Delta\phi$ correlations.

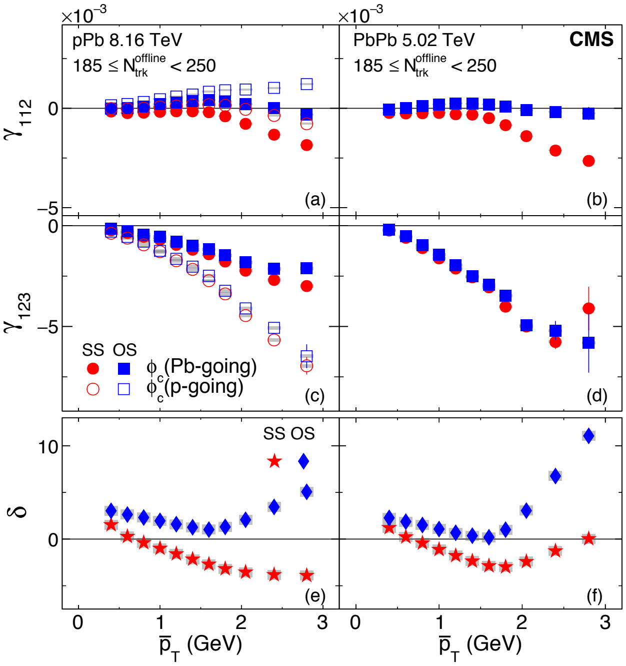

Figure 6.8 : The SS and OS three-particle correlators, γ_{112} (upper) and γ_{123} (middle), and two-particle correlator, δ (lower), as a function of $\overline{p}_{\mathrm{T}}$ for $185 \leq N_{\mathrm{trk}}^{\mathrm{offline}} < 250$ in pPb collisions at $\sqrt{s_{NN}} = 8.16$ TeV (left) and PbPb collisions at 5.02 TeV (right). The pPb results obtained with particle c in Pb-going (solid markers) and p-going (open markers) sides are shown separately. The SS and OS two-particle correlators are denoted by different markers for both pPb and PbPb collisions. Statistical and systematic uncertainties are indicated by the error bars and shaded regions, respectively.

To provide more detailed information on the particle p_{T} dependence of the correlations, the γ_{112}, γ_{123}, and δ correlators are measured as functions of the p_{T} difference ($|\Delta p_{\mathrm{T}}| \equiv |p_{\mathrm{T},\alpha} - p_{\mathrm{T},\beta}|$) and average ($\overline{p}_{\mathrm{T}} \equiv (p_{\mathrm{T},\alpha} + p_{\mathrm{T},\beta})/2$) of the SS and OS pairs in pPb and PbPb collisions, and shown in Figs. 6.7 and 6.8. The $|\Delta p_{\mathrm{T}}|$- and $\overline{p}_{\mathrm{T}}$-dependent results are averaged over the full $|\eta| < 2.4$ range. In particular, the charge-dependent correlations from the CME are expected to be strongest in the low-p_{T} region [56].

For all correlators, similar behaviors between pPb and PbPb data are again observed. The trends in $|\Delta p_{\mathrm{T}}|$ for γ_{112} and γ_{123} correlators seem to be opposite. The γ_{112} correlator increases as a function of $|\Delta p_{\mathrm{T}}|$, while a decreasing trend is seen for the γ_{123} correlator up to $|\Delta p_{\mathrm{T}}| \approx 2$ GeV, where γ_{123} becomes constant in $|\Delta p_{\mathrm{T}}|$. The opposite behavior observed between the γ_{112} and γ_{123} correlators is related to back-to-back jet-like correlations, which give a positive (negative) contribution to even- (odd-) order Fourier harmonics [113]. The δ correlators decrease monotonically as functions of $|\Delta p_{\mathrm{T}}|$ for both SS and OS pairs in pPb and PbPb collisions. This trend of decreasing for δ is consistent with the expectation from either transverse momentum conservation or back-to-back jet correlations [66].

In terms of the $\overline{p}_{\mathrm{T}}$ dependence in Fig. 6.8, all three correlators for both SS and OS pairs show very similar behaviors in the low-$\overline{p}_{\mathrm{T}}$ region, which is likely a consequence of the same physical origin. However, an opposite trend starts emerging at $\overline{p}_{\mathrm{T}} \approx 1.6$ GeV, most evidently for γ_{112} and δ. Within the $0.3 < p_{\mathrm{T}} < 3$ GeV range, as $\overline{p}_{\mathrm{T}}$ increases toward 3 GeV, both particles of a pair tend to be selected with a high-p_{T} value, while for low-$\overline{p}_{\mathrm{T}}$ or any $|\Delta p_{\mathrm{T}}|$ values, the pair usually consists of at least one low-p_{T} particle. This may be the reason for a different trend seen at high $\overline{p}_{\mathrm{T}}$. The qualitative behavior of the data is captured by the A Multi-Phase Transport model [114, 115]. In Appendix A.3, all three correlators as functions of $|\Delta\eta|$, Δp_{T}, and $\overline{p}_T$ in different multiplicity and centrality ranges in pPb and PbPb collisions, can be found.

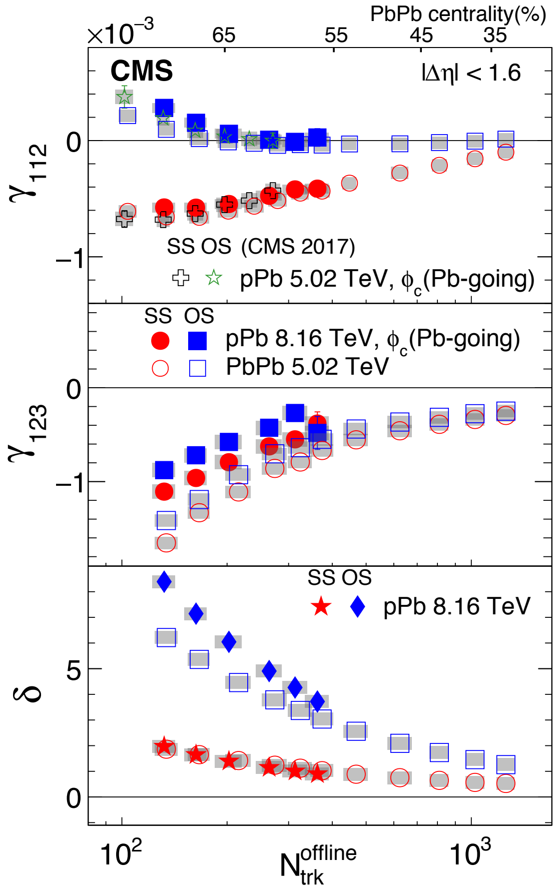

Figure 6.9 : The SS and OS three-particle correlators, γ_{112} (upper) and γ_{123} (middle), and two-particle correlator, δ (lower), averaged over $|\Delta\eta| < 1.6$ as a function of $N_{\mathrm{trk}}^{\mathrm{offline}}$ in pPb collisions at $\sqrt{s_{NN}} = 8.16$ TeV and PbPb collisions at 5.02 TeV. The SS and OS two-particle correlators are denoted by different markers for pPb collisions. The results of γ_{112} for pPb collisions at 5.02 TeV from CMS Collaboration (CMS 2017: [87]), are also shown for comparison. Statistical and systematic uncertainties are indicated by the error bars and shaded regions, respectively.

To explore the multiplicity or centrality dependence of the three- and two-particle correlators, an average of the data is taken over $|\Delta\eta| < 1.6$, corresponding to the region in Fig. 6.6 which exhibits charge dependence. The average over $|\Delta\eta| < 1.6$

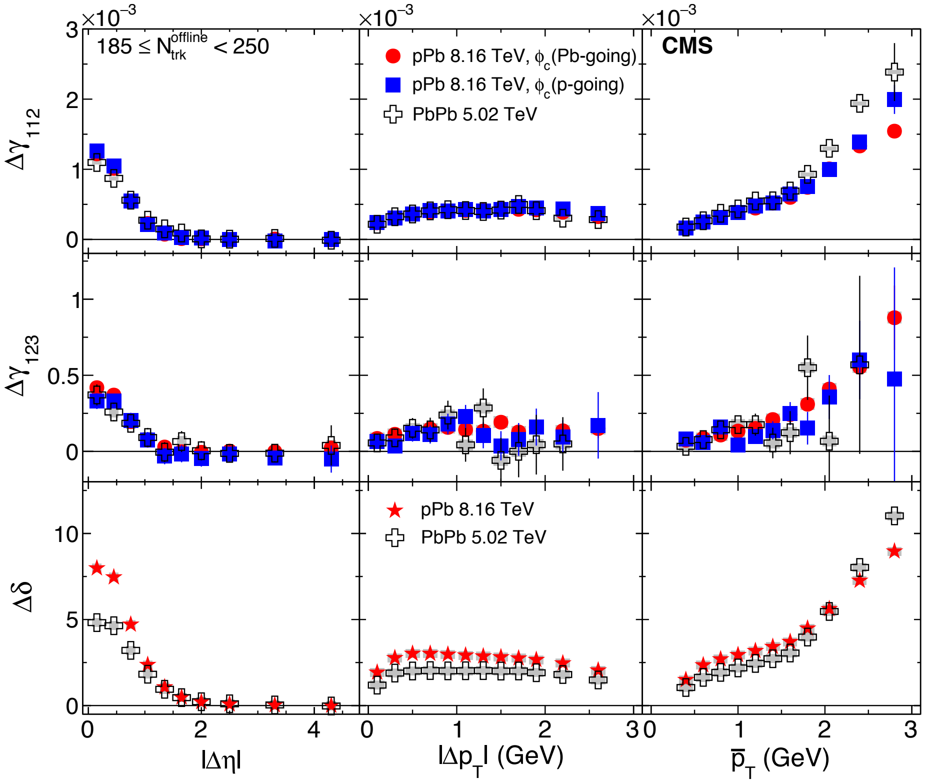

Figure 6.10 : The difference of the OS and SS three-particle correlators, γ_{112} (upper) and γ_{123} (middle), and two-particle correlator, δ (lower) as functions of $\Delta\eta$ (left), Δp_{T} (middle), and $\overline{p}_{\mathrm{T}}$ (right) for $185 \leq N_{\mathrm{trk}}^{\mathrm{offline}} < 250$ in pPb collisions at $\sqrt{s_{_{NN}}} = 8.16$ TeV and PbPb collisions at 5.02 TeV. The $\Delta\delta$ correlator is denoted by a different marker for pPb collisions. The pPb results are obtained with particle c from Pb- and p-going sides separately. Statistical and systematic uncertainties are indicated by the error bars and shaded regions, respectively.

is weighted by the density of particle pairs in $|\Delta\eta|$, and all further plots averaged over $|\Delta\eta| < 1.6$ are weighted similarly. The resulting $|\Delta\eta|$-averaged data of γ_{112}, γ_{123} and δ are shown in Fig. 6.9 for both OS and SS pairs, as functions of $N_{\mathrm{trk}}^{\mathrm{offline}}$ for pPb collisions at $\sqrt{s_{_{NN}}} = 8.16$ TeV (particle c from the Pb-going side) and PbPb collisions at 5.02 TeV. Previously published pPb data at 5.02 TeV are also shown for comparison [87]. The centrality scale on the top of Fig. 6.9 relates to the PbPb experimental results. Up to $N_{\mathrm{trk}}^{\mathrm{offline}} = 400$, the pPb and PbPb results are measured in the same $N_{\rm trk}^{\rm offline}$ ranges. The new pPb data at 8.16 TeV extend the multiplicity reach further than the previously published pPb data at 5.02 TeV (which stopped at $N_{\rm trk}^{\rm offline} \approx 300$).

Within the uncertainties, the SS and OS γ_{112} correlators in pPb and PbPb collisions exhibit the same magnitude and trend as functions of event multiplicity. The pPb data are independent of collision energy from 5.02 to 8.16 TeV at similar multiplicities. This justifies the comparison of new pPb data and PbPb data at somewhat different energies. For both pPb and PbPb collisions, the OS correlator reaches a value close to zero for $N_{\rm trk}^{\rm offline} > 200$, while the SS correlator remains negative, but the magnitude gradually decreases as $N_{\rm trk}^{\rm offline}$ increases. Part of the observed multiplicity (or centrality) dependence is understood as a dilution effect that falls with the inverse of event multiplicity [20]. The notably similar magnitude and multiplicity dependence of the three-particle correlator, γ_{112}, observed in pPb collisions relative to that in PbPb collisions again indicates that the dominant contribution of the signal is not related to the CME. The results of SS and OS three-particle correlators as functions of centrality in PbPb collisions at $\sqrt{s_{_{NN}}} = 5.02$ TeV are also found to be consistent with the results from lower energy AA collisions [20,64]. However, values of γ_{123} correlators between pPb and PbPb are observed to be different, unlike those for γ_{112} correlators. As the CME contribution to γ_{123} is not expected, the data suggest different properties of backgrounds in pPb and PbPb systems. If the γ_{112} correlator in pPb data is expected to be background dominated, as argued earlier, the similarity found to the PbPb data in γ_{112} requires further understanding. The two-particle δ correlators show a similar trend in multiplicity between pPb and PbPb systems, but a larger splitting between OS and SS pairs is observed in pPb than in PbPb data.

To eliminate sources of correlations that are charge independent (e.g., directed

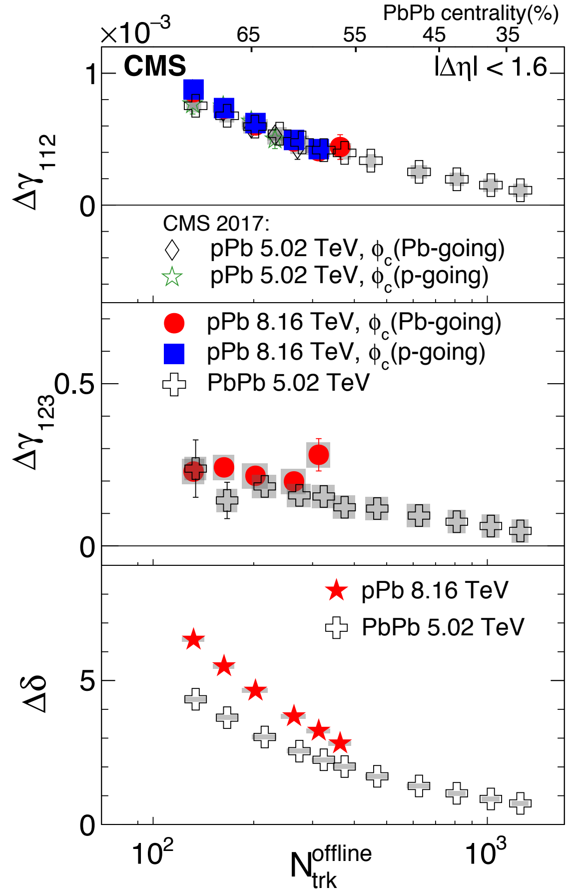

Figure 6.11 : The difference of the OS and SS three-particle correlators, γ_{112} (upper) and γ_{123} (middle), and two-particle correlator, δ (lower), averaged over $|\Delta\eta| < 1.6$ as a function of $N_{\rm trk}^{\rm offline}$ in pPb collisions at $\sqrt{s_{NN}}$ = 8.16 TeV and PbPb collisions at 5.02 TeV. The pPb results are obtained with particle c from Pb- and p-going sides separately. The $\Delta\delta$ correlator is denoted by a different marker for pPb collisions. The results of γ_{112} for pPb collisions at 5.02 TeV from CMS Collaboration (CMS 2017: [87]), are also shown for comparison. Statistical and systematic uncertainties are indicated by the error bars and shaded regions, respectively.

flow, v_1) and to explore a possible charge separation effect generated by the CME or charge-dependent background correlations, the differences of three-particle correlators, $\Delta\gamma_{112}$ and $\Delta\gamma_{123}$, and two-particle correlator, $\Delta\delta$, between OS and SS are shown in Fig. 6.10 as functions of $|\Delta\eta|$, $|\Delta p_{\mathrm{T}}|$, and $\overline{p}_{\mathrm{T}}$ in the multiplicity range $185 \leq N_{\mathrm{trk}}^{\mathrm{offline}} < 250$ for pPb collisions at $\sqrt{s_{_{NN}}} = 8.16$ TeV and PbPb collisions at 5.02 TeV.

After taking the difference, the three-particle correlators, $\Delta\gamma_{112}$ and $\Delta\gamma_{123}$, in pPb collisions with particle c from either the p- or Pb-going side, and in PbPb collisions, show nearly identical values, except in the high $\overline{p}_{\mathrm{T}}$ region. Note that for OS and SS correlators separately, this similarity between pPb and PbPb is only observed for the γ_{112} correlator. As a function of $|\Delta\eta|$, the charge-dependent difference is largest at $|\Delta\eta| \approx 0$ and drops to zero for $|\Delta\eta| > 1.6$ for both systems. The striking similarity in the observed charge-dependent azimuthal correlations between pPb and PbPb as functions of $|\Delta\eta|$, $|\Delta p_{\mathrm{T}}|$ and $\overline{p}_{\mathrm{T}}$ strongly suggests a common physical origin. As argued in Ref. [87], a strong charge separation signal from the CME is not expected in a very high-multiplicity pPb collisions, and not with respect to Ψ_3 (for the γ_{123} correlator) in either the pPb or PbPb system. The similarity seen between high-multiplicity pPb and peripheral PbPb collisions for both $\Delta\gamma_{112}$ and $\Delta\gamma_{123}$ further challenges the attribution of the observed charge-dependent correlations to the CME. The two-particle correlator, $\Delta\delta$, on the other hand, is found to show a larger value in pPb than in PbPb collisions.

The differences of three-particle correlators, $\Delta\gamma_{112}$ and $\Delta\gamma_{123}$, and two-particle correlator, $\Delta\delta$, between OS and SS are shown in Fig. 6.11 as functions of $N_{\mathrm{trk}}^{\mathrm{offline}}$ averaged over $|\Delta\eta| < 1.6$ for pPb collisions at $\sqrt{s_{_{NN}}} = 8.16$ TeV and PbPb collisions at 5.02 TeV. For comparison, previously published pPb data at 5.02 TeV are also

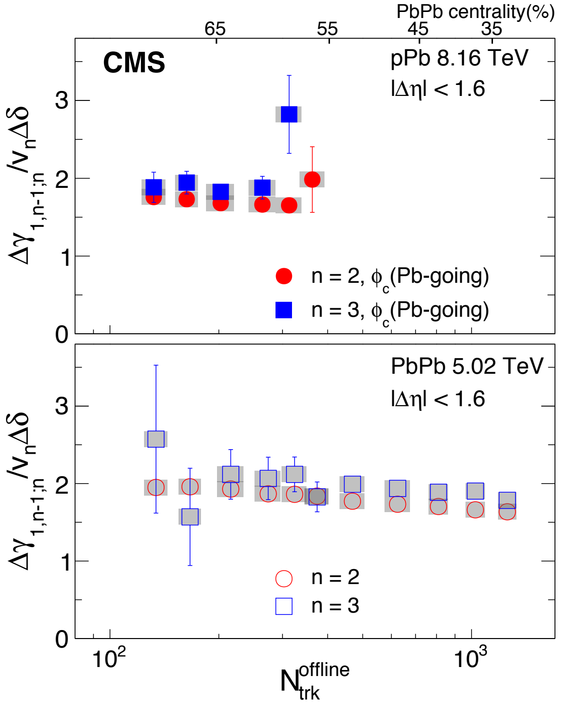

Figure 6.12 : The ratio of $\Delta\gamma_{112}$ and $\Delta\gamma_{123}$ to the product of v_n and δ, averaged over $|\Delta\eta| < 1.6$, in pPb collisions for the Pb-going direction at $\sqrt{s_{NN}} = 8.16$ TeV (upper) and PbPb collisions at 5.02 TeV (lower). Statistical and systematic uncertainties are indicated by the error bars and shaded regions, respectively.

shown [87]. Similar to those shown in Fig. 6.10, the observed difference between OS and SS pairs in $\Delta\gamma_{112}$ and $\Delta\gamma_{123}$ is strikingly similar in pPb and PbPb collisions over the entire overlapping multiplicity range (and also independent of collision energy for $\Delta\gamma_{112}$ in pPb), while higher values of an OS-SS difference in $\Delta\delta$ are found for the pPb system.

6.3.2 κ parameter for second- and third-order harmonics

To check if the mechanism of local charge conservation coupled with anisotropic flow can explain the observed charge dependence of the $\Delta\gamma_{112}$ and $\Delta\gamma_{123}$ correlators, the relation in Eq. (6.3) is used. The ratios of $\Delta\gamma_{112}$ and $\Delta\gamma_{123}$ to the product of $\Delta\delta$ and

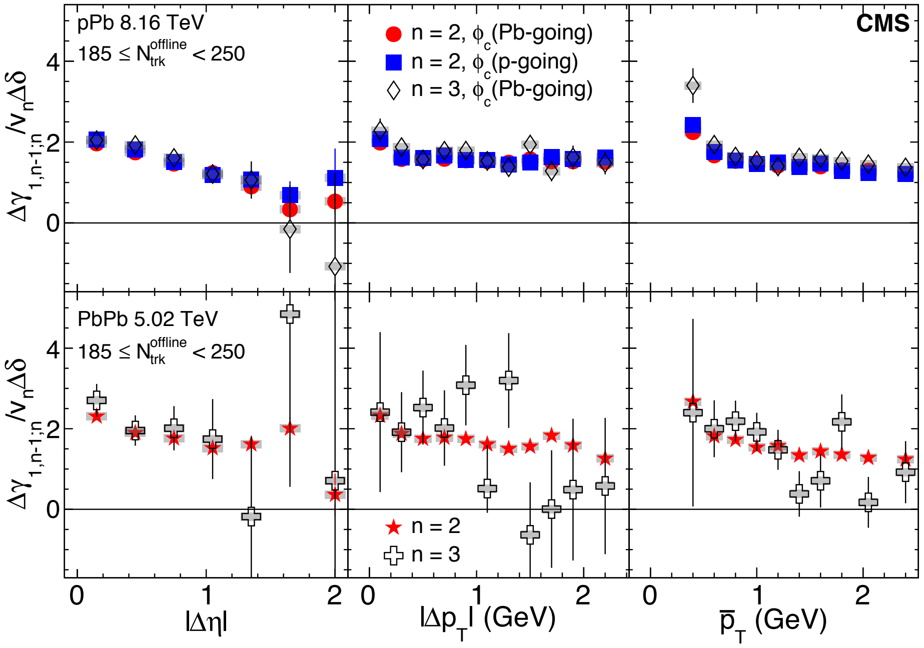

Figure 6.13 : The ratio of $\Delta\gamma_{112}$ and $\Delta\gamma_{123}$ to the product of v_n and δ, as functions of $\Delta\eta$ (left), Δp_{T} (middle), and $\bar{p}_{\mathrm{T}}$ (right) for $185 \leq N_{\mathrm{trk}}^{\mathrm{offline}} < 250$ in pPb collisions at $\sqrt{s_{NN}} = 8.16$ TeV (upper) and PbPb collisions at 5.02 TeV (lower). Statistical and systematic uncertainties are indicated by the error bars and shaded regions, respectively.

v_n are shown in Fig. 6.12, averaged over $|\Delta\eta| < 1.6$, as functions of event multiplicity in pPb and PbPb collisions. The v_2 and v_3 values for particles α or β are calculated with the scalar-product method with respect to the particle c. In pPb collisions, only results with the Pb-going direction are shown because the p-going direction data lack statistical precision, except for the multiplicity range $185 \leq N_{\mathrm{trk}}^{\mathrm{offline}} < 250$.

The ratios shown in Fig. 6.12 for both systems are found to be similar between n=2 and n=3, on average with values slightly less than 2. This observation indicates that the measured charge dependence of three-particle correlators is consistent with mostly being dominated by charge-dependent two-particle correlations (e.g., from local charge conservation) coupled with the anisotropic flow v_n. For a given n value, the ratios are also similar between pPb and PbPb collisions (and may reflect similar particle kinematics and acceptances), and approximately constant as functions of event multiplicity. Notably, the $\Delta\delta$ in Fig. 6.11 are different between the pPb and PbPb systems. However, the anisotropic flow harmonics v_n are larger for PbPb collisions than for pPb collisions [83]. As a result, the product of $\Delta\delta$ and v_n leads to similar values of $\Delta\gamma_{112}$ and $\Delta\gamma_{123}$ correlators between the pPb and PbPb systems, implying the κ_2 is similar to κ_3.

The ratios of $\Delta\gamma_{112}$ and $\Delta\gamma_{123}$ to the product of $\Delta\delta$ and v_n can also be studied as functions of $|\Delta\eta|$, Δp_{T}, and $\overline{p}_{\mathrm{T}}$ in pPb and PbPb collisions, as shown in Fig. 6.13 for the multiplicity range of $185 \leq N_{\mathrm{trk}}^{\mathrm{offline}} < 250$. Here, the v_n are calculated as the average v_n of particles α and β, $v_n = (v_{n,\alpha} + v_{n,\beta})/2$ (based on the relation derived in Eq. (A.5) in Appendix A.1), and are weighted by the number of pairs of particles α and β in the given kinematic ranges when averaged over η or p_{T}. The ratios involving $\Delta\gamma_{112}$ and $\Delta\gamma_{123}$ are again found to be similar differentially for all three variables in both pPb and PbPb collisions. This observation further supports a common origin of $\Delta\gamma_{112}$ and $\Delta\gamma_{123}$ from charge-dependent two-particle correlations coupled with the anisotropic flow.

6.3.3 Event shape engineering

To explore directly the background scenario in Eq. (2.6) in terms of a linear dependence on v_2 for the γ_{112} correlator, results based on the ESE analysis are presented in this section.

The SS and OS three-particle correlators, γ_{112}, averaged over $|\Delta\eta| < 1.6$, are shown as a function of v_2 (evaluated as the average v_2 value for each corresponding q_2 event class in Fig. 6.14), for the multiplicity range $185 \leq N_{\mathrm{trk}}^{\mathrm{offline}} < 250$ in pPb

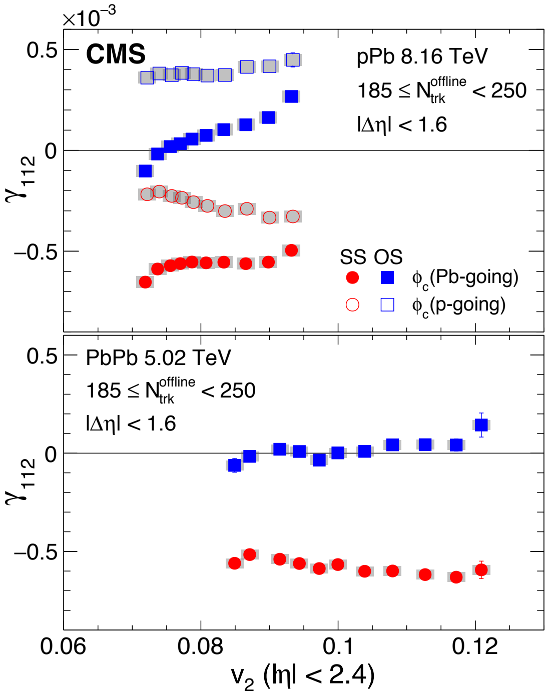

Figure 6.14 : The SS and OS three-particle correlators, γ_{112}, averaged over $|\Delta\eta| < 1.6$ as a function of v_2 (evaluated as the average v_2 value for each corresponding q_2 event class), for the multiplicity range $185 \leq N_{\mathrm{trk}}^{\mathrm{offline}} < 250$ in pPb collisions at $\sqrt{s_{NN}} = 8.16$ TeV (upper) and PbPb collisions at 5.02 TeV (lower). The pPb results are obtained with particle c from Pb- and p-going sides separately. Statistical and systematic uncertainties are indicated by the error bars and shaded regions, respectively.

collisions at $\sqrt{s_{NN}} = 8.16$ TeV (upper) and PbPb collisions at 5.02 TeV (lower). The pPb results are obtained with particle c from the Pb- and p-going sides separately.

Both SS and OS γ_{112} correlators in both pPb (both beam directions for particle c) and PbPb collisions show a dependence on v_2. A clear linear dependence on the v_2 value is not seen for any of the SS and OS correlators studied.

Similar to the analysis in Section 6.3.1, the difference between OS and SS correlators is taken in order to eliminate the charge-independent sources of the correlators. The results, averaged over $|\Delta\eta| < 1.6$, are shown in Fig. 6.15 (upper) , as a function of v_2 evaluated in each q_2 class, for the multiplicity range $185 \leq N_{\mathrm{trk}}^{\mathrm{offline}} < 250$ in pPb

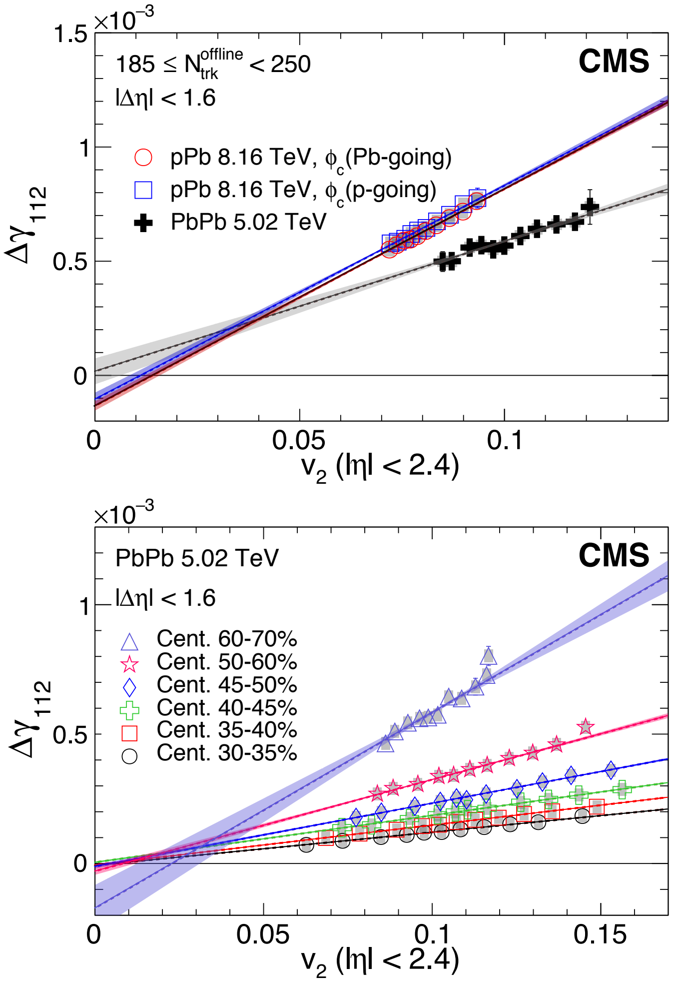

Figure 6.15 : The difference of the OS and SS three-particle correlators, γ_{112}, averaged over $|\Delta\eta| < 1.6$ as a function of v_2 evaluated in each q_2 class, for the multiplicity range $185 \leq N_{\mathrm{trk}}^{\mathrm{offline}} < 250$ in pPb collisions at $\sqrt{s_{NN}} = 8.16$ TeV and PbPb collisions at 5.02 TeV (upper), and for different centrality classes in PbPb collisions at 5.02 TeV (lower). Statistical and systematic uncertainties are indicated by the error bars and shaded regions, respectively. A one standard deviation uncertainty from the fit is also shown.

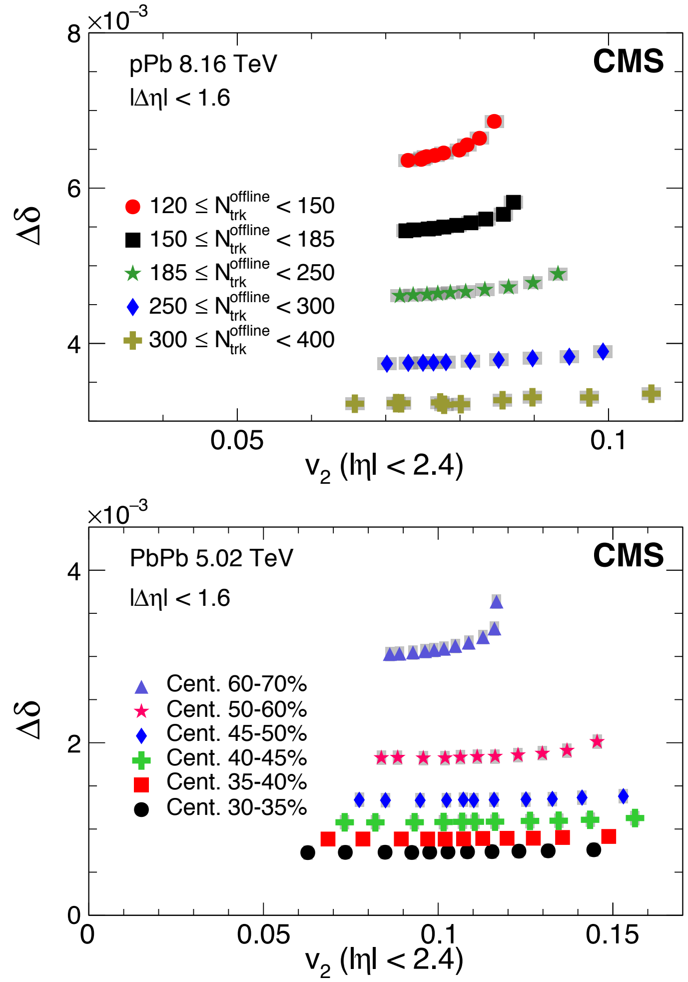

Figure 6.16 : The difference of the OS and SS two-particle correlators, δ, averaged over $|\Delta\eta| < 1.6$ as a function of v_2 evaluated in each q_2 class, for different multiplicity ranges in pPb collisions at $\sqrt{s_{NN}} = 8.16$ TeV (upper), and for different centrality classes in PbPb collisions at 5.02 TeV (lower). Statistical and systematic uncertainties are indicated by the error bars and shaded regions, respectively.

collisions at $\sqrt{s_{_{NN}}} = 8.16$ TeV and PbPb collisions at 5.02 TeV. The results obtained in each centrality class of PbPb collisions at 5.02 TeV are also presented in Fig. 6.15 (lower). The lines are linear fits to the data,

$$\Delta\gamma_{112} = a\, v_2 + b, \tag{6.12}$$

where the first term corresponds to the v_2-dependent background contribution with the slope parameter a equal to $\kappa_2 \Delta\delta$ (from Eq. (2.6)), which is assumed to be v_2 independent. The intercept parameter b denotes the v_2-independent contribution (when linearly extrapolating to $v_2 = 0$) in the γ_{112} correlator. In particular, as the CME contribution to the $\Delta\gamma_{112}$ is expected to be largely v_2-independent within narrow multiplicity (centrality) ranges, the b parameter may provide an indication to a possible observation of the CME, or set an upper limit on the CME contribution.

As shown in Fig. 6.15, for both pPb and PbPb collisions in each multiplicity or centrality range, a clear linear dependence of the $\Delta\gamma_{112}$ correlator as a function of v_2 is observed. Fitted by a linear function, the intercept parameter, b, can be extracted. A one standard deviation uncertainty band is also shown for the linear fit. Taking the statistical uncertainties into account, the values of b are found to be nonzero for multiplicity range $185 \leq N_{\text{trk}}^{\text{offline}} < 250$ in pPb and 60–70% centrality in PbPb collisions.

Observing a nonzero intercept b from Fig. 6.15 may or may not lead to a conclusion of a finite CME signal, as an assumption is made for the background contribution term, namely that $\Delta\delta$ is independent of v_2. To check this assumption explicitly, the $\Delta\delta$ correlator is shown in Fig. 6.16 as a function of v_2 in different multiplicity and centrality ranges in pPb (upper) and PbPb (lower) collisions. It is observed that the value of $\Delta\delta$ remains largely constant as a function of v_2 in low- or intermediate-q_2 classes, but starts rising as v_2 increases in high-q_2 classes. The multiplicity, within a

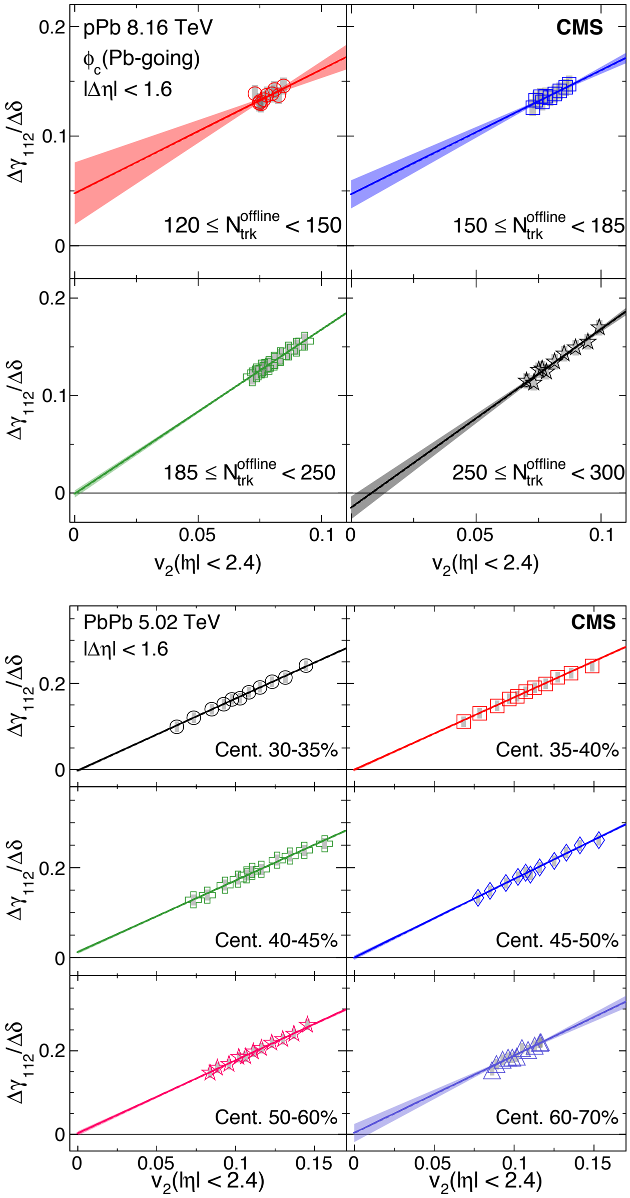

Figure 6.17 : The ratio between the difference of the OS and SS three-particle correlators and the difference of OS and SS in δ correlators, $\Delta\gamma_{112}/\Delta\delta$, averaged over $|\Delta\eta| < 1.6$ as a function of v_2 evaluated in each q_2 class, for different multiplicity ranges in pPb collisions at $\sqrt{s_{NN}} = 8.16$ TeV (upper), and for different centrality classes in PbPb collisions at 5.02 TeV (lower). Statistical and systematic uncertainties are indicated by the error bars and shaded regions, respectively. A one standard deviation uncertainty from the fit is also shown.

centrality or multiplicity range, decreases slightly with increasing q_2, which qualitatively could contribute to the rising $\Delta\delta$ due to a multiplicity dilution effect. However, this is only found to be true for PbPb collisions, but not for pPb collisions. The other reason may be related to larger jet-like correlations selected by requiring large q_2 values. Events with higher multiplicities show a weaker dependence on v_2 than those with lower multiplicities, which is consistent with the expectation that short-range jet-like correlations are stronger in peripheral events. Because of the possible bias towards larger jet-like correlations at higher q_2 from the ESE technique, the v_2 dependence of $\Delta\delta$ is hard to completely eliminate. This presents a challenge to the interpretation of the intercept values from the linear fits in Fig. 6.15.

In order to avoid the issue of $\Delta\delta$ being dependent on v_2, the ratio $\Delta\gamma_{112}/\Delta\delta$ as function of v_2 is shown in Fig. 6.17 for different multiplicity ranges in pPb collisions at $\sqrt{s_{_{NN}}} = 8.16$ TeV (upper) and for different centrality classes in PbPb collisions at 5.02 TeV (lower). Particularly in the scenario of a pure v_2-dependent background, the ratio $\Delta\gamma_{112}/\Delta\delta$ is expected to be proportional to v_2. A linear function is fitted again using

$$\frac{\Delta\gamma_{112}}{\Delta\delta} = a_{\mathrm{norm}}\, v_2 + b_{\mathrm{norm}}. \tag{6.13}$$

Here, comparing to the intercept parameter b in Eq. (6.12), the b_{norm} parameter is equivalent to b scaled by the $\Delta\delta$ factor. The fitted linear slope and intercept parameters, a_{norm} and b_{norm}, are summarized in Tables 6.1 and B.3 in $N_{\mathrm{trk}}^{\mathrm{offline}}$ and centrality classes for pPb and PbPb collisions, respectively.

The values of the intercept parameter b_{norm} are shown as a function of event multiplicity in Fig. 6.18 (upper), for both pPb and PbPb collisions. The $\pm 1\sigma$ and $\pm 2\sigma$ systematic uncertainty is shown, which correspond to a 68% and 95% confidence level (CL), respectively. Within statistical and systematic uncertainties, no significant

Table 6.1 : The summary of slope and intercept parameter a_{norm} and b_{norm} for different $N_{\mathrm{trk}}^{\mathrm{offline}}$ classes in pPb collisions, and the goodness of fit χ^2 per degree of freedom (ndf). The statistical and systematic uncertainties are shown after the central values, respectively.

$N_{\mathrm{trk}}^{\mathrm{offline}}$	a_{norm}	b_{norm}	χ^2/ndf
120–150	$1.13 \pm 0.24 \pm 0.14$	$0.048 \pm 0.019 \pm 0.012$	16.3/8
150–185	$1.13 \pm 0.19 \pm 0.04$	$0.047 \pm 0.016 \pm 0.008$	4.9/8
185–250	$1.69 \pm 0.06 \pm 0.01$	$-0.0009 \pm 0.0050 \pm 0.0078$	4.5/8
250–300	$1.83 \pm 0.13 \pm 0.15$	$-0.015 \pm 0.011 \pm 0.016$	8.1/8

Table 6.2 : The summary of slope and intercept parameter a_{norm} and b_{norm} for different centrality classes in PbPb collisions, and the goodness of fit χ^2 per degree of freedom (ndf). The statistical and systematic uncertainties are shown after the central values, respectively.

$N_{\mathrm{trk}}^{\mathrm{offline}}$	a_{norm}	b_{norm}	χ^2/ndf
60–70%	$1.85 \pm 0.17 \pm 0.21$	$0.003 \pm 0.017 \pm 0.023$	12.3/9
50–60%	$1.75 \pm 0.04 \pm 0.01$	$0.002 \pm 0.004 \pm 0.010$	11.8/9
45–50%	$1.74 \pm 0.04 \pm 0.03$	$0.000 \pm 0.005 \pm 0.011$	8.4/9
40–45%	$1.59 \pm 0.03 \pm 0.01$	$0.012 \pm 0.003 \pm 0.011$	9.1/9
35–40%	$1.68 \pm 0.03 \pm 0.01$	$-0.001 \pm 0.003 \pm 0.010$	15.1/9
30–35%	$1.67 \pm 0.04 \pm 0.01$	$-0.0026 \pm 0.0036 \pm 0.0095$	6.9/9

positive value for b_{norm} is observed for most multiplicities in pPb or centralities in PbPb collisions. For multiplicity ranges $120 \leq N_{\text{trk}}^{\text{offline}} < 150$ and $150 \leq N_{\text{trk}}^{\text{offline}} < 185$ in pPb collisions, an indication of positive values with significances of more than two standard deviations is seen. However, results in these multiplicity ranges are likely to be highly sensitive to the very limited v_2 coverage using the ESE technique, as shown in the upper panel of Fig. 6.17. Overall, the result suggests that the v_2-independent contribution to the $\Delta\gamma_{112}$ correlator is consistent with zero, and correlation data are consistent with the background-only scenario of charge-dependent two-particle correlations plus an anisotropic flow, v_n. This conclusion is consistent with that drawn from the study of higher-order harmonic three-particle correlators discussed earlier.

Based on the assumption of a nonnegative CME signal, the upper limit of the v_2-independent fraction in the $\Delta\gamma_{112}$ correlator is obtained from the Feldman–Cousins approach [116] with the measured statistical and systematic uncertainties. In Fig. 6.18 (lower), the upper limit of the fraction f_{norm}, where f_{norm} is the ratio of the b_{norm} value to the value of $\langle\Delta\gamma_{112}\rangle/\langle\Delta\delta\rangle$, is presented at 95% CL as a function of event multiplicity. The v_2-independent component of the $\Delta\gamma_{112}$ correlator is less than 8–15% for most of the multiplicity or centrality range. The combined limits from all presented multiplicities and centralities are also shown in pPb and PbPb collisions. An upper limit on the v_2-independent fraction of the three-particle correlator, or possibly the CME signal contribution, is estimated to be 13% in pPb and 7% in PbPb collisions, at 95% CL. Note that the conclusion here is based on the assumption of a CME signal independent of v_2 in a narrow multiplicity or centrality range. As pointed out in a study by the ALICE Collaboration [117], the observed CME signal may be reduced as v_2 decreases for small v_2 values (e.g., $< 6\%$), due to a weaker correlation between magnetic field and event-plane orientations as a result of initial-state fluctuations. Depending on specific models of initial-state fluctuations, the upper limits obtained in this thesis may increase relatively by about 20%, although still well within a few % level. On the other hand, covering a wide range of v_2 values in this analysis (6–15%), the v_2 dependence of the observed CME signal is minimized to the largest extent, especially for more central events. The data also rule out any significant nonlinear v_2 dependence of the observed CME signal, as suggested by Ref. [117]. Therefore, the high-precision data presented in this thesis indicate that the charge-dependent three-particle azimuthal correlations in pPb and PbPb collisions are consistent with a v_2-dependent background-only scenario, posing a significant challenge to the search for the CME in heavy ion collisions using three-particle azimuthal correlations.

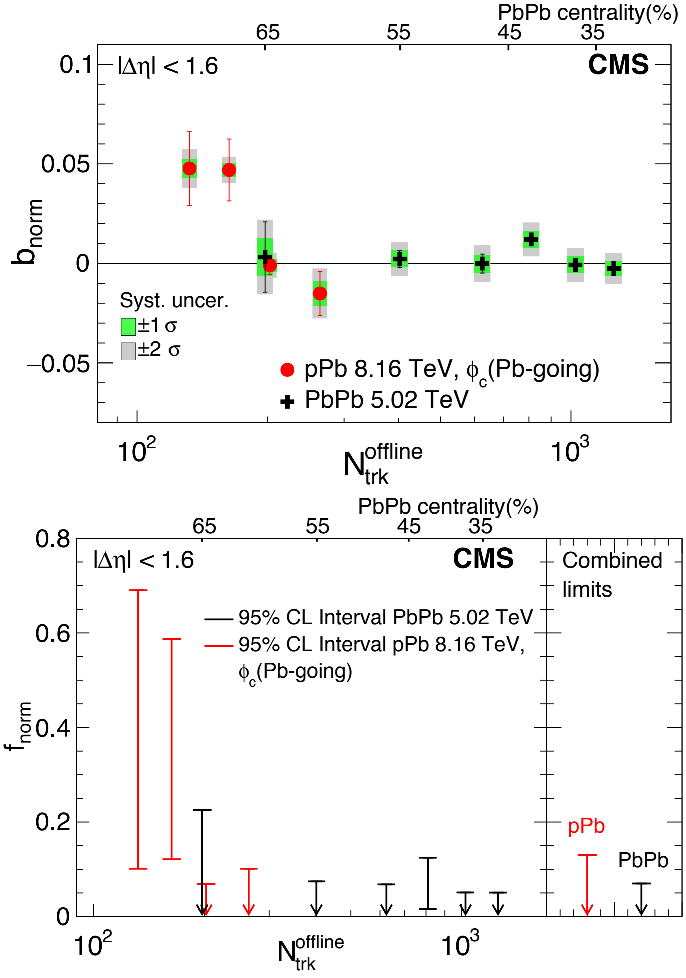

Figure 6.18 : Extracted intercept parameter b_{norm} (upper) and corresponding upper limit of the fraction of v_2-independent γ_{112} correlator component (lower), averaged over $|\Delta\eta| < 1.6$, as a function of $N_{\mathrm{trk}}^{\mathrm{offline}}$ in pPb collisions at $\sqrt{s_{NN}} = 8.16$ TeV and PbPb collisions at 5.02 TeV. Statistical and systematic uncertainties are indicated by the error bars and shaded regions in the top panel, respectively.

6.4 Summary

Charge-dependent azimuthal correlations of same- and opposite-sign (SS and OS) pairs with respect to the second- and third-order event planes have been studied in pPb collisions at $\sqrt{s_{NN}}$= 5.02 TeV and 8.16 TeV and PbPb collisions at 5.02 TeV by the CMS experiment at the LHC. The correlations are extracted via three-particle correlators as functions of pseudorapidity difference, transverse momentum difference, and p_{T} average of SS and OS particle pairs, in various multiplicity or centrality ranges of the collisions. The differences in correlations between OS and SS particles with respect to both second- and third-order event planes as functions of $\Delta\eta$ and multiplicity are found to agree for pPb and PbPb collisions, indicating a common underlying mechanism for the two systems. Dividing the OS and SS difference of the three-particle correlator by the product of the v_n harmonic of the corresponding order and the difference of the two-particle correlator, the ratios are found to be similar for the second- and third-order event planes, and show a weak dependence on event multiplicity. These observations support a scenario in which the charge-dependent three-particle correlator is predominantly a consequence of charge-dependent two-particle correlations coupled to an anisotropic flow signal.

To establish the relation between the three-particle correlator and anisotropic flow harmonic in detail, an event shape engineering technique is applied. A linear relation for the ratio of three- to two-particle correlator difference as a function of v_2 is observed, which extrapolates to an intercept that is consistent with zero within uncertainties for most of multiplicities. An upper limit on the v_2-independent fraction of the three-particle correlator, or the possible CME signal contribution (assumed independent of v_2 within the same narrow multiplicity or centrality range), is estimated to be 13% for pPb data and 7% for PbPb data at a 95% confidence level. The data presented in this thesis provide new stringent constraints on the nature of the background contribution to the charge-dependent azimuthal correlations, and establish a new baseline for the search for the chiral magnetic effect in heavy ion collisions.

Chapter 7

Search for chiral magnetic wave in pPb and PbPb collisions

This chapter presents the measurements of charge-dependent azimuthal anisotropy $v_2^{\pm}$ and $v_3^{\pm}$ in pPb and PbPb collisions at $\sqrt{s_{_{NN}}} = 5.02$ TeV at similar event charged-particle multiplicities. The charge-dependent $v_{\mathrm{n}}^{\pm}$ harmonics are investigated as a function of true event charge asymmetry $A_{\mathrm{ch}}^{\mathrm{true}}$. In order to directly compare results from different collision systems and harmonic orders, the v_{n} difference is normalized by the sum of v_{n}^{+} and v_{n}^{-}, where this new experimental approach was firstly developed in this study. The majority of work presented in this chapter is published in Ref. [118].

7.1 Analysis techniques of charge-asymmetry dependence of Fourier harmonics

7.1.1 Charge asymmetry $A_{\mathbf{ch}}$ and Fourier harmonics v_{n}

The following analysis techniques introduce the charge dependence of elliptic flow and triangular flow and its implication for searching for the CMW. The CMW evolution induces an electric quadrupole in the quark-gluon plasma, with the two poles acquiring additional positive charges and the equator acquiring additional negative charges. The formation of this charge quadrupole splits the elliptic flows of positively and negatively charged particles.

The azimuthal dependence of the particle yield can be written in terms of an harmonic expansion as,

$$\frac{dN}{d\phi} \propto N_0[1 + 2v_2 \cos(2\phi - 2\Psi_R) + ...], \tag{7.1}$$

where ϕ is the particle's azimuthal angle and N_0 is the total number of particles. If the impact-parameter direction is known, the reference angle Ψ can be taken as the azimuthal angle of the reaction plane Ψ_R as defined by the beam and impact parameter directions (see Fig. 2.4).

Since the strong radial flow aligns the azimuthal angle ϕ of emitted particle's momentum with the spatial angle, the electric quadrupole deformation translates into the difference of the yields of positive and negative charges.

$$\begin{aligned}\frac{dN_\pm}{d\phi} &\propto N_0[1 \pm A_{\text{ch}}[1 - r\cos(2\phi - 2\Psi_R)]][1 + 2v_{2,\pm}^{base}\cos(2\phi - 2\Psi_R) + ...] \qquad (7.2)\\ &\simeq N_0(1 \pm A_{\text{ch}})[1 + 2(v_{2,\pm}^{base} \mp rA_{\text{ch}})\cos(2\phi - 2\Psi_R) + ...]. \qquad (7.3)\end{aligned}$$

Here A_{ch} , the event-by-event fluctuating charge asymmetry parameter, is defined as:

$$A_{\text{ch}} \equiv \frac{N_+ - N_-}{N_+ + N_-} \tag{7.4}$$

where N_+ and N_- are number of positive and negative particles in each event.

Therefore the elliptic flow components of positive and negative particles are

$$v_{2,\pm} = v_{2,\pm}^{base} \mp rA_{\text{ch}}. \tag{7.5}$$

The quantities that are to compare CMW in different systems are the slope parameters r_{v_2} and r_{v_3}. The slope parameter is extracted by a linear function fit from $(v_2^- - v_2^+)/(v_2^- + v_2^+)$ and $(v_3^- - v_3^+)/(v_3^- + v_3^+)$ as a function of charge asymmetry parameter A_{ch}. The normalization procedure is to remove the dependence on the base values of v_{n} on the slope parameter. We denote r_n^{norm} the slope parameter for normalized v_n difference.

7.1.2 Scalar product and two-particle cumulant

In this analysis, we use the Q-cumulant method [119] to calculate the 2-particle correlations. A minimum η gap of 1 unit is applied to remove short-range correlations from jet fragmentation. The cumulants are expressed in terms of the moments of the magnitude of the corresponding flow vector Q_n, defined as:

$$Q_n \equiv \sum_{i=1}^{M} e^{in\phi_i}\,, \tag{7.6}$$

where M is the number of particles in each event. This Q vector is filled for particles taken from the tracker with $|\eta| < 2.4$, and $0.3 < p_{\mathrm{T}} < 3$ GeV. In this analysis we focus on the second and the third order, v_2 and v_3 harmonic of the azimuthal behavior,corresponding to $n = 2$ and $n = 3$, respectively.

Single-event average 2-particle azimuthal correlation is first defined as

$$\langle 2 \rangle \equiv \left\langle e^{in(\phi_1 - \phi_2)} \right\rangle \equiv \frac{1}{P_{M,2}} \sum_{i,j}{}' \, e^{in(\phi_i - \phi_j)}\,, \tag{7.7}$$

where $P_{M,2} = M!/(M-2)! = M(M-1)$. The prime in the sum $\sum'$ symbol indicates that the sums are taken with all indices different to avoid autocorrelations.

The *all-event* averaged 2-particle azimuthal correlations are defined as

$$\langle\langle 2 \rangle\rangle \equiv \left\langle\left\langle e^{in(\phi_1 - \phi_2)} \right\rangle\right\rangle \equiv \frac{\sum_{i}^{N} (W_{\langle 2 \rangle})_i \, \langle 2 \rangle_i}{\sum_{i}^{N} (W_{\langle 2 \rangle})_i}\,,$$

where N is the number of events, and $W_{\langle\rangle}$ are the event weights. The weights are chosen to be the number of particle combinations. For an event with multiplicity M, the event weight is

$$W_{\langle 2\rangle} = P_{M,2} = M(M-1) \tag{7.8}$$

The azimuthal Fourier harmonics v_n can be related to the above correlation.

$$\langle\langle 2\rangle\rangle \equiv \left\langle\left\langle e^{in(\phi_1-\phi_2)}\right\rangle\right\rangle = \left\langle\left\langle e^{in((\phi_1-\Phi_n)-(\phi_2-\Phi_n))}\right\rangle\right\rangle \tag{7.9}$$

$$= \left\langle\left\langle e^{in(\phi_1-\Phi_n)}\right\rangle\left\langle e^{-in(\phi_2-\Phi_n)}\right\rangle\right\rangle = \left\langle v_n^2\right\rangle . \tag{7.10}$$

The unbiased estimators of the true multi-particle correlations are the cumulants, defined as

$$c_n\{2\} = \langle\langle 2\rangle\rangle \tag{7.11}$$

Thus, the genuine two-particle correlation is related to the Fourier harmonics v_n by substituting into Eqn. 7.10,

$$c_n\{2\} = v_n^2 \tag{7.12}$$

We define two particle cumulant flow v_n as

$$v_n\{2\} = \sqrt{c_n\{2\}}\,, \tag{7.13}$$

In the preceeding discussion it has been assumed that all particles should receive equal weight when evaluating the cumulant expressions. To account for detector effects such as the tracking efficiency, the Q-vector expression is modified to allow for particles having different weights. We denote the particle weight per particle by w. Typically, this weight will be a function of pseudo-rapidity (η) and transverse momentum (p_T). The weight can also be a function of azimuthal angle (ϕ) to correct for a non-uniform azimuthal acceptance. However, in the pseudo-rapidity range of our analysis($|\eta| < 2.4$), the CMS detector has a very uniform ϕ acceptance and an azimuthal correction was not found needed. Thus, the general form is:

$$w = w(p_T, \eta) = \frac{1 - f_{fake}}{\mathrm{eff}(p_T, \eta)}\,, \tag{7.14}$$

where f_{fake} is the fake tracking rate, and $eff(p_T, \eta)$ is the p_T and η dependent tracking efficiency. Now, the weighted Q-vector of the n-th order harmonic is defined as:

$$Q_{n,k} \equiv \sum_{i=1}^{M} w_i^k e^{in\phi_i}\,, \tag{7.15}$$

where w_i is the weight of the i-th particle, and M is the total number of reference particles. We also introduce:

$$\begin{aligned} S_{p,k} &\equiv \left[\sum_{i=1}^{M} w_i^k\right]^p\,, &(7.16)\\ \mathcal{M}_{abcd\cdots} &\equiv {\sum_{i,j,k,l,\cdots=1}^{M}}' w_i^a w_j^b w_k^c w_l^d \cdots\,. &(7.17)\end{aligned}$$

The weighted single-event 2-particle correlations are then given by:

$$\begin{aligned} \langle 2\rangle &\equiv \frac{1}{\mathcal{M}_{11}} {\sum_{i,j=1}^{M}}' w_i w_j e^{in(\phi_i-\phi_j)} &(7.18)\\ &= \frac{|Q_{n,1}|^2 - S_{1,2}}{S_{2,1} - S_{1,2}}\,, &(7.19)\\ \mathcal{M}_{11} &\equiv {\sum_{i,j=1}^{N}}' w_i w_j &(7.20)\\ &= S_{2,1} - S_{1,2} &(7.21)\\ \langle\langle 2\rangle\rangle &= \frac{\sum_{i=1}^{N}(\mathcal{M}_{11})_i \langle 2\rangle_i}{\sum_{i=1}^{N}(\mathcal{M}_{11})_i}\,. &(7.22)\end{aligned}$$

The scalar product (SP) method, similar to the one used in Sec. 6.1.2, was first introduced by the STAR collaboration in a study of elliptic flow in AuAu collisions at $\sqrt{s_{_{NN}}} = 130$ GeV [120] is also applied for comparison,

$$v_n\{\mathrm{SP}\} \equiv \frac{\langle Q_n Q_{nA}^* \rangle}{\sqrt{\frac{\langle Q_{nA} Q_{nB}^* \rangle \langle Q_{nA} Q_{nC}^* \rangle}{\langle Q_{nB} Q_{nC}^* \rangle}}}. \tag{7.23}$$

Here, the subscripts A, B, and C refer to three separate event planes established in different regions of pseudorapidity.The particles of interest are expressed by the Q_n vector and are correlated with the A event plane. The event planes B and C effectively correct for the finite resolution of the A event plane that results from finite particle multiplicities and detector effects.

Finally, the two methods, SP and two-particle cumulant, are found in excellent agreement and the final results are presented by SP method [118].

7.1.3 Charge asymmetry correction

In order to study the v_2 as a function of $A_{\rm ch}$, the observed $A_{\rm ch}$, denoted as $A_{\rm ch}^{\rm obs}$, needs to be corrected back to the underlying true $A_{\rm ch}$, denoted as $A_{\rm ch}^{\rm true}$. The MC charge asymmetry $A_{\rm ch}$ correlation between the reconstructed level and generated level has been studied, and one example is given in Fig. 7.1 from the EPOS event generator for multiplicity range $120 \leq N_{\rm trk}^{\rm offline} < 150$ in pPb collisions at 5.02 TeV. The right hand side of Fig. 7.1 is showing the profile of the reconstructed $A_{\rm ch}$, where each point denote the average over all the generated level $A_{\rm ch}$ within a narrow reconstructed level $A_{\rm ch}$ range.

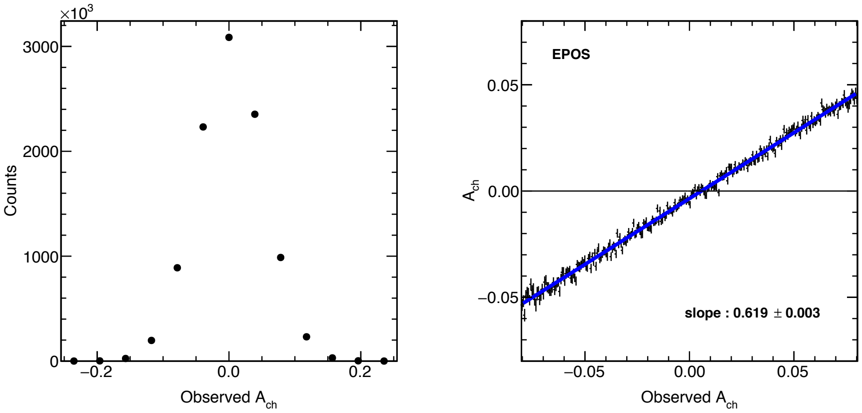

Figure 7.1 : The distribution of observed charge asymmetry $A_{\rm ch}$, and the relation between the observed charge asymmetry and the charge asymmetry from EPOS generated events for $120 \leq N_{\rm trk}^{\rm offline} < 150$ pPb collisions at 5.02 TeV

There is a smearing effect from generated to reconstructed level as the slope of the distribution is not exactly one, which is mostly caused by the tracking inefficiency. The slope of the profile (on reconstructed $A_{\rm ch}$) can be used as the correction factor, which can be applied on the final results. However, if the slope of the profile (correction factor) is completely derived from MC, then it is model dependent, driven by the generated level A_{ch} distributions in the event generators. In Fig. 7.2, the MC generated level A_{ch} distributions from two event generators, are shown.

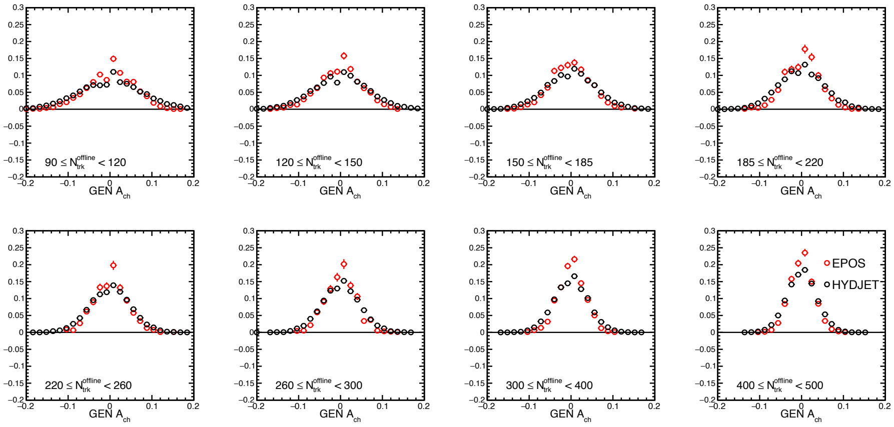

Figure 7.2 : The distribution of the generated level charge asymmetry A_{ch} distribution for EPOS and Hydjet event generators in different $N_{\mathrm{trk}}^{\mathrm{offline}}$ ranges for PbPb collisions.

The difference in the generated level A_{ch} between EPOS and Hydjet might be related to the underlying physics in the generators. For example, the EPOS LHC event generators are well known for its unrealistic flow effect and its large strange particle fractions [100], which could affect the A_{ch} distributions. Therefore, model dependent A_{ch} correction should be avoided.

Therefore, a semi-data driven method of obtaining the A_{ch} correction factors has been developed. Instead of using the generated level MC A_{ch} distributions, the particle level A_{ch} distributions in data are derived in different multiplicity (centrality) ranges, assuming the smearing process is a Gaussian, and is independent of generators from particle level to reconstructed level. After knowing the smearing distribution (a Gaussian), the particle level A_{ch} distribution in data (a Gaussian) can be obtained by $\sigma^2_{GEN} = \sigma^2_{RECO} - \sigma^2_{Smearing}$, where the σ_{GEN}, σ_{RECO}, and $\sigma_{Smearing}$ are the widths of particle level, reconstructed level, and the smearing Gaussian distribution, respectively. Therefore, in each multiplicity (centrality) ranges, the 2D correlation map between particle level and reconstructed level $A_{\rm ch}$ in data can be built by emulating the smearing process, and finally the correction factors can be derived. This process is also listed below:

- Assume the mean (μ) of the particle level $A_{\rm ch}$ is zero;
- Given the reconstructed level $A_{\rm ch}$ distributions in data, use the smearing Gaussian distribution derived from MC in bins of centrality or multiplicity, to build the particle level $A_{\rm ch}$ in data;
- Use the particle level $A_{\rm ch}$ in data and the smearing Gaussian from MC, the 2D correlation map can be obtained;
- Derive the correction factors by calculating the slope of the profile on reconstructed $A_{\rm ch}$.

The major assumption in this semi-data driven method, is whether the smearing process follows Gaussian distribution. Otherwise, the particle level $A_{\rm ch}$ distributions in data would be incorrect. Using the Hydjet event generator, this Gaussian smearing process has been indeed found to be correct, where all multiplicity ranges are found to be in agreement within a few percent. Note that the smearing distribution is the reconstructed $A_{\rm ch}$ in a narrow generated level $A_{\rm ch}$ range, where the smearing is found to be independent of where the range is chosen. Therefore, the smearing distribution in each multiplicity bin is an average of different slices of generated level $A_{\rm ch}$ distributions.

From this method, the only input depends on MC is the $\sigma_{Smearing}$, which still could be different between generators. Therefore, in Fig. 7.3, the $\sigma_{Smearing}$ as a function of $N_{\rm trk}^{\rm offline}$ for EPOS and Hydjet are shown, fitted with a parametrized function $A/\sqrt{N}+B$, where A and B are fitting parameters. The value of the $\sigma_{Smearing}$ as well as their difference between the EPOS and the Hydjet, decrease when multiplicity increases. The difference in $\sigma_{Smearing}$ will result in a difference on the correction factors, which serves as one of the major systematic uncertainties related to the final results. Since the smearing distribution is mostly driven by the event multiplicity, the correction factors are derived in the same way for pPb and PbPb collisions, given by their average multiplicity $N_{\rm trk}^{\rm offline}$ in each range.

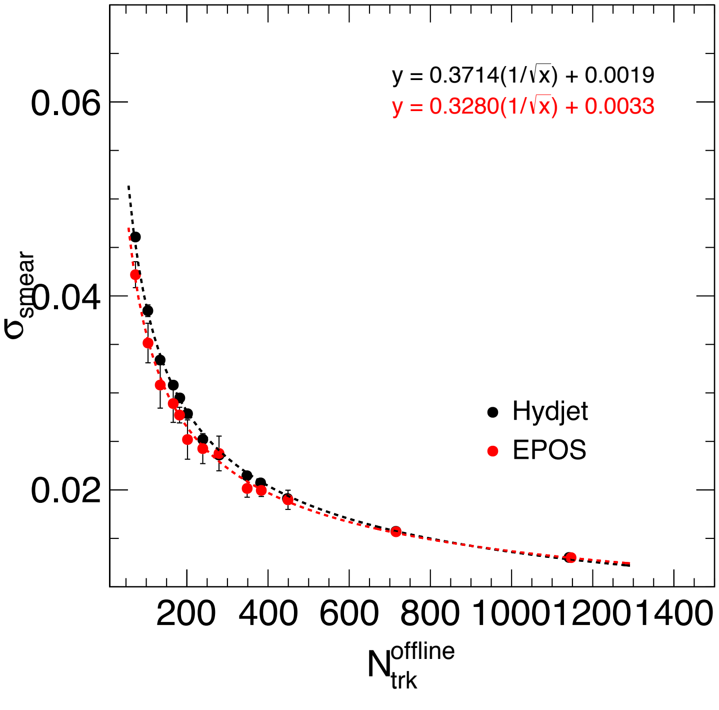

Figure 7.3 : The smearing width $\sigma_{Smearing}$ is plotted against $N_{\rm trk}^{\rm offline}$ and a function that proportional to $1/\sqrt(N)$ is used to fit for both Hydjet and EPOS.

In Table 7.1 and Table 7.2, the correction factors are derived according to the method introduced above, using different $\sigma_{Smearing}$ from the two generators. Note that the final correction factors are taken from the Hydjet slope values shown in the tables, where the difference between EPOS and Hydjet is quoted as a systematic uncertainty. Therefore, the EPOS or Hydjet slope values and their statistical uncertainties are only referring to where the $\sigma_{Smearing}$ is derived.

Table 7.1 : Summary of the A_{ch} correction factors in PbPb collisions in different centrality ranges (profile slope).

PbPb centrality	80-90%	70-80%	60-70%	50-60%	40-50%	30-40%
EPOS Slope	0.668	0.746	0.724	0.698	0.671	0.637
EPOS Error	0.000	0.000	0.000	0.000	0.000	0.000
Hydjet Slope	0.623	0.699	0.689	0.673	0.663	0.645
Hydjet Error	0.000	0.000	0.000	0.000	0.000	0.000
Uncertainty	7.2%	6.8%	5.1%	3.7%	1.1%	1.2%

Table 7.2 : Summary of the A_{ch} correlation factors in pPb and PbPb collisions in different multiplicity ranges (profile slope).

pPb (PbPb) multiplicity	90-120	120-150	150-185	185-220	220-260	260-300	300-400	400-500
EPOS Slope	0.747	0.738	0.730	0.722	0.716	0.705	0.699	0.684
EPOS Error	0.000	0.000	0.000	0.000	0.000	0.000	0.000	0.000
Hydjet Slope	0.704	0.698	0.694	0.687	0.684	0.676	0.673	0.662
Hydjet Error	0.000	0.000	0.000	0.000	0.000	0.000	0.000	0.000
Uncertainty	6.1%	5.8%	5.3%	5.1%	4.7%	4.4%	3.9%	3.2%

7.2 Results of charge-dependent elliptic and triangular flow

Figure 7.4 (left column) shows the $A_{\mathrm{ch}}^{\mathrm{true}}$ dependence of v_2 coefficients, averaged over $0.3 < p_{\mathrm{T}} < 3$ GeV, for positively and negatively charged particles in the multiplicity range $185 \leq N_{\mathrm{trk}}^{\mathrm{offline}} < 220$ of pPb and PbPb collisions at $\sqrt{s_{_{NN}}} = 5.02$ TeV. The normalized v_2 difference as a function of $A_{\mathrm{ch}}^{\mathrm{true}}$ is also shown. A trend of v_2^+ (v_2^-) decreasing (increasing) as $A_{\mathrm{ch}}^{\mathrm{true}}$ increases is observed for both pPb and PbPb collisions with an approximately linear dependence. A similar linear trend of elliptic anisotropy as a function of A_{ch} has been observed in AuAu [69] and PbPb [70] systems at lower collision energies (a direct comparison to the lower-energy result [70] is reported in Appendix. B for 30–40% centrality PbPb events). The linear slope parameter, r_2^{norm}, is extracted by a χ^2 fit to a linear function, which gives values of 0.149 ± 0.008 for pPb and 0.108 ± 0.005 for PbPb, in the multiplicity range $185 \leq N_{\mathrm{trk}}^{\mathrm{offline}} < 220$. A significant nonzero value of the linear slope parameter is observed in pPb collisions, even greater than that in PbPb collisions. As the CMW effect is expected to be negligible in high-multiplicity pPb events, the observation may indicate a common physics origin unrelated to the CMW.

The $\langle p_{\mathrm{T}} \rangle$ for positively and negatively charged particles are also measured as functions of $A_{\mathrm{ch}}^{\mathrm{true}}$, in the multiplicity range $185 \leq N_{\mathrm{trk}}^{\mathrm{offline}} < 220$ of pPb and PbPb collisions at $\sqrt{s_{_{NN}}} = 5.02$ TeV, and shown in Fig. 7.4 (right column). The normalized $\langle p_{\mathrm{T}} \rangle$ difference as a function of $A_{\mathrm{ch}}^{\mathrm{true}}$ is obtained for the two systems with the slope parameters displayed in the figure. As shown, a similar linear $A_{\mathrm{ch}}^{\mathrm{true}}$ dependence of the $\langle p_{\mathrm{T}} \rangle$ value to that of v_2 is observed. As discussed earlier in Chapter 2, this behavior is qualitatively consistent with the expectation of the Local Charge Conservation (LCC) effect from resonance decays. Since v_n has a strong dependence on particle p_{T}, a correlation between the p_{T}-averaged v_n and A_{ch}, as observed in Fig. 7.4 (left),

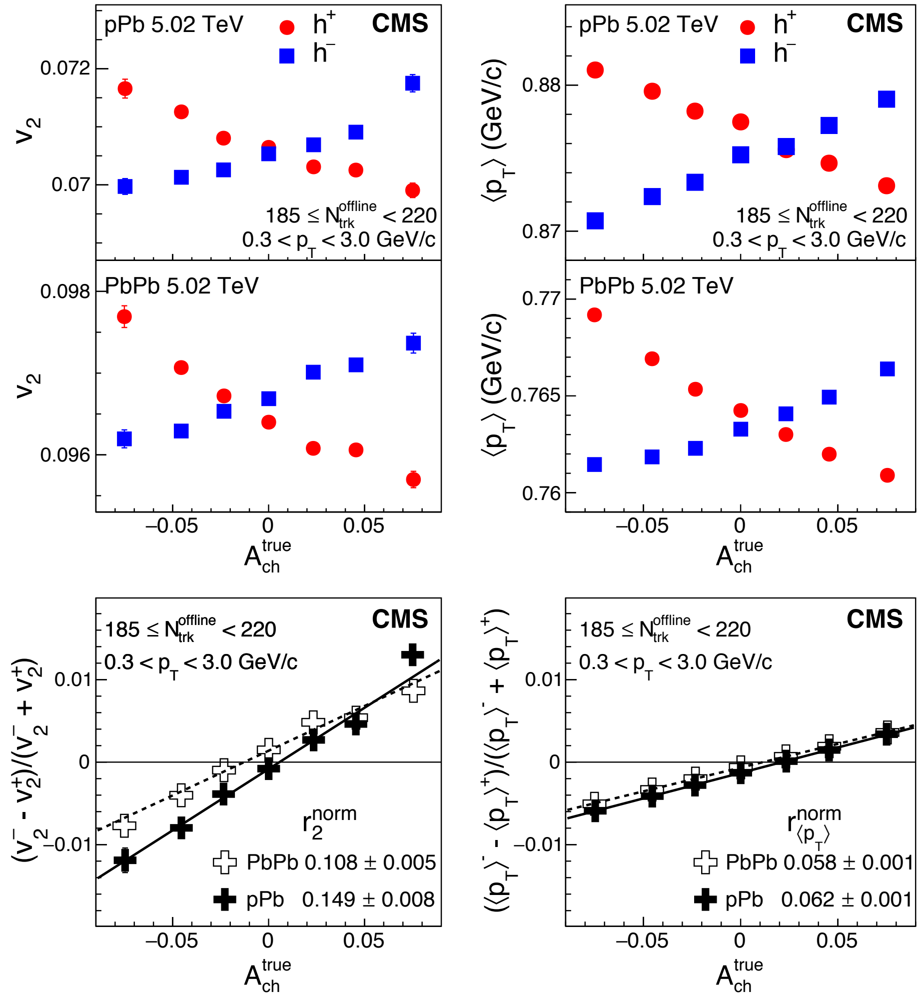

Figure 7.4 : The elliptic anisotropy v_2 (top left) and event-averaged p_T value ($\langle p_T \rangle$, top right) for positively (h^+) and negatively (h^-) charged particles, and their normalized differences (bottom row), as functions of A_{ch}^{true} for the multiplicity range $185 \leq N_{trk}^{offline} < 220$ of pPb and PbPb collisions at $\sqrt{s_{NN}} = 5.02$ TeV. Statistical uncertainties are smaller than the marker size, while systematic uncertainties are not displayed.

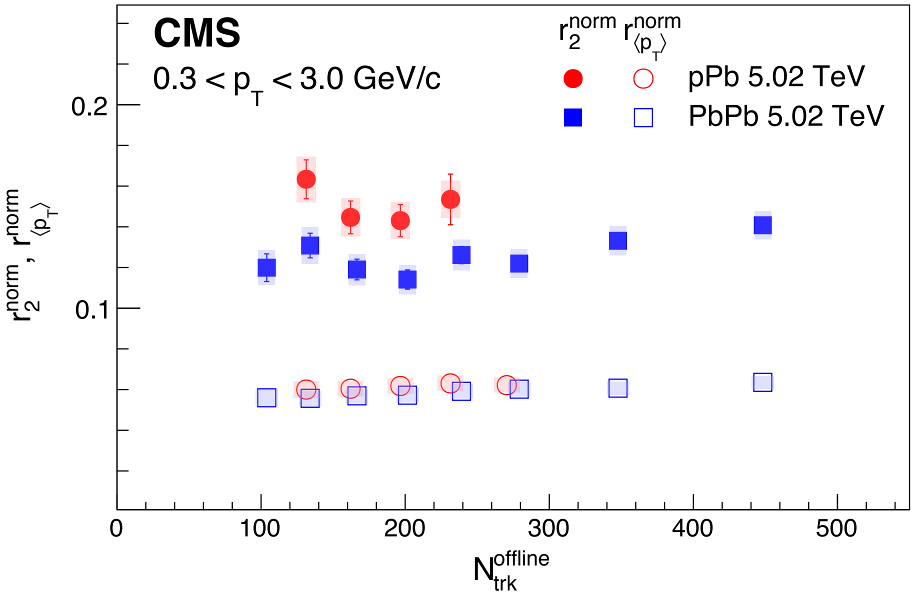

Figure 7.5 : The linear slope parameters, r^{norm}, for v_2 (filled symbols) and $\langle p_{\text{T}} \rangle$ (open symbols) as functions of event multiplicity in pPb and PbPb collisions at $\sqrt{s_{NN}} =$ 5.02 TeV. The two highest multiplicity ranges of PbPb data are selected based on the centrality, while the others are obtained by selecting on $N_{\text{trk}}^{\text{offline}}$. Statistical and systematic uncertainties are indicated by the error bars and shaded regions, respectively.

can be also induced by the LCC mechanism.

The extracted normalized slope parameters for v_2 and $\langle p_{\text{T}} \rangle$ as functions of event multiplicity in pPb and PbPb collisions are shown in Fig. 7.5. The two highest multiplicity ranges of PbPb data are selected based on the centrality class 30–40% and 40–50%, plotted at their average $N_{\text{trk}}^{\text{offline}}$ values, while the other data points are obtained from selecting on $N_{\text{trk}}^{\text{offline}}$ in order to compare directly with pPb data. The r^{norm} values for both v_2 and $\langle p_{\text{T}} \rangle$ are found to have a weak dependence on the event multiplicity for both pPb and PbPb collisions, with values for $\langle p_{\text{T}} \rangle$ approximately half of those for v_2. In the overlapping multiplicity range, normalized slope parameters are observed to be larger in pPb than PbPb collisions, which again is not expected in the CMW but may indicate a collision system dependence of the LCC or other physics mechanism. The measured values of normalized slope parameters, as well as values of absolute slope parameters, are reported in Tables of Appendix. B.

The charge asymmetry dependence of the v_3 coefficient for positively and negatively charged particles is also studied in PbPb collisions at $\sqrt{s_{_{NN}}} = 5.02$ TeV, as shown in Fig. 7.6 (top) for the 30–40% centrality class. As found for the v_2 values, the v_3^+ (v_3^-) values also decrease (increase) as $A_{\rm ch}^{\rm true}$ increases. No v_3 results for pPb collisions are reported because of limited statistical precision. The normalized v_3 difference, $(v_3^- - v_3^+)/(v_3^- + v_3^+)$, is derived as a function of $A_{\rm ch}^{\rm true}$ in PbPb collisions and compared with that for v_2 in Fig. 7.6 (bottom). The normalized slope parameter of v_3, $r_3^{\rm norm}$, agrees well with $r_2^{\rm norm}$ within statistical uncertainties. Charge-dependent higher harmonic $v_{\rm n}$ coefficients were measured in PbPb collisions at 2.76 TeV [64] and their magnitude was found to be smaller than that of the second order coefficient. We show in this thesis that, once normalized, no difference is observed for the $A_{\rm ch}^{\rm true}$ dependence between the charge-dependent v_2 and v_3.

The $r_2^{\rm norm}$ and $r_3^{\rm norm}$ values of PbPb collisions at $\sqrt{s_{_{NN}}} = 5.02$ TeV, as functions of centrality in the range 30–90%, are shown in Fig. 7.7. As found for $r_2^{\rm norm}$, a moderate centrality dependence of $r_3^{\rm norm}$ is observed. Over the centrality range studied in this analysis, the $r_2^{\rm norm}$ and $r_3^{\rm norm}$ slope parameters are consistent with each other within uncertainties. The CMW effect is expected with respect to the reaction plane, which is approximated by the second-order event plane in AA collisions, but highly suppressed with respect to the third-order event plane [55]. The similar values of the $r_2^{\rm norm}$ and $r_3^{\rm norm}$ observed in the data indicate an underlying physics mechanism that is not related to the CMW effect. This observation of the harmonic order independence, on the other hand, can be qualitatively explained by the LCC effect [71].

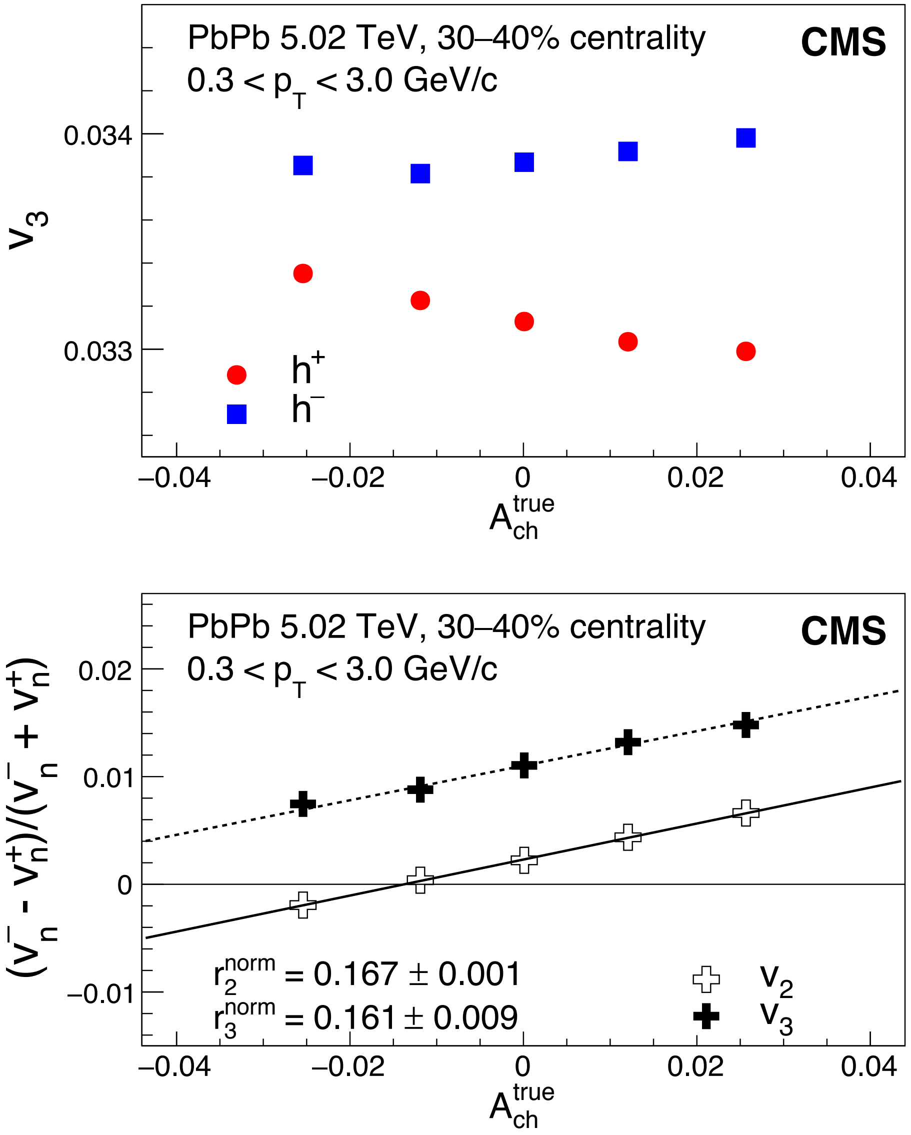

Figure 7.6 : The v_3 coefficient for positively and negatively charged particles (top) and the normalized difference in v_n, $(v_n^- - v_n^+)/(v_n^- + v_n^+)$ (bottom), for $n = 2$ and 3, as functions of true event charge asymmetry for the 30–40% centrality class in PbPb collisions at $\sqrt{s_{NN}} = 5.02$ TeV.

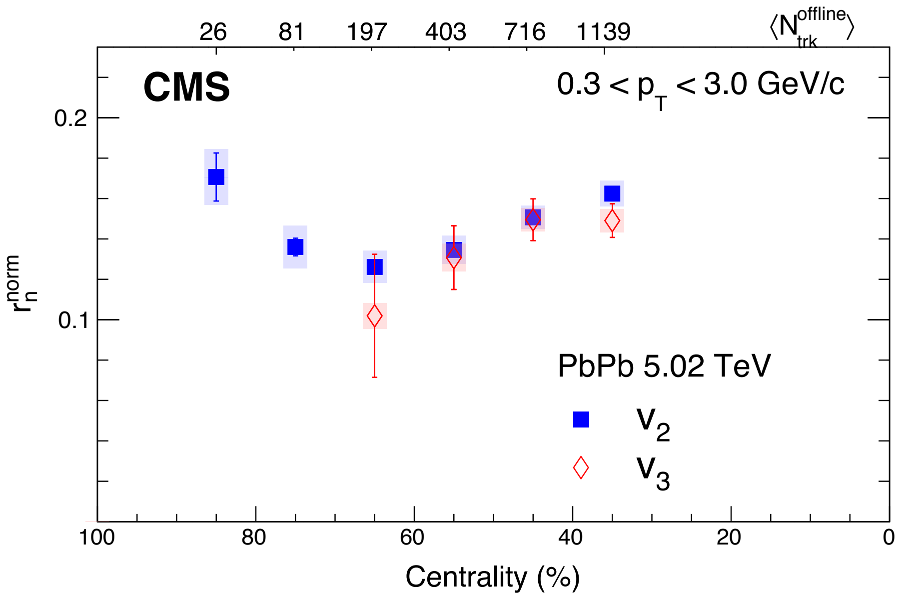

Figure 7.7 : The linear slope parameters, r_2^{norm} and r_3^{norm} as functions of the centrality class in PbPb collisions. Average $N_{\text{trk}}^{\text{offline}}$ values for each centrality class are indicated on the top axis. Statistical and systematic uncertainties are indicated by the error bars and shaded regions, respectively.

Note that the results reported here and elsewhere [69,70] used the same population of particles to measure both v_n and $A_{\text{ch}}^{\text{true}}$. However, the slope parameters are found to be reduced by about a factor of three, if the $A_{\text{ch}}^{\text{true}}$ and v_n values are determined by two distinct groups of randomly selected particles. This suggests that the observed correlations are not of a collective nature, which is qualitatively suggestive of a local effect.

7.3 Summary

The charge-dependent Fourier coefficients of the azimuthal anisotropy have been measured in pPb and PbPb collisions at $\sqrt{s_{_{NN}}} = 5.02$ TeV as functions of the charge asymmetry of the produced hadrons. The normalized differences in the v_2 coefficient between positively and negatively charged particles in pPb and PbPb, and that in the v_3 coefficient in PbPb collisions, are found to depend linearly on the charge asymmetry. The normalized slope parameters of the v_2 coefficient versus charge asymmetry in pPb collisions are found to be significant and similar to those in PbPb collisions over a wide range of charged particle multiplicities. The normalized slope parameters of the v_2 and v_3 coefficients in PbPb collisions show similar magnitudes for various centrality classes. Significant charged asymmetry dependence is also observed for the event-averaged transverse momenta of positively and negatively charged particles in both pPb and PbPb collisions. At the reported LHC energy at 5.02 TeV and within the CMS acceptance for particles between 0.3 to 3.0 GeV, none of these observations are expected from the chiral magnetic wave as the dominant physics mechanism, but they are qualitatively consistent with predictions based on local charge conservation. New measurements presented here on the charge-dependent azimuthal anisotropies in pPb and PbPb collisions pose challenges to the chiral magnetic wave as their origin.

Chapter 8

Conclusion and outlook

Conclusion The idea of using the charge-dependent correlators and charge-dependent Fourier coefficients in the high-multiplicity pPb collisions, has been a breakthrough for the longstanding problem of the chiral magnetic effect (CME) and chiral magnetic wave (CMW). These measurements have been a first experimental evidence to unambiguously uncover the presence of non-negligible background correlations in the data, which are not related to the CME and CMW. Because of the smaller magnitude of the magnetic field in very high-multiplicity pPb collisions, and its decorrelation relative to the event plane angle, the charge-dependent signal from the CME and CMW are expected to be much smaller in pPb than in the PbPb collisions. The observation of a similar charge-dependent signal in both collision systems, strongly suggests a common underlying physics mechanism without a magnetic field effect.

Based on the conventional method of measuring the charge separation signal via a charge-dependent correlator with respect to the second-order event plane, a similar but new correlator with respect to the third-order event plane opens up a new opportunity of studying the details of the background mechanism. The similar behavior between the second- and third-order correlators, together with the precise measurements of the elliptic and triangular flow (v_2 and v_3), further constrains the underlying physics mechanism to be an interplay between short-range correlations and anisotropy flow that developed from the QCD medium.

Taking advantage of the initial-state fluctuations, the event shape engineering can effectively select events with very different initial collision geometry, thus leading to a different v_2 of the final-state particles, and to explore its dependence on the charge-dependent correlators with respect to the same event plane. This dependence has been found to be strictly linear in both pPb and PbPb collisions for all measured charged-particle multiplicities, indicating the nature of its flow-driven background of the charge-dependent correlator. To remove this obvious linear dependence, a linear fit has been performed, where the intercept values are the v_2-independent components of the correlator. This component can be interpreted as a value that is directly proportional to the signal of the CME, which has been found to be very small for both pPb and PbPb collisions at LHC energies. At a confidence level of 95%, the upper limit of the possible CME fraction with respect to the charge-dependent correlator, has been found to be 13% and 7% for pPb and PbPb collisions, while the dominant uncertainty is no longer statistical but systematic. Therefore, more experimental data would not improve the significance of these results.

Outlook Even though the upper limit on the CME has been established, the real question still remains whether the CME can be discovered. Therefore, a unique and dedicated program of searching the CME signal has been scheduled at Relativistic Heavy-Ion Collider (RHIC) in 2018, where definitive answer is expected [121]. The isobaric nuclei, both with 96 nucleons but 44 protons for Ru and 40 for Zr, has been proposed to disentangle the CME signal from flow-driven background. Because of the similar shape of the nuclei and the same number of nucleons, the flow-driven background is expected to be within 2% difference between the two colliding systems. However, due to the initial charge difference that carried by the protons, the initial magnetic field is expected to be different by 10% and therefore, a 15-20% difference in the CME observable. Based on the current estimate of the total number of events, an observation of the CME signal with significance of five standard deviations is expected if the background to signal ratio is less than 3/2.

It is noteworthy to point out that the charge-dependent correlator with respect to the third-order event plane, first proposed and measured from the work of this thesis, should be precisely measured in the Ru + Ru and Zr + Zr collisions together with the elliptic and triangular flow using a large pseudorapidity separation (at least 2–3 unit) between the particle of interests and the event planes. The ratios that are shown in Fig. 6.12 and Fig. 6.13 should be carefully examined, and it will be consistent with the presence of a CME if the κ_2 is larger than the κ_3 in both sources, and the Ru + Ru system has a larger difference for this ratio.

In order to support the data that is magnetic field driven, a complementary study of directly measuring the effects of the magnetic field is encouraged, and more importantly, their differences between the two collision systems. For example, the charge-dependent directed flow (known as v_1) can be a unique measurement of the magnetic field effect. Arising from the contribution of two competing forces, Faraday and Hall effects induced by the time-dependent magnetic field, the positively- and negatively charged particles would be deflected to opposite direction if these two effects are not exactly canceled, resulting in a splitting in the charge-dependent v_1 [44]. From the published results in AuAu collisions at $\sqrt{s_{NN}} = 200$ GeV, the observation of the charge-dependent v_1 of proton and its weak dependence from the charged-pion, might be related to the baryon stopping [122]. However, these results still cannot rule out the possibility of the magnetic field induced effects, based on the precision of the data. In terms of the new isobaric collision data, with a statistics of more than 1 billion events and detector upgrades, the relative difference of the charged-dependent

v_1 between the two isobaric systems can be studied. In order to disentangle the magnetic field effects from others, a relative difference in v_1 can be measured (i.e., using proton) as a function of rapidity,

$$r_1 = 2\frac{\left(v_1^+ - v_1^-\right)_{\mathrm{Ru+Ru}} - \left(v_1^+ - v_1^-\right)_{\mathrm{Zr+Zr}}}{\left(v_1^+ - v_1^-\right)_{\mathrm{Zr+Zr}} + \left(v_1^+ - v_1^-\right)_{\mathrm{Zr+Zr}}}. \tag{8.1}$$

In a naive picture, since the difference in terms of the magnitude of the magnetic field between the two isobaric systems is 10%, the observable r_1 is expected to be 10% assuming other effects that are not related to the magnetic field cancel. Based on values and their uncertainties from Ref. [123], the measurements of Ru + Ru and Zr + Zr with the projected statistics might be able to have the sensitivity to measure a nonzero r_1 with statistical significance, if the magnetic field effect is present. Overall, this measurement will be an essential study to the search for the CME. Finally, the outlook of this thesis, the isobaric program at RHIC that is to search for the CME, will be a great opportunity of discovering this exotic phenomenon in relativistic heavy ion collisions.

Appendix A

Supporting material for the search for CME in pPb and PbPb collisions

A.1 General relation of v_n harmonics, two- and three-particle azimuthal correlations

In Chapter 2, Eq. (6.2) can be derived in a way similar as Eq. (2.6), with details which can be found in Ref. [68]. Here, a general derivation of Eq. (6.2) for all higher-order-harmonic correlators is given.

Similar to Eq. (40) in Ref. [68], the general relation between the nth order anisotropy harmonic v_n and the three-particle correlator with respect to the nth order event plane can be derived starting from,

$$\begin{aligned}\gamma_{1,n-1;n} &\equiv \langle\cos(\phi_\alpha + (n-1)\phi_\beta - n\Psi_\mathrm{n})\rangle \\ &= \frac{\int \rho_2 \cos\left(\phi_\alpha + (n-1)\phi_\beta - n\Psi_n\right) d\phi_\alpha\, d\phi_\beta\, dx_\alpha\, dx_\beta}{\int \rho_2 d\phi_\alpha\, d\phi_\beta\, dx_\alpha\, dx_\beta} \\ &= \frac{\int \rho_2 \cos\left(\phi_\alpha - \phi_\beta + n(\phi_\beta - \Psi_n)\right) d\phi_\alpha\, d\phi_\beta\, dx_\alpha\, dx_\beta}{\int \rho_2 d\phi_\alpha\, d\phi_\beta\, dx_\alpha\, dx_\beta},\end{aligned} \tag{A.1}$$

where x denotes (p_T, η) and $dx = p_\mathrm{T}\, dp_\mathrm{T}\, d\eta$. ρ_2 is the two-particle pair density distribution, which can be expressed in terms of the single-particle density distribution and its underlying two-particle correlation function (see Section 2 in Ref. [68]),

$$\rho_2 = \rho(\phi_\alpha, x_\alpha)\rho(\phi_\beta, x_\beta)\left[1 + C(\phi_\alpha, \phi_\beta, x_\alpha, x_\beta)\right]. \tag{A.2}$$

In presence of collective anisotropic flow, the single-particle azimuthal distribution can be expressed in terms of a Fourier series with respect to the event plane of the corresponding order,

$$\rho(\phi, x) = \frac{\rho_0(x)}{2\pi}\left[1 + \sum_{n=1}^{\infty} n v_{\mathrm{n}}(x) \cos n(\phi - \Psi_n)\right], \tag{A.3}$$

where $\rho_0(x)$ depends on p_{T} and η only.

The two-particle correlation function C describes intrinsic correlations that are insensitive to the event plane Ψ_n, but only involve azimuthal angle difference $\Delta\phi = \phi_\alpha - \phi_\beta$. It can be also expanded in Fourier series [68],

$$C(\Delta\phi, x_\alpha, x_\beta) = \sum_{n=1}^{\infty} a_n(x_\alpha, x_\beta) \cos(n\Delta\phi), \tag{A.4}$$

where $a_n(x_\alpha, x_\beta)$ is the two-particle Fourier coefficient. By definition, $a_1(x_\alpha, x_\beta)$ is equal to the two-particle correlator $\delta(x_\alpha, x_\beta)$, introduced in Section 1, as a function of x_α and x_β (i.e., p_{T} and η of both particles).

Therefore, we substitute Eqs. (A.4) and (A.2) into (A.1) and obtain,

$$\begin{aligned}\gamma_{1,n-1;n} = \frac{1}{2N^2} \int & \rho_0(x_\alpha)\rho_0(x_\beta) a_1(x_\alpha, x_\beta) \\ & [v_n(x_\alpha) + v_n(x_\beta)]\, dx_\alpha\, dx_\beta \\ = \frac{1}{2N^2} \int & \rho_0(x_\alpha)\rho_0(x_\beta)\delta(x_\alpha, x_\beta) \\ & [v_n(x_\alpha) + v_n(x_\beta)]\, dx_\alpha\, dx_\beta\end{aligned} \tag{A.5}$$

where $N = \int \rho_0(x) dx$. This is the general equation explaining why a nonzero two-particle correlation $\delta(x_\alpha, x_\beta)$ plus an anisotropic flow of nth order $v_n(x)$ contribute to the three-particle correlator, $\gamma_{1,n-1;n}$.

Therefore, this general form of $\gamma_{1,n-1;n}$ can be applied to any order n and decomposed into the two-particle correlator δ and the nth order harmonic v_n, where $n = 2$ and 3 are studied in detail in Section 6.3.1.

A.2 Supporting results of the event shape engineering method

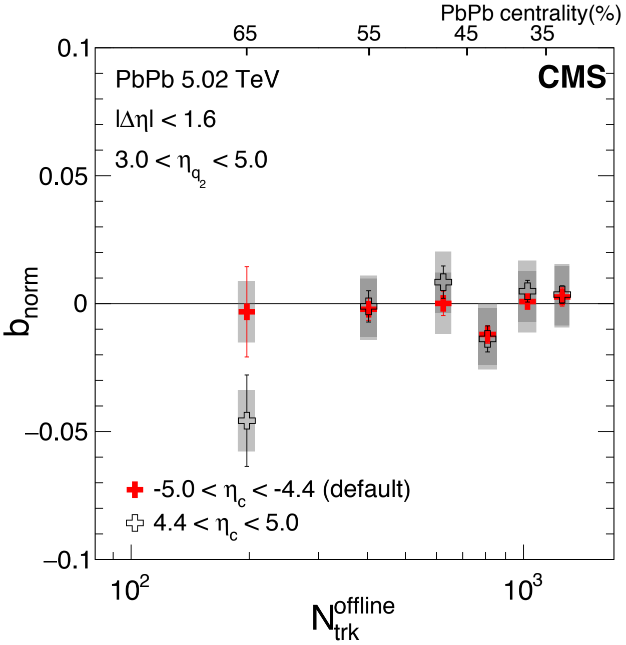

Figure A.1 : The intercepts b_{norm} of v_2-independent γ_{112} correlator component using particle c from HF+ and HF− data, averaged over $|\Delta\eta| < 1.6$, are shown as a function of $N_{\mathrm{trk}}^{\mathrm{offline}}$ in PbPb collisions at $\sqrt{s_{NN}} = 5.02$ TeV. Statistical and systematic uncertainties are indicated by the error bars and shaded regions, respectively.

As stated in Section 6.1.2, the Q_2 vector is calculated using one side of the HF detector within the η range of 3 to 5 units. The default result in Section 6.3.3 presents the $\Delta\gamma_{112}$ as a function of v_2, where the particle c in the γ_{112} correlator corresponds to the η range -5.0 to -4.4. However, the results are found to be independent of where the particle c is reconstructed, as it is shown in Fig. A.1.

In Figs. A.2 and A.3, the denominators of Eq. (6.4), $v_{2,c}$, for different Q_2 classes with respect to HF+ and HF− in PbPb collisions at $\sqrt{s_{NN}} = 5.02$ TeV, and the Pb-going side of the HF in pPb collisions at 8.16 TeV, are shown as a function of v_2 in the tracker region. Here $v_{2,c}$ is a measure of elliptic anisotropy of the transverse energy

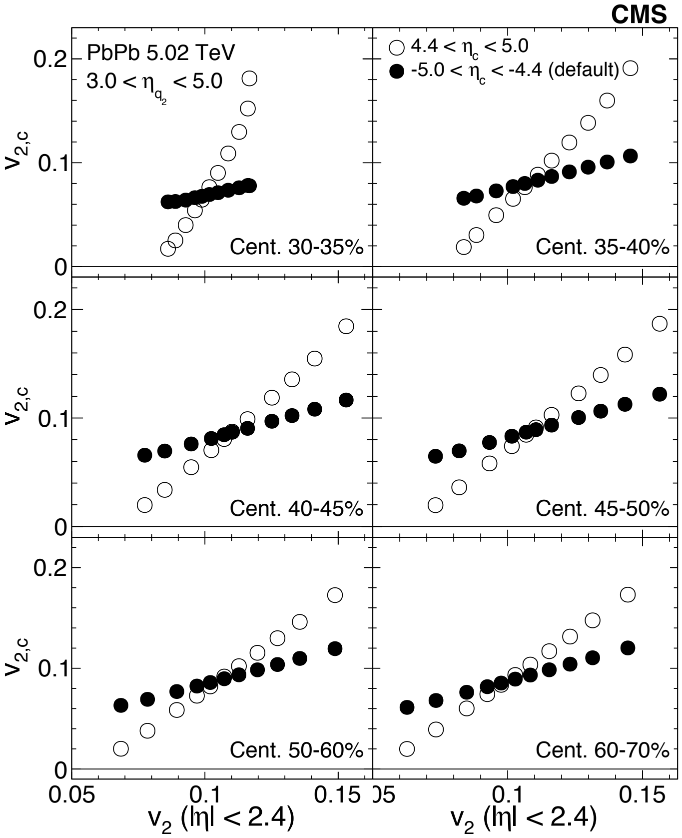

Figure A.2 : The $v_{2,c}$ using particle c from HF+ and HF− data are shown as a function of v_2 in the tracker region ($|\eta| < 2.4$) in PbPb collisions at $\sqrt{s_{NN}} = 5.02$ TeV.

registered in the HF detectors without being corrected to the particle-level elliptic flow. It serves as the resolution correction factor when deriving the three-particle correlators or the v_2 values in the tracker region using the scalar-product method.

In Fig. A.4, the average $N_{\text{trk}}^{\text{offline}}$ is shown as a function of v_2 in different multiplicity and centrality ranges in pPb (upper) and PbPb collisions (lower), respectively. The average $N_{\text{trk}}^{\text{offline}}$ is found to be weakly dependent on v_2, but with a slight decreasing trend as v_2 increases. Similar to Fig. 6.16, the effect at low multiplicities is stronger than that at high multiplicities. Overall, this effect is negligible for the results shown

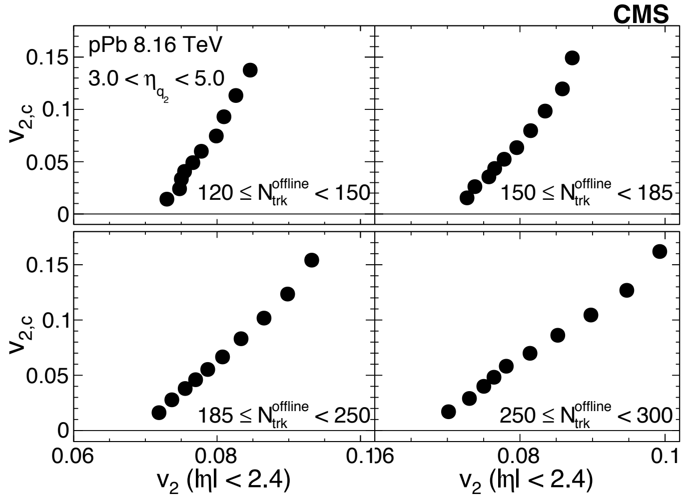

Figure A.3 : The $v_{2,c}$ using particle c from the Pb-going side of the HF ($4.4 < \eta < 5.0$) data are shown as a function of v_2 in the tracker region ($|\eta| < 2.4$) in pPb collisions at $\sqrt{s_{_{NN}}} = 8.16$ TeV.

in Section 6.3.3.

A.3 Three- and two-particle correlator as functions of differential variables in different multiplicity and centrality classes

The figures in Appendix A.3 show the γ_{112}, γ_{123}, and the δ correlators as a function of $|\Delta\eta|$, $|\Delta p_{\mathrm{T}}|$, and $\overline{p}_{\mathrm{T}}$ in pPb collisions at $\sqrt{s_{_{NN}}} = 8.16$ TeV and PbPb collisions at 5.02 TeV. In pPb and PbPb collisions, the results are shown for multiplicity ranges $N_{\mathrm{trk}}^{\mathrm{offline}}$ = [120,150), [150,185), [185,250), and [250,300) in Figs. A.5 to A.7. In PbPb collisions, the results are also shown for five centrality classes from 30–80% in Figs. A.8 to A.10.

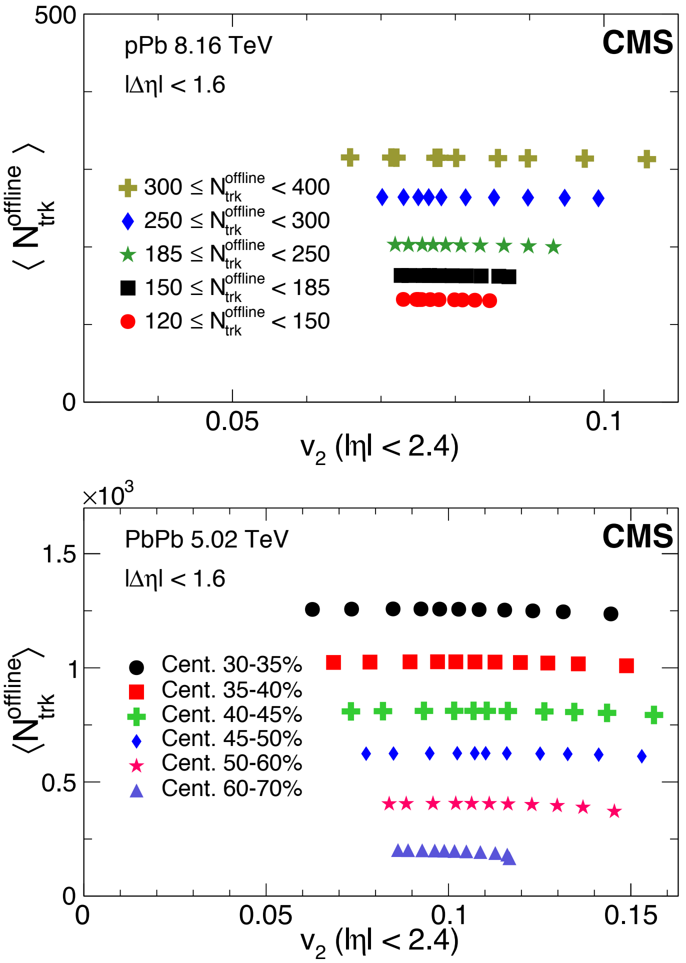

Figure A.4 : The average multiplicity $N_{\mathrm{trk}}^{\mathrm{offline}}$ as a function of v_2 evaluated in each q_2 class, for different multiplicity ranges in pPb collisions at $\sqrt{s_{NN}} = 8.16$ TeV (upper), and for different centrality classes in PbPb collisions at 5.02 TeV (lower). Statistical uncertainties are invisible on the current scale.

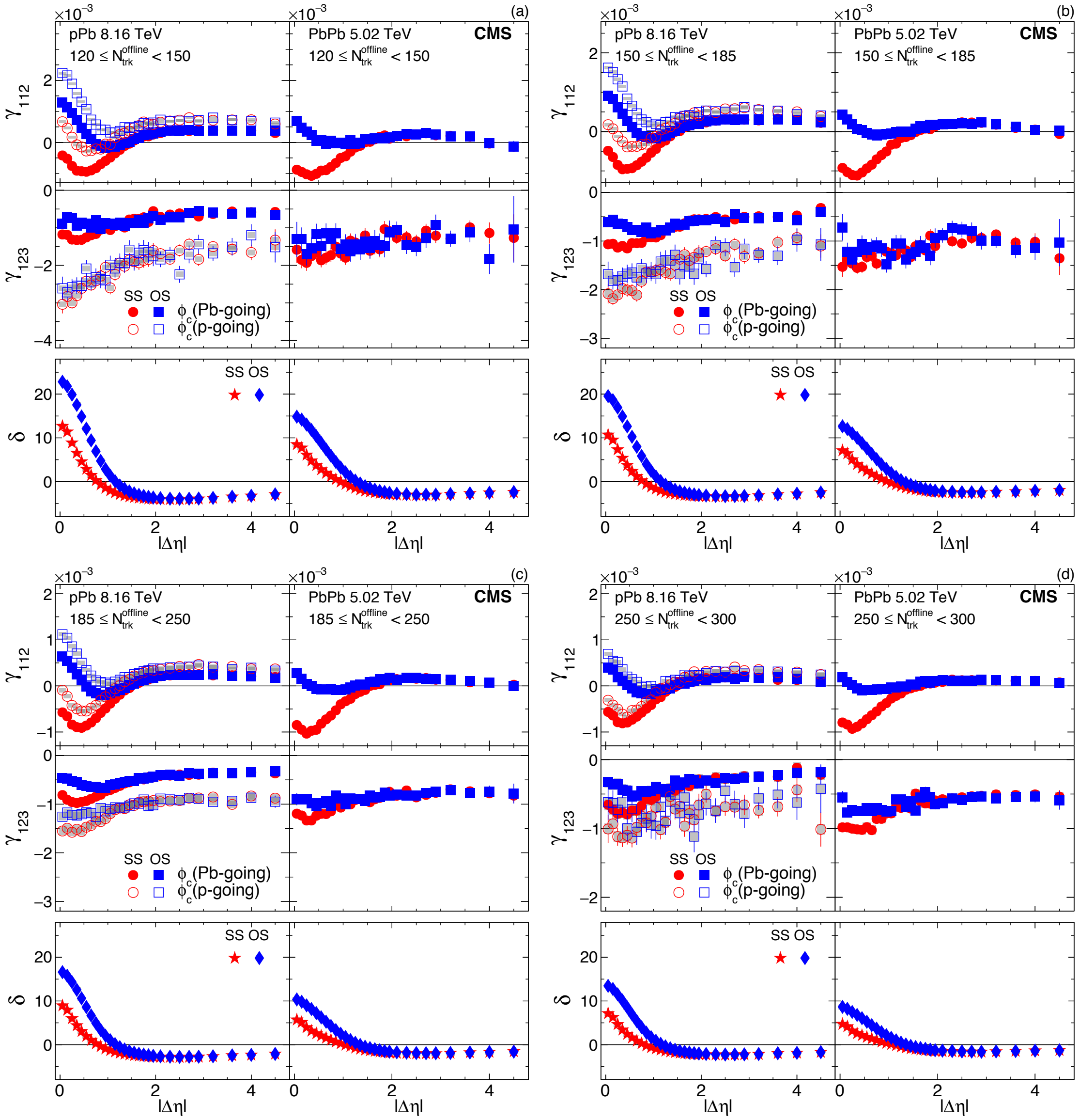

Figure A.5 : The SS and OS three-particle correlators, γ_{112} (upper) and γ_{123} (middle), and two-particle correlator, δ (lower), as a function of $|\Delta\eta|$ for four multiplicity ranges in pPb collisions at $\sqrt{s_{NN}}$ = 8.16 TeV (left) and PbPb collisions at 5.02 TeV (right). The pPb results obtained with particle c in Pb-going (solid markers) and p-going (open markers) sides are shown separately. The SS and OS two-particle correlators are denoted by different markers for both pPb and PbPb collisions. Statistical and systematic uncertainties are indicated by the error bars and shaded regions, respectively.

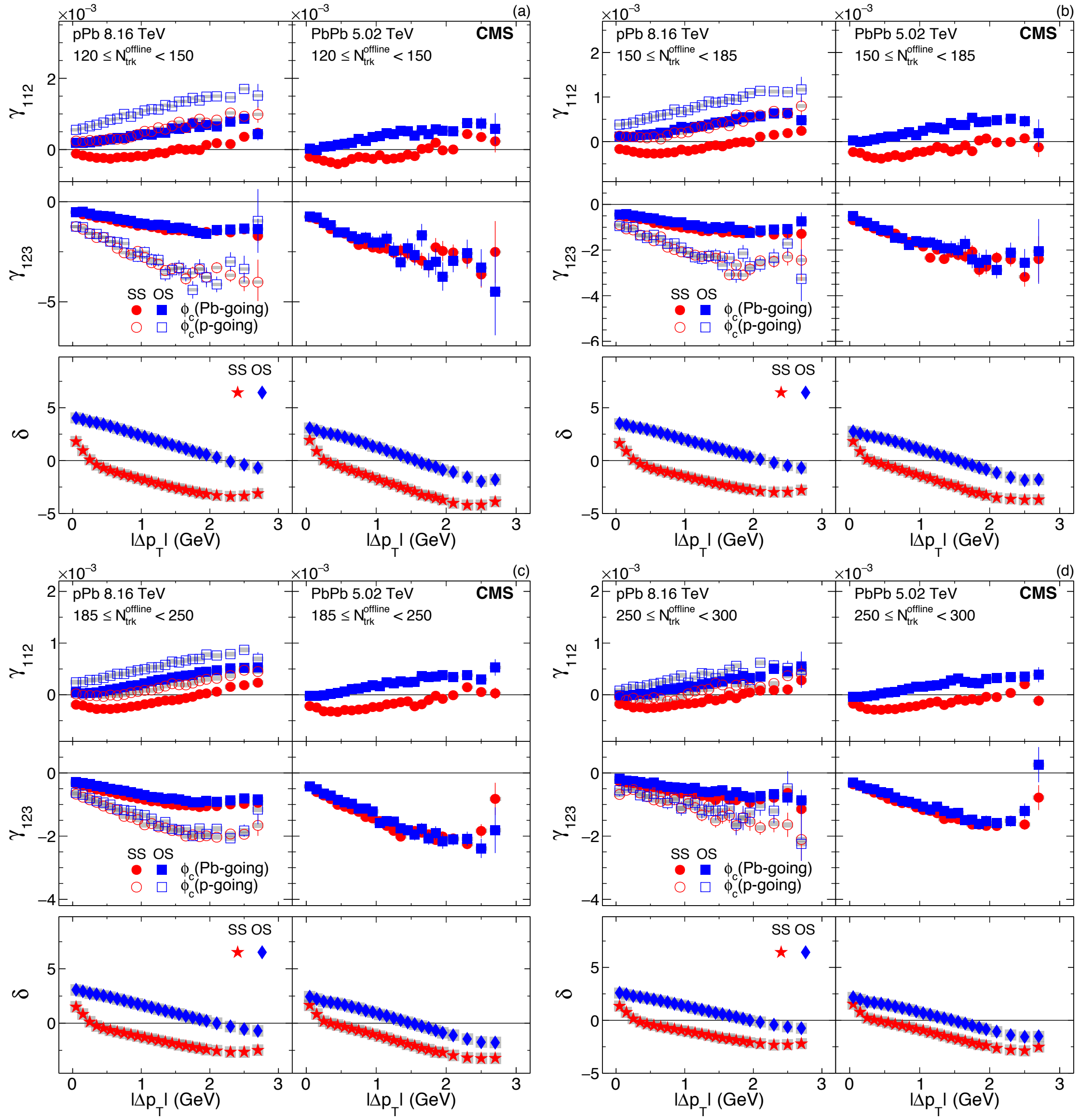

Figure A.6 : The SS and OS three-particle correlators, γ_{112} (upper) and γ_{123} (middle), and two-particle correlator, δ (lower), as a function of $|\Delta p_{\mathrm{T}}|$ for four multiplicity ranges in pPb collisions at $\sqrt{s_{NN}} = 8.16$ TeV (left) and PbPb collisions at 5.02 TeV (right) collisions. The pPb results obtained with particle c in Pb-going (solid markers) and p-going (open markers) sides are shown separately. The SS and OS two-particle correlators are denoted by different markers for both pPb and PbPb collisions. Statistical and systematic uncertainties are indicated by the error bars and shaded regions, respectively.

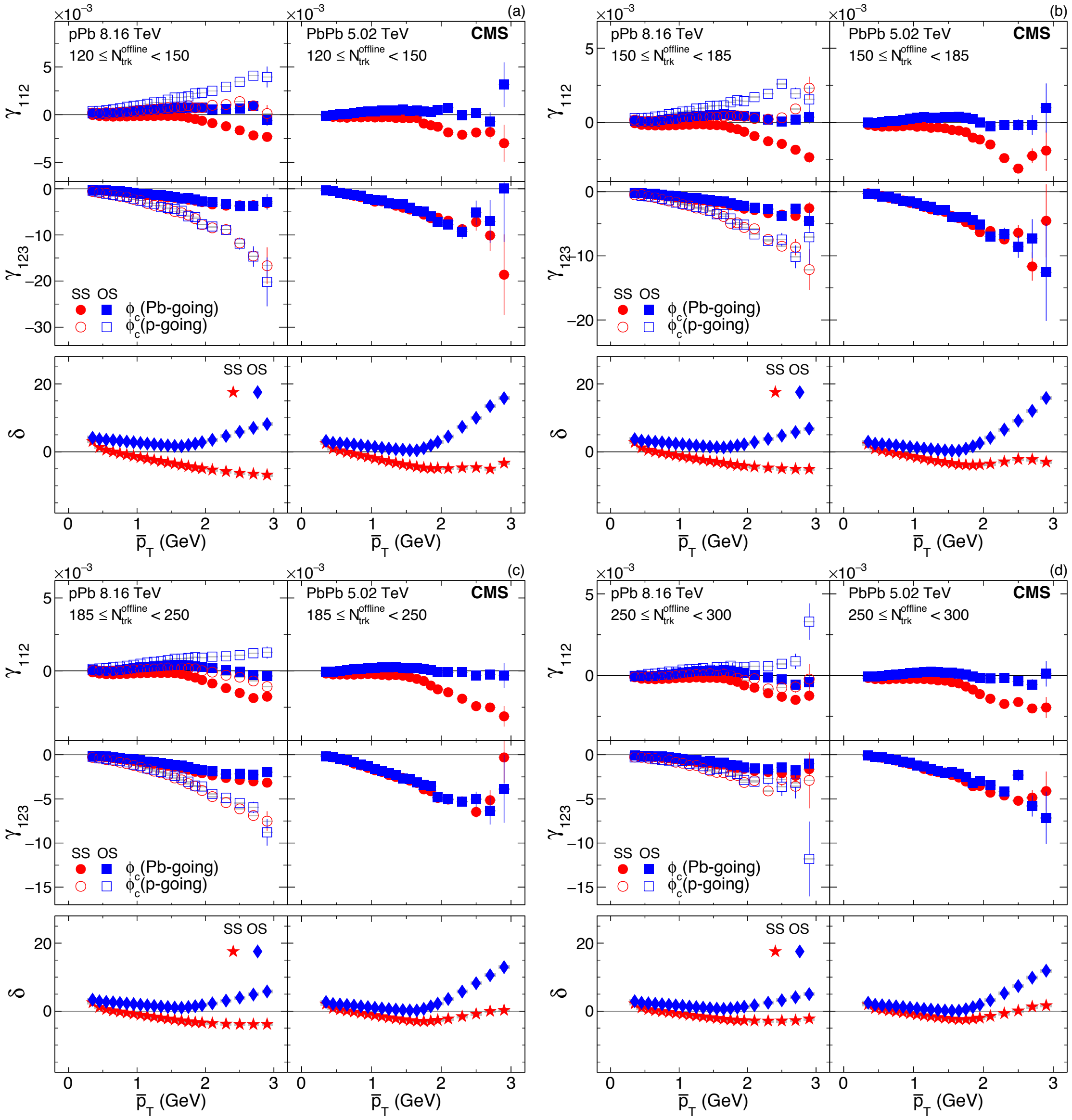

Figure A.7 : The SS and OS three-particle correlators, γ_{112} (upper) and γ_{123} (middle), and two-particle correlator, δ (lower), as a function of $\overline{p}_{\mathrm{T}}$ for four multiplicity ranges in pPb collisions at $\sqrt{s_{NN}}$ = 8.16 TeV (left) and PbPb collisions at $\sqrt{s_{NN}}$ = 5.02 TeV (right). The pPb results obtained with particle c in Pb-going (solid markers) and p-going (open markers) sides are shown separately. The SS and OS two-particle correlators are denoted by different markers for both pPb and PbPb collisions. Statistical and systematic uncertainties are indicated by the error bars and shaded regions, respectively.

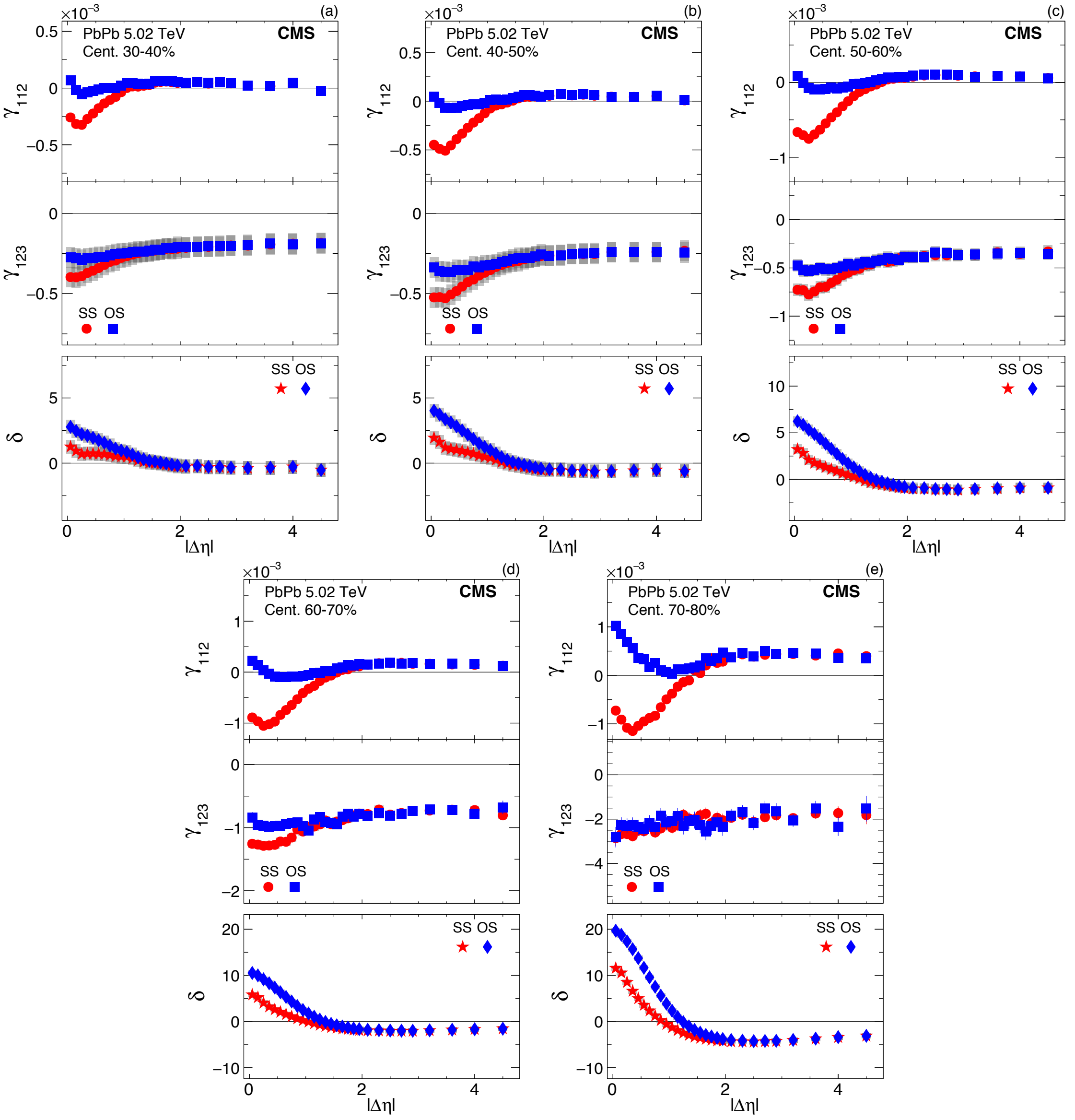

Figure A.8 : The SS and OS three-particle correlators, γ_{112} (upper) and γ_{123} (middle), and two-particle correlator, δ (lower), as a function of $|\Delta\eta|$ for five centrality classes in PbPb collisions at 5.02 TeV. The SS and OS two-particle correlators are denoted by different markers. Statistical and systematic uncertainties are indicated by the error bars and shaded regions, respectively.

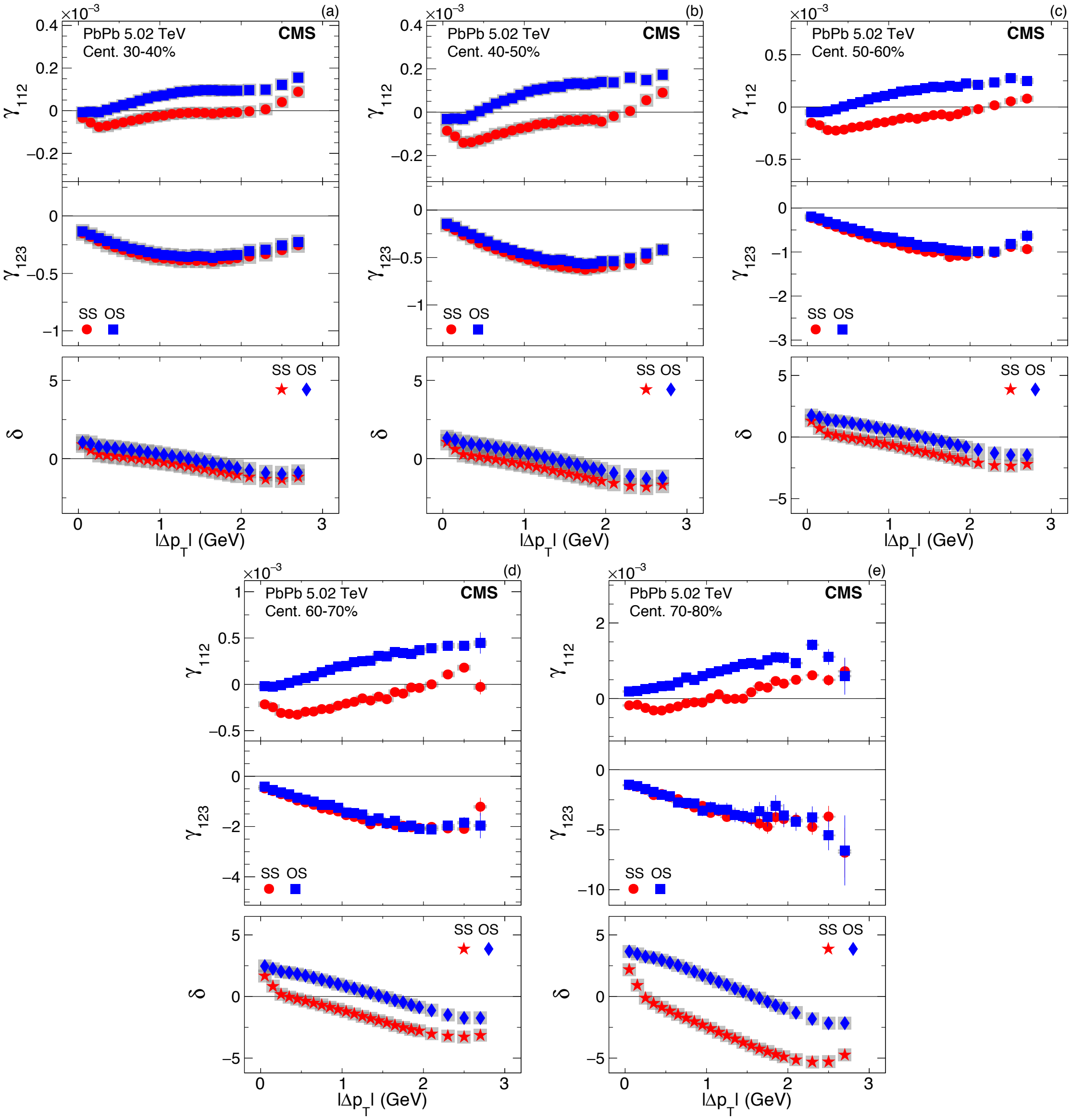

Figure A.9 : The SS and OS three-particle correlators, γ_{112} (upper) and γ_{123} (middle), and two-particle correlator, δ (lower), as a function of $|\Delta p_{\mathrm{T}}|$ for five centrality classes in PbPb collisions at $\sqrt{s_{NN}} = 5.02$ TeV. The SS and OS two-particle correlators are denoted by different markers. Statistical and systematic uncertainties are indicated by the error bars and shaded regions, respectively.

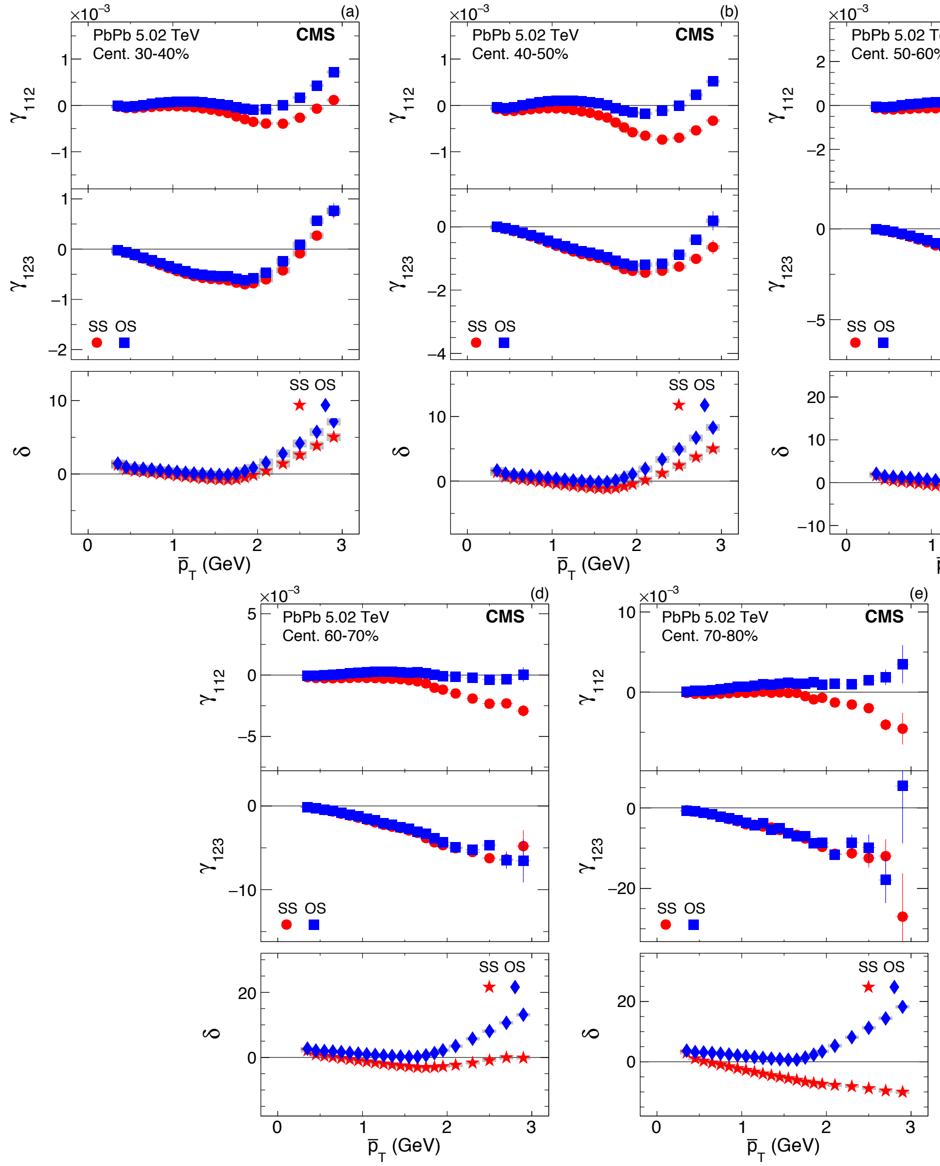

Figure A.10 : The SS and OS three-particle correlators, γ_{112} (upper) and γ_{123} (middle), and two-particle correlator, δ (lower), as a function of $\overline{p}_{\mathrm{T}}$ for five centrality classes in PbPb collisions at $\sqrt{s_{NN}} = 5.02$ TeV. The SS and OS two-particle correlators are denoted by different markers. Statistical and systematic uncertainties are indicated by the error bars and shaded regions, respectively.

Appendix B

Supporting material for the search for CMW in pPb and PbPb collisions

The normalized difference in elliptic flow v_2 between positively and negatively charged particles as a function of charge asymmetry is shown in Fig. B.1, in the centrality range 30–40% with particles within $|\eta| < 0.8$ and $0.2 \leq p_{\mathrm{T}} < 5.0$ GeV, and are compared between the ALICE [70] and the CMS experiment in PbPb collisions at $\sqrt{s_{_{NN}}} = 2.76$ TeV and 5.02 TeV, respectively.

The $A_{\mathrm{ch}}^{\mathrm{obs}}$ in centrality range 30–40% is shown in Fig. B.2, with particles selected between 0.3 to 3.0 GeV and pseudorapidity range $|\eta| < 2.4$.

From Table B.1 to B.3, the values of the slope parameter and normalized slope parameter for v_2 and $\langle p_{\mathrm{T}} \rangle$ are shown in pPb and PbPb collisions.

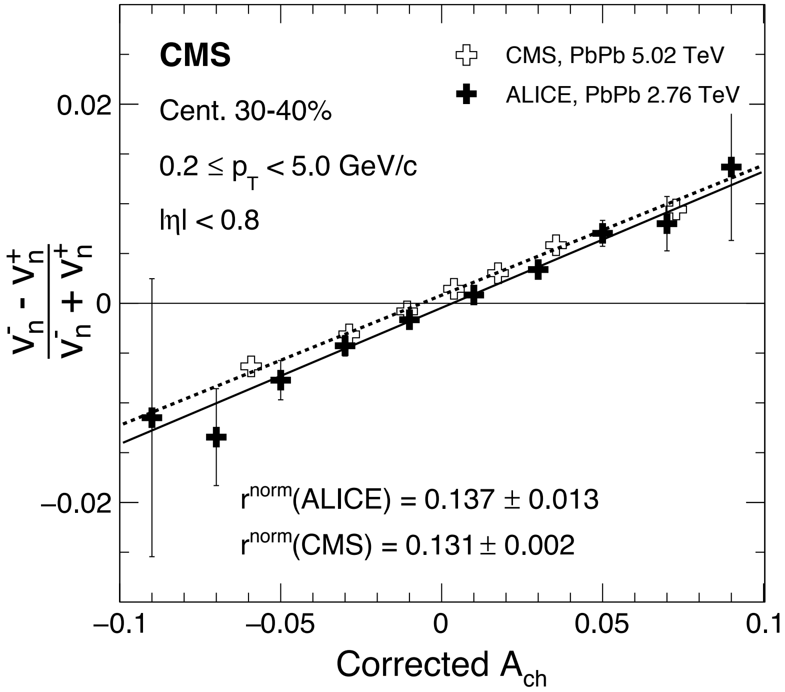

Figure B.1 : The normalized difference in elliptic flow v_2 between positive- and negative-charged particles, $(v_2^- - v_2^+)/(v_2^- + v_2^+)$, as a function of charge asymmetry is presented. The results are selected in centrality range 30–40% with particles within $|\eta| < 0.8$ and $0.2 \le p_{\mathrm{T}} < 5.0$GeV, and are compared between the ALICE [70] and the CMS experiment in PbPb collisions at $\sqrt{s_{_{NN}}}$ = 2.76TeV and 5.02 TeV, respectively. The bars represent statistical point-by-point uncertainties.

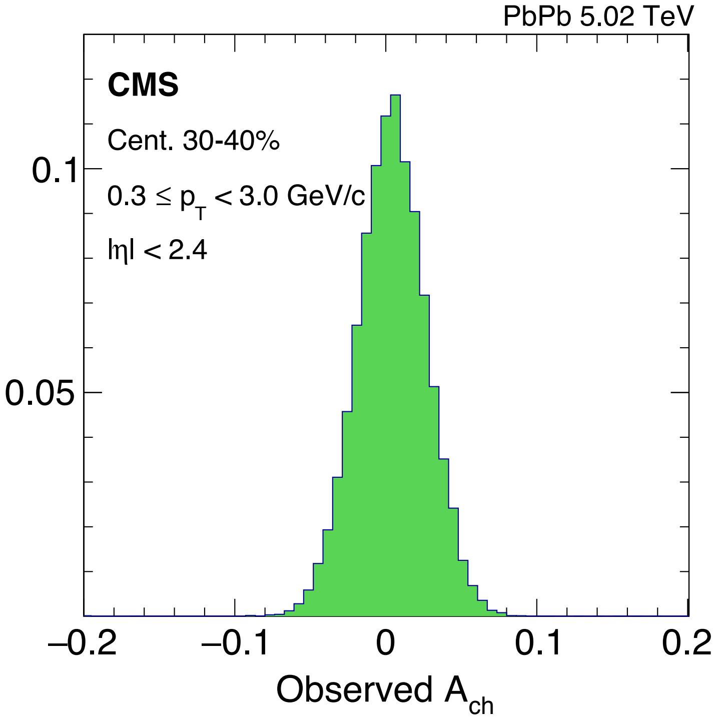

Figure B.2 : The event-by-event observed charge asymmetry, A_{ch}, is shown within the centrality range 30–40% in PbPb collisions at $\sqrt{s_{NN}} = 5.02$ TeV. The particles are selected between 0.3 to 3.0 GeV and pseudorapidity range $|\eta| < 2.4$.

Table B.1 : The table summarizes the absolute and normalized slope parameters (r) from v_2 and $\langle p_{\mathrm{T}} \rangle$ in ranges of multiplicity class, $N_{\mathrm{trk}}^{\mathrm{offline}}$, in pPb collisions at $\sqrt{s_{_{NN}}}$= 5.02 TeV. The first uncertainty associated with the central values denotes statistical errors, while the second uncertainty represents the systematic uncertainty.

$N_{\mathrm{trk}}^{\mathrm{offline}}$	$r_{\langle v_2 \rangle}$	$r_{\langle v_2 \rangle}^{\mathrm{norm}}$	$r_{\langle p_{\mathrm{T}} \rangle}$	$r_{\langle p_{\mathrm{T}} \rangle}^{\mathrm{norm}}$
$[120, 150)$	0.022±0.001±0.002	0.163±0.01±0.011	0.103±0.001±0.007	0.06±0±0.004
$[150, 185)$	0.02±0.001±0.001	0.145±0.008±0.009	0.105±0.001±0.007	0.06±0±0.004
$[185, 220)$	0.02±0.001±0.001	0.149±0.008±0.009	0.108±0.001±0.007	0.062±0.001±0.004
$[220, 260)$	0.022±0.002±0.001	0.153±0.012±0.009	0.111±0.002±0.007	0.063±0.001±0.004

Table B.2 : The table summarizes the absolute and normalized slope parameters (r) from v_2 and $\langle p_{\mathrm{T}} \rangle$ in ranges of multiplicity class, $N_{\mathrm{trk}}^{\mathrm{offline}}$, in PbPb collisions at $\sqrt{s_{_{NN}}}$= 5.02 TeV. The first uncertainty associated with the central values denotes statistical errors, while the second uncertainty represents the systematic uncertainty.

$N_{\mathrm{trk}}^{\mathrm{offline}}$	$r_{\langle v_2 \rangle}$	$r_{\langle v_2 \rangle}^{\mathrm{norm}}$	$r_{\langle p_{\mathrm{T}} \rangle}$	$r_{\langle p_{\mathrm{T}} \rangle}^{\mathrm{norm}}$
$[90, 120)$	0.02±0.001±0.001	0.12±0.007±0.009	0.084±0.001±0.006	0.056±0±0.004
$[120, 150)$	0.023±0.001±0.002	0.131±0.006±0.009	0.084±0.001±0.006	0.056±0.001±0.004
$[150, 185)$	0.022±0.001±0.001	0.119±0.005±0.008	0.087±0.001±0.006	0.057±0.001±0.004
$[185, 220)$	0.022±0.001±0.001	0.108±0.005±0.007	0.087±0.001±0.006	0.058±0.001±0.004
$[220, 260)$	0.025±0.001±0.001	0.126±0.004±0.008	0.091±0.001±0.005	0.059±0.001±0.004
$[260, 300)$	0.025±0.001±0.001	0.122±0.004±0.007	0.093±0.001±0.005	0.06±0.001±0.003
$[300, 400)$	0.028±0±0.001	0.133±0.002±0.007	0.094±0.001±0.005	0.061±0±0.003
$[400, 500)$	0.03±0±0.001	0.141±0.002±0.007	0.099±0.001±0.005	0.064±0.001±0.003

Table B.3 : The table summarizes the absolute and normalized slope parameters (r) from v_2 and v_3 in ranges of centrality class, in PbPb collisions at $\sqrt{s_{_{NN}}}$= 5.02 TeV. The first uncertainty associated with the central values denotes statistical errors, while the second uncertainty represents the systematic uncertainty.

Centrality	$r_{\langle v_2 \rangle}$	$r^{\text{norm}}_{\langle v_2 \rangle}$	$r_{\langle p_{\text{T}} \rangle}$	$r^{\text{norm}}_{\langle p_{\text{T}} \rangle}$
30–40%	0.032±0±0.001	0.162±0.001±0.006	0.01±0.0006±0.0004	0.149±0.008±0.006
40–50%	0.032±0±0.001	0.151±0.001±0.006	0.0102±0.0007±0.0004	0.15±0.01±0.006
50–60%	0.028±0±0.001	0.135±0.001±0.007	0.0083±0.001±0.0004	0.131±0.016±0.007
60–70%	0.024±0±0.002	0.126±0.002±0.008	0.0054±0.0016±0.0003	0.102±0.03±0.006
70–80%	0.022±0.001±0.002	0.136±0.004±0.011	NA	NA
80–90%	0.022±0.002±0.002	0.171±0.012±0.014	NA	NA

Appendix C

Details of data samples, triggers, and track reconstruction

C.1 High-multiplicity trigger performance

To measure the triggers efficiency a reference method was used, where a minimum bias trigger is used as reference. The efficiency is computed using the following expression:

$$\text{Trigger Efficiency} = \frac{\text{N Events Firing Desired Trigger \& MinBias Trigger}}{\text{N Events Firing MinBias Trigger}}.$$

The Fig. C.1 shows the efficiency turn-on curves for the L1 trigger component (Tower Count), HLT-only component, and the total trigger (L1 + HLT) as a function of track multiplicity (denoted as $\mathrm{N}_{\mathrm{trk}}^{\mathrm{offline}}$).

C.2 Data sample

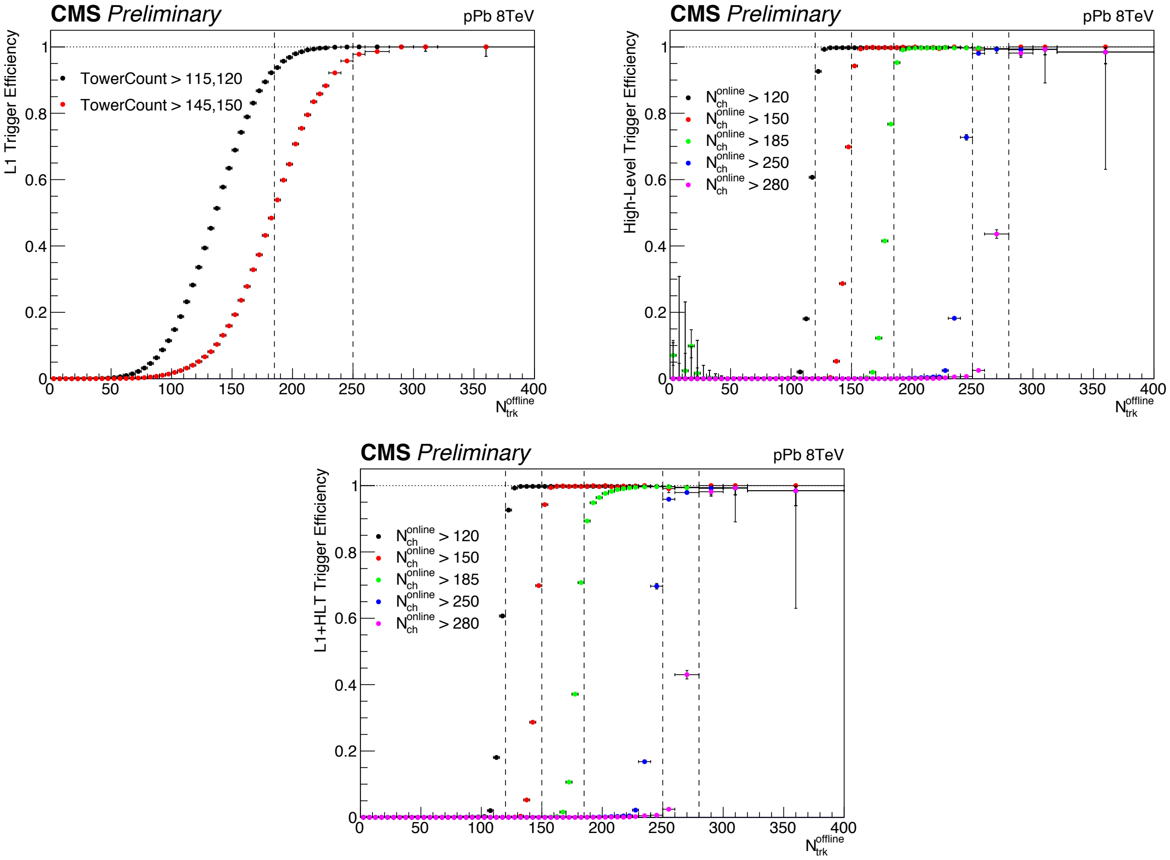

Figure C.1 : High multiplicity trigger efficiency as a function of offline selected track multiplicity. Top left: level-1 trigger. Top right: HLT-only component. Bottom: total efficiency, L1+HLT. The vertical lines indicate the online track multiplicity selection for each trigger.

Table C.1 : Detail information of the pPb and PbPb data sample used in this work, including pileup, integrated luminosity and number of events collected by the triggers.

Collision	Energy	Year	Pileup	Int. lumi	Trigger	Triggered events
pPb	5.02 TeV	2013	0.06	35 nb^{-1}	HLT_PAZeroBiasPixel_SingleTrack	31.4
					HLT_PixelTracks_Multiplicity100	19.2
					HLT_PixelTracks_Multiplicity130	18.9
					HLT_PixelTracks_Multiplicity160	17
					HLT_PixelTracks_Multiplicity190	8
pPb	8.16 TeV	2016	0.4	174 nb^{-1}	HLT_PAFullTracks_Multiplicity120	286.51
					HLT_PAFullTracks_Multiplicity150	216.14
					HLT_PAFullTracks_Multiplicity185	795.7
					HLT_PAFullTracks_Multiplicity250	64
PbPb	5.02 TeV	2015	0.001	530 $\mu\mathrm{b}^{-1}$	HLT_HIL1Centralityext30100MinimumumBiasHF1AND_v1	330

C.3 Heavy ion tracking

For the heavy ion PbPb tracking algorithm in 2015, the iterative tracking have four global iterations and one additional regional jet core iteration. In Table C.2 the seeds, parameters used in each iteration are shown as well as the tracks these iterations aim to reconstruct.

Table C.2 : Iterative tracking with four global iterations and one additional regional jet core iteration are presented with the information about seeds, and parameters used

Iteration	Target	Seeding	$p_{\mathrm{T}} >$ (GeV)	d_0	d_{z}
Initial Step	high pt prompt	Pixel track	0.9	0.1 cm	$3\ \sigma_{\mathrm{BS}}$
Detached Step	displaced prompt	Pixel triplets	0.9	0.5 cm	$4\ \sigma_{\mathrm{BS}}$
Low p_{T} Step	low pt prompt	Pixel triplets	0.4	0.02 cm	$4\ \sigma_{\mathrm{BS}}$
Pixel Pair Step	recover high pt prompt	Pixel pairs	0.9	0.005 cm	$4\ \sigma_{\mathrm{BS}}$
Jet core	regional around high pt jets	Pixel triplets	10	0.2 cm	$3\ \sigma_{\mathrm{BS}}$

Note that the new iteration that had been implemented for the 2015 PbPb data taking at $\sqrt{s_{NN}} = 5.02$ TeV was jet core, which was briefly described in Sec. 5.1.4.

C.4 Tracking performance using pp and PbPb reconstruction algorithm

There are 3 sub-subsections below, which are corresponding to using heavy-ion reconstruction algorithm, pp reconstruction algorithm, and the comparison between heavy-ion and pp reconstruction, respectively.

Tracking performance in heavy-ion reconstruction The tracking performance figures derived from heavy-ion reconstruction are shown from Fig. C.2 to Fig. C.3, in terms of tracking efficiency×acceptance, fake reconstruction rates. The multiple reconstruction rates, and nonprompt reconstruction rates are found to be small for most of cases, therefore not shown. All the quantities are presented in the centrality ranges, 0–5%, 5–10%, 30–50%, and 50–100%.

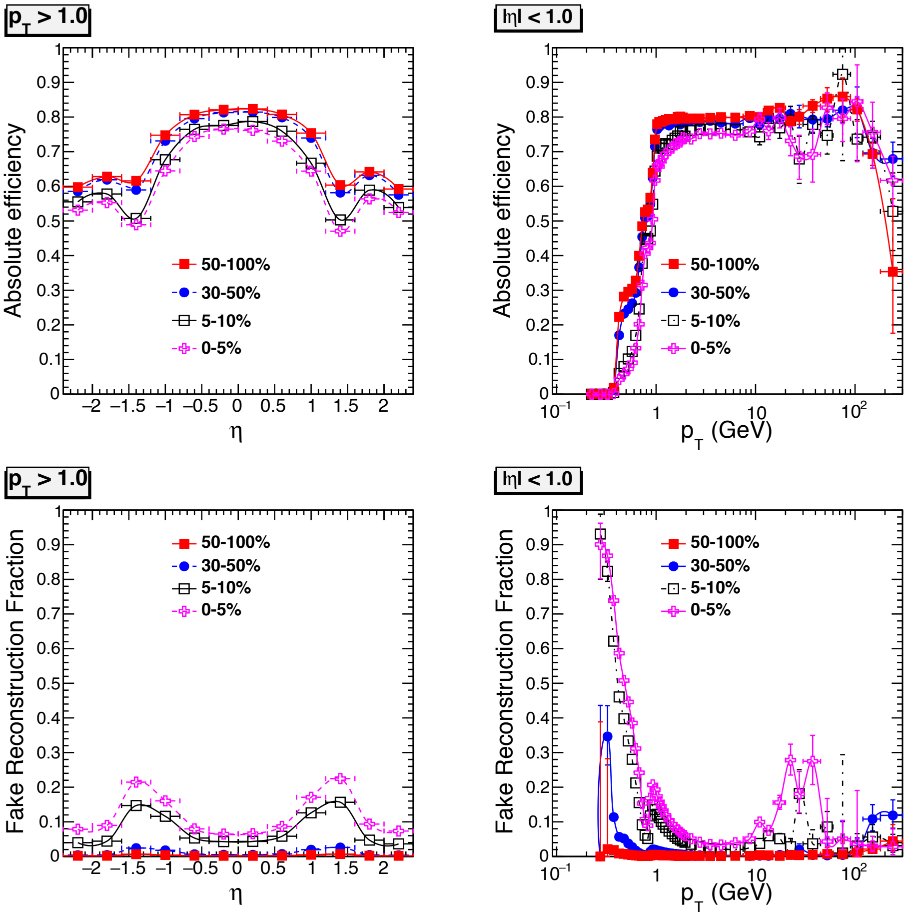

Figure C.2 : The tracking efficiency×acceptance and fake reconstruction rates, fake reconstruction rates are shown in the centrality ranges, 0–5%, 5–10%, 30–50%, and 50–100%. The track p_T is greater than 1.0 GeV and $|\eta| < 1.0$.

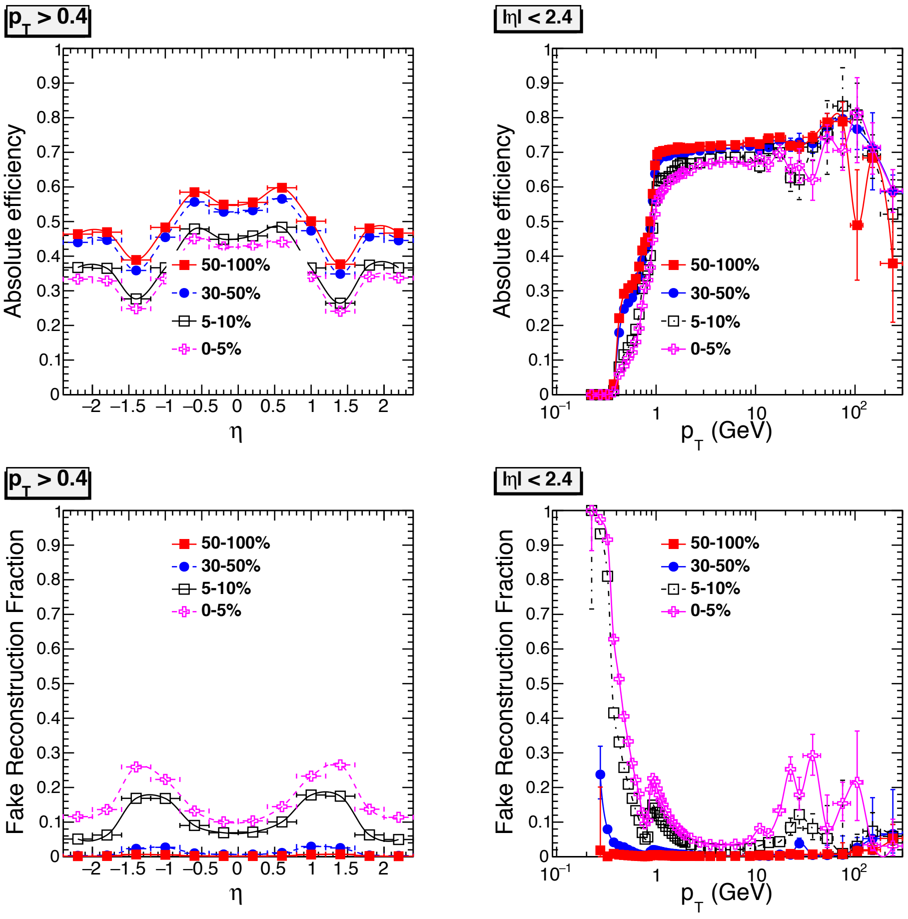

Figure C.3 : The tracking efficiency×acceptance and fake reconstruction rates, fake reconstruction rates are shown in the centrality ranges, 0–5%, 5–10%, 30–50%, and 50–100%. The track p_T is greater than 0.4 GeV and $|\eta| < 2.4$.

Tracking performance in pp reconstruction The tracking performance figures derived from pp reconstruction are shown from Fig. C.4 to Fig. C.5, in terms of tracking efficiency×acceptance, fake reconstruction rates. All the quantities are presented in the $N_{\mathrm{trk}}^{\mathrm{offline}}$ ranges, 40–150, 150–260, 260–400, 400–800, and 800–1200. The centrality range that roughly corresponding to $0 \leq N_{\mathrm{trk}}^{\mathrm{offline}} < 1200$ is around 30–100%.

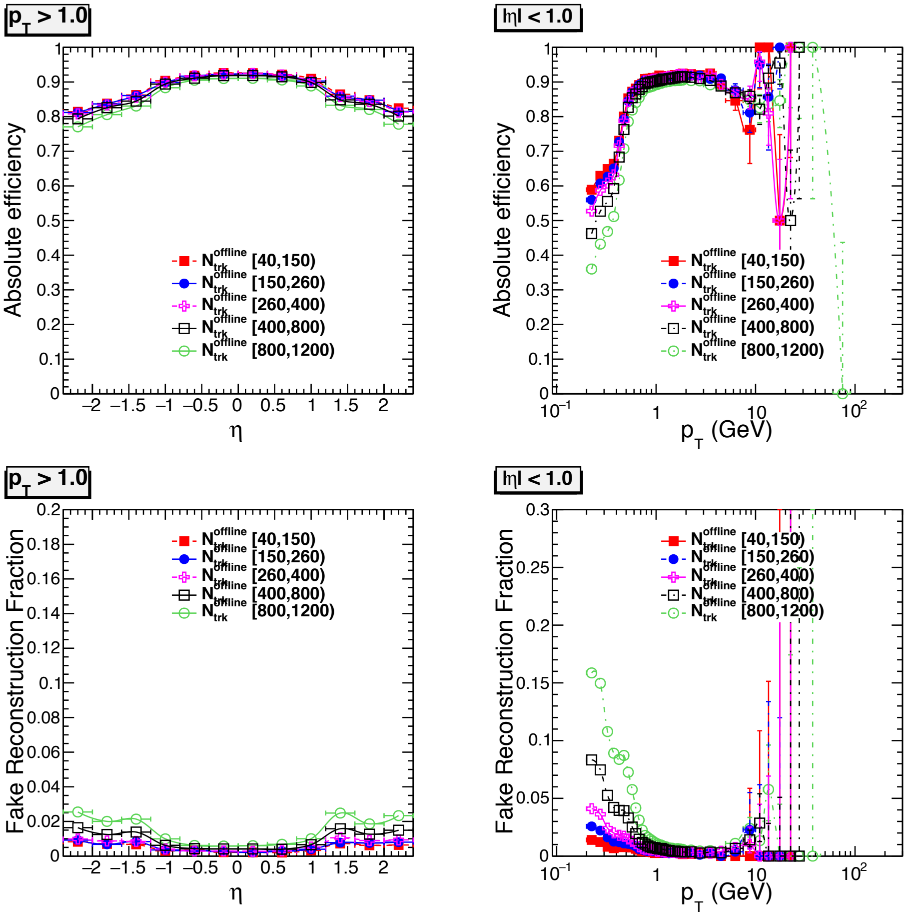

Figure C.4 : The tracking efficiency×acceptance and fake reconstruction rates, fake reconstruction rates are shown in the $N_{\mathrm{trk}}^{\mathrm{offline}}$ ranges, 40–150, 150–260, 260–400, 400–800, and 800–1200. The track p_{T} is greater than 1.0 GeV and $|\eta| < 1.0$.

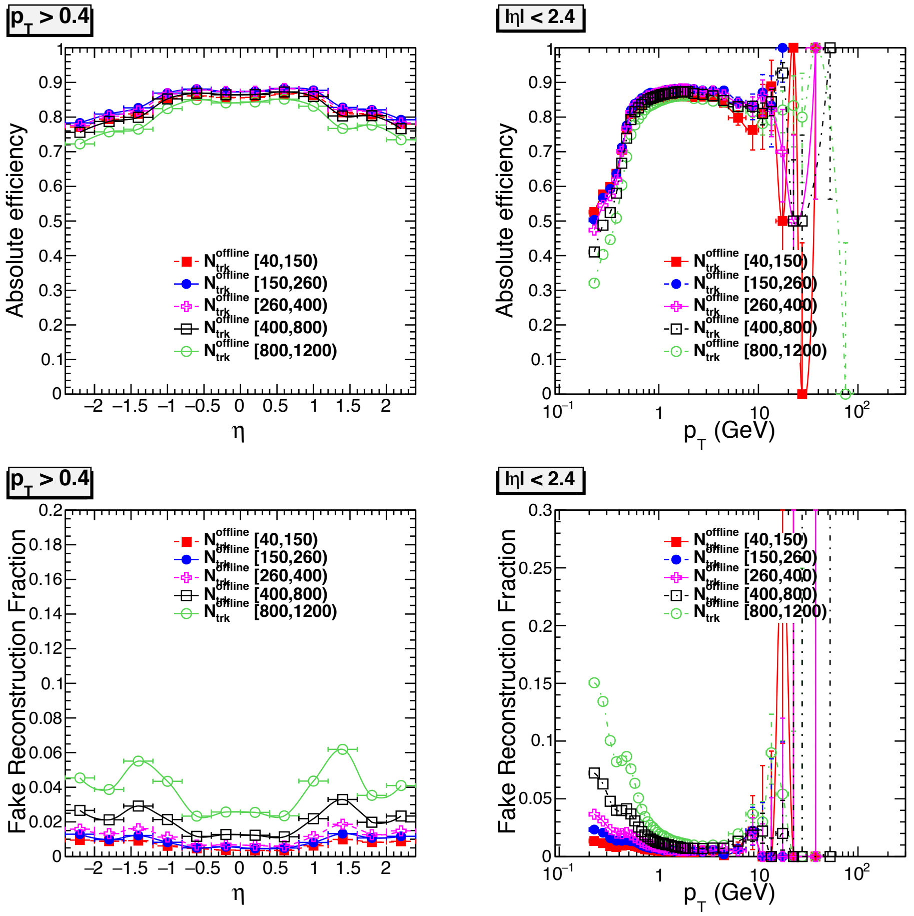

Figure C.5 : The tracking efficiency×acceptance and fake reconstruction rates, fake reconstruction rates are shown in the $N_{\rm trk}^{\rm offline}$ ranges, 40–150, 150–260, 260–400, 400–800, and 800–1200. The track $p_{\rm T}$ is greater than 0.4 GeV and $|\eta| < 2.4$.

Comparison of heavy-ion and pp reconstruction The tracking performance between heavy-ion and pp reconstruction are presented from Fig. C.6 to Fig. C.7. The Centrality ranges of heavy-ion reconstruction are 0–30% and 30–100%. For the pp reconstruction, only 30–100% centrality are processed due to the current reconstruction limits. Clearly, pp reconstruction has better performance over heavy-ion reconstruction in centrality range 30–100%.

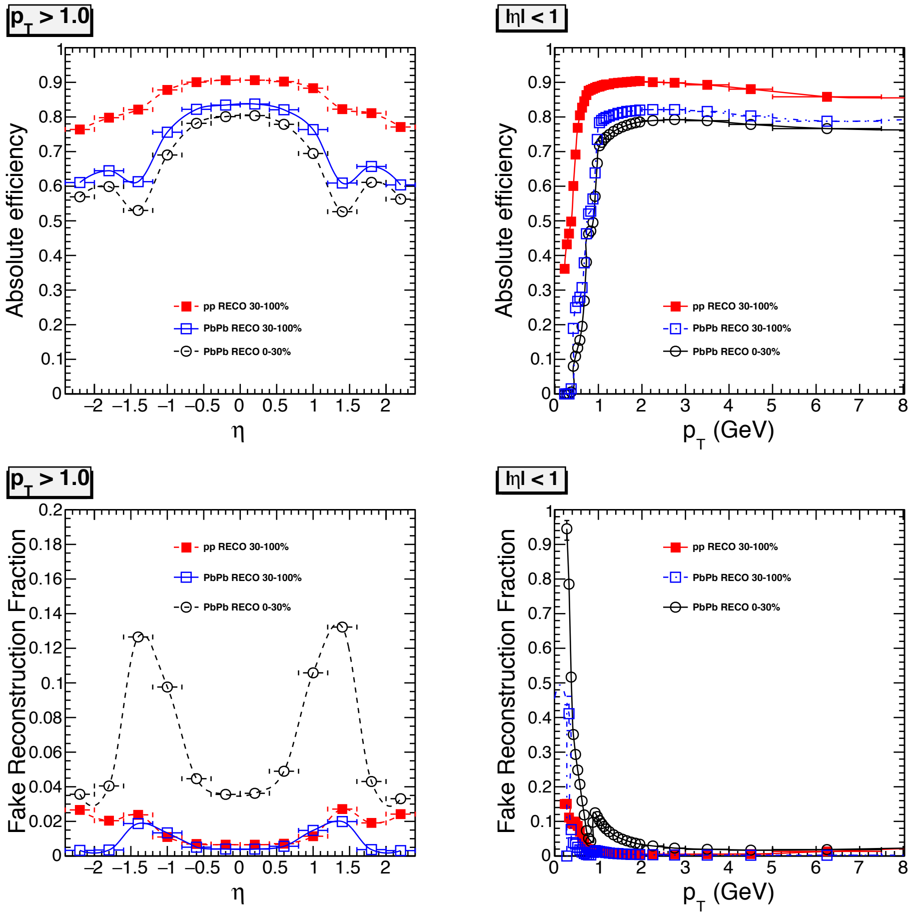

Figure C.6 : The tracking efficiency×acceptance and fake reconstruction rates, fake reconstruction rates are shown in the centrality ranges, 0–30%, and 30–100%. The track p_{T} is greater than 1.0 GeV and $|\eta| < 1.0$.

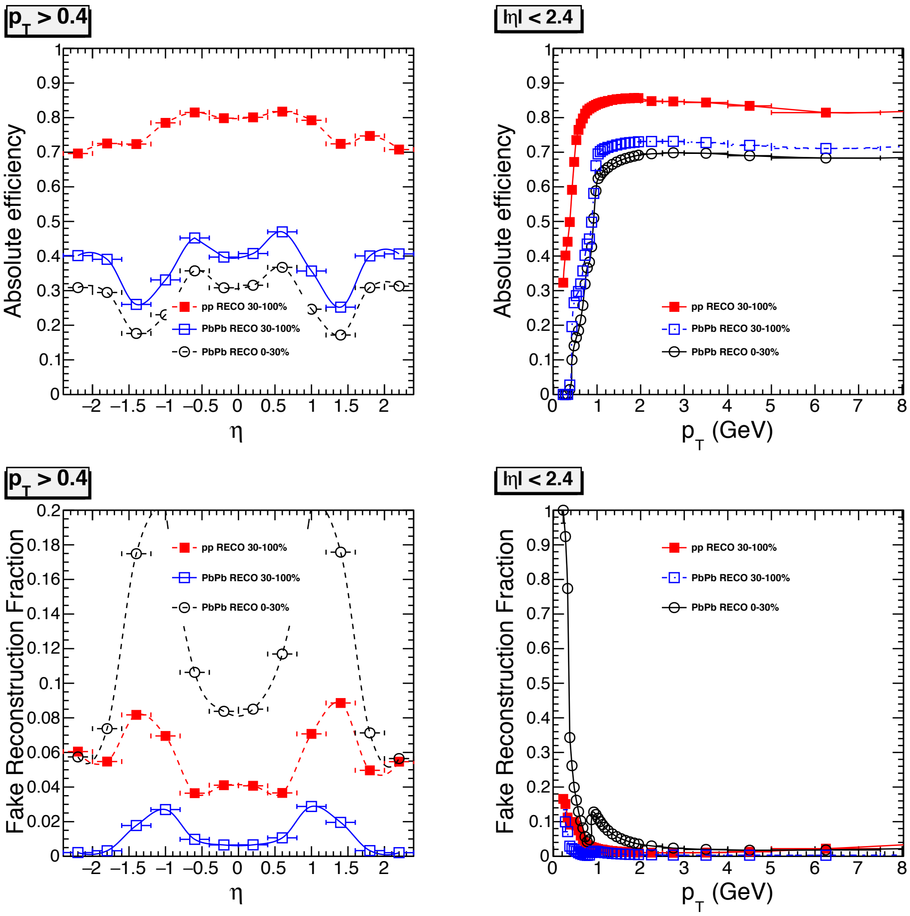

Figure C.7 : The tracking efficiency×acceptance and fake reconstruction rates, fake reconstruction rates are shown in the centrality ranges, 0–30%, and 30–100%. The track p_{T} is greater than 0.4 GeV and $|\eta| < 2.4$.

C.5 Pileup rejection

Pileup, defined as the number of inelastic collisions (interactions) per bunch crossing, has been one of the most important issues in terms of offline analysis for heavy ion physics. Unlike the high energy physics searching for rare particle (e.g., Higgs), the physics that we are interested in is based on a single event. For example, it is possible to have two collisions in one event in a way that one event has a positive charge asymmetry, but the other one has negative charge asymmetry. In this case of pileup equals to two, the charge asymmetry would be averaged to zero if the two collisions are not separated. In this section, the pileup rejection mechanism is described for 8.16 TeV pPb collisions, where similar rejection has been applied on 5.02 TeV pPb data. In PbPb collisions, the average pileup is very low and negligible to the current interest of physics.

For pPb 8 TeV data samples, the pileup scenario (pileup probability) is around 10-25% for the nominal runs depending on the fills and instantaneous luminosity. For the analysis using pPb data, the pileup is a secondary effect, since all the tracks that used in calculating the observables are reconstructing with respect to one vertex. However, in order to make precise measurement, the effect from pileup is also evaluated and a proper filter has been applied to all the events. This pileup filter is not intended to remove events with two collisions, but to only reject the events that are too close to each other spatially. The details of the pileup filter are given below, while systematic checks have been done with different pileup filters and with different pileup samples in the data.

C.5.1 Samples for pileup study

For pileup study, we have used a few different samples to determine what cut values should be used.

For MC:

- pPb EPOS MinBias sample with exactly pileup = 1
- pPb EPOS MinBias sample with exactly pileup = 2.
- pPb EPOS MinBias sample with exactly pileup = 3.

For Data:

- pPb 8 TeV run = 285832, pileup 0.004
- pPb 8 TeV run = 285480, pileup 0.04
- pPb 8 TeV run = 285505, pileup 0.25
- pPb 8 TeV run = 285517, pileup 0.1.

C.5.2 Pileup filters

Multiple collisions events can be identified by the number of good primary vertices in the event. However, not all multiple collision events would lead to multiple reconstructed vertex, nor single collision event would lead to only one reconstructed vertex. In the multiple collision events with only one vertex reconstructed, the two collisions could be close enough that vertex reconstruction algorithm fails. In the case of of a single collisions, the decay of a short lived particle close to the beam line may result in the reconstruction of an additional primary vertex (vertex splitting).

In order to balance between statistics and pileup contamination, one needs to look at the spatial distribution of the vertices, the correlation between number of tracks associated with the second populated vertex and dz value, to come up with a reasonable combinations for the pileup filter. Below a few cuts are proposed for pileup filters.

- dz cut : accept those events that have two vertices where dz, the z distance between the most populated vertex and other vertices, is larger than some value, i.e, 1 cm.
- Gplus cut: according to the number of tracks w.r.t the second populated vertex, cut on a dz value.
- vtx1 cut: accept events that only has one vertex.

The available filters with instructions can be found in here, github, as,

- $pileupFilter\_pPb8TeV\_vtx1$, with only 1 reconstructed vertex.
- $pileupFilter\_pPb8TeV\_Gplus$, with only N_{trk} vs dz cut.
- $olvFilter\_pPb8TeV\_dz1p0$, with N_{trk} vs dz cut plus dz cut at 1 cm. olvFilter stands for "overlapping vertex filter", which only filters those events with 2 or more vertices are too close to each other.

In Table. C.3, it shows the cut values in N_{trk} vs dz cut. From Fig. C.8 to Fig. C.9, they are showing the N_{trk} vs dz distribution in both MC and data to indicate where the cut values are.

Table C.3 : Table of N_{trk} vs dz cuts.

N_{trk}	dz
0–4	NA
5	4.0
6	1.5
7	1.0
8	0.6
9	0.5
10	0.4
11	0.3
12–15	0.2
16–19	0.1
20+	0.0

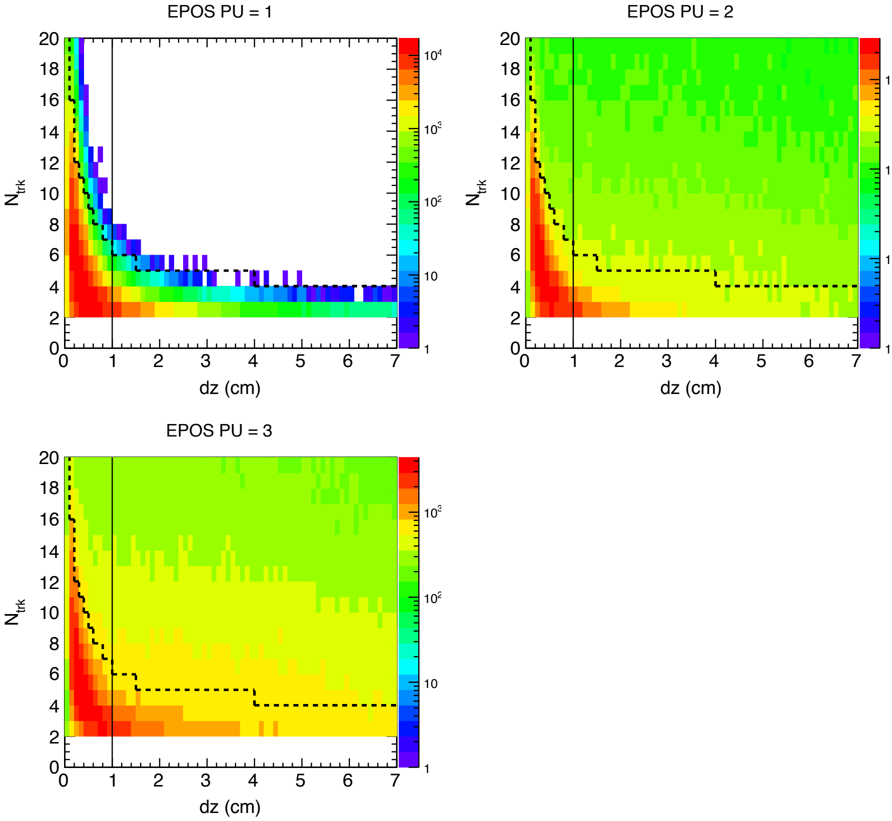
EPOS PU = 1

EPOS PU = 2

EPOS PU = 3

Figure C.8 : $N_{\rm trk}$ vs dz from MC is shown and the line is indicating where the cut values are.

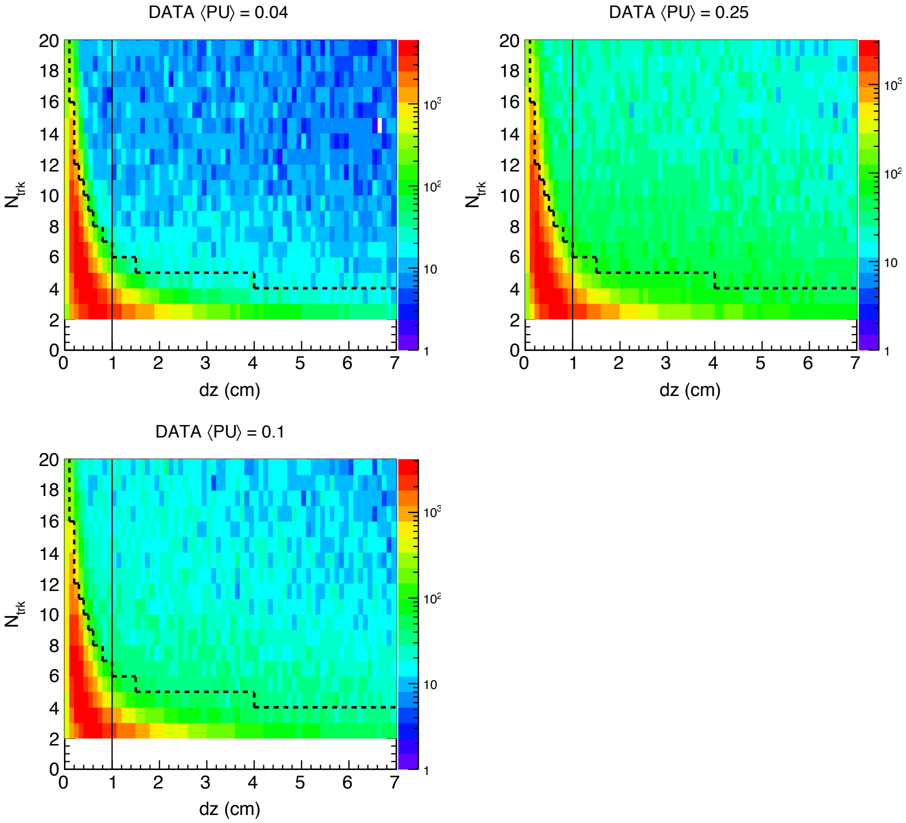

Figure C.9 : N_{trk} vs dz from Data is shown and the line is indicating where the cut values are.

C.5.3 Pileup Filter Performance

The available filters are applied on various MC samples and Data samples to see the filter efficiency. From Fig. C.10 to Fig. C.11, they show the accepted fraction of events after applying various filters as a function of $N_{\mathrm{trk}}^{\mathrm{offline}}$. The filter efficiency can be used as a measure of how much statistics would be reduced after using each filter as well as an estimate of the remaining pileup contaminations given the average pileup μ. The overall filter efficiency for $pileupFilter\_pPb8TeV\_Gplus$ filter is around 99.6%, while the purity of the remaining sample is about 97.3%. In this analysis, the $pileupFilter\_pPb8TeV\_Gplus$ filter is only applied for systematic studies and the default filter is $olvFilter\_pPb8TeV\_dz1p0$.

In order to make sure the $pileupFilter\_pPb8TeV\_Gplus$ filter is effective in terms of removing pileup events, the HF sum E_{T} and $N_{\mathrm{trk}}^{\mathrm{offline}}$ are compared with different pileup samples before and after the filter. The distributions from different pileup samples should be expected to be the same if the pileup events are removed. In Fig. C.12 and Fig. C.13, the HF sum E_{T} and $N_{\mathrm{trk}}^{\mathrm{offline}}$ are shown before pileup filter, and clearly the HF sum E_{T} has a clear ordering with the level of pileup in the sample. For $N_{\mathrm{trk}}^{\mathrm{offline}}$, since our mutiplicity definition is with respect to one vertex, the pileup effect is a second order effect that the difference between different pileup level is much smaller comparing to that of HF sum E_{T}. In Fig. C.14 and Fig. C.15, the same two distributions are shown after the pileup filter, and as expected, both distributions are almost the same showing the pileup events are mostly removed.

The vertex merging rate, the probability of having 2 real collisions but with only one vertex reconstructed, needs to be estimated in order to understand the efficiency of the filters. For example, for the $pileUpFilter\_pPb8TeV\_vtx1$, we have filtered out all the events that have 2 reconstructed vertices, but the remaining events might still

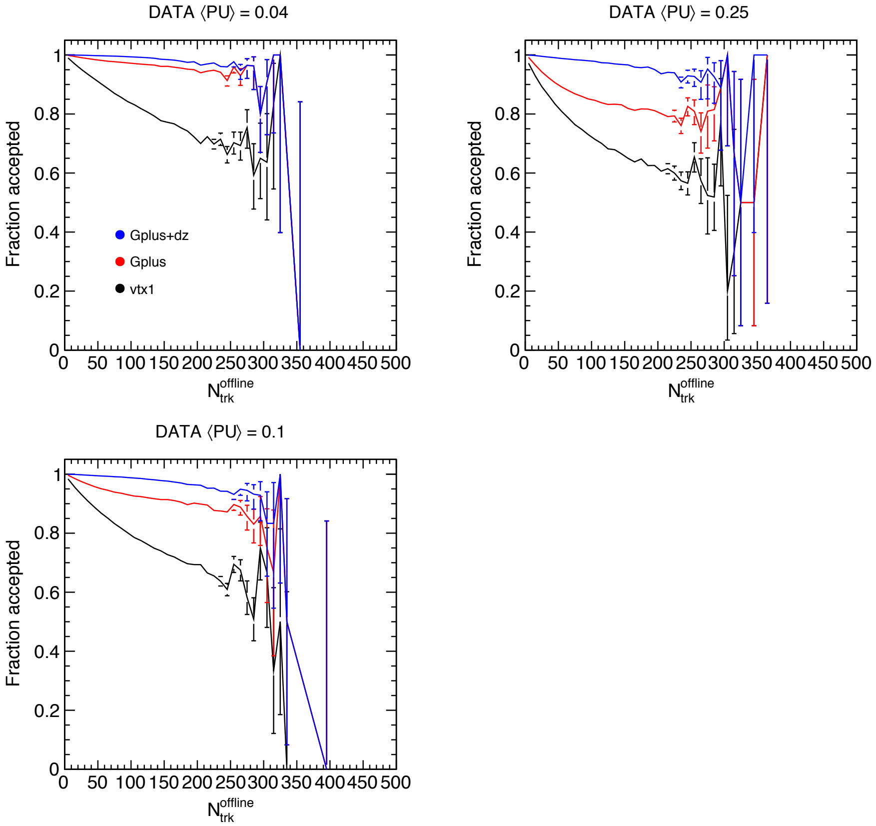

Figure C.10 : The accepted fraction of number of events is shown as a function $N_{\text{trk}}^{\text{offline}}$ with different defined pileup filters for different runs.

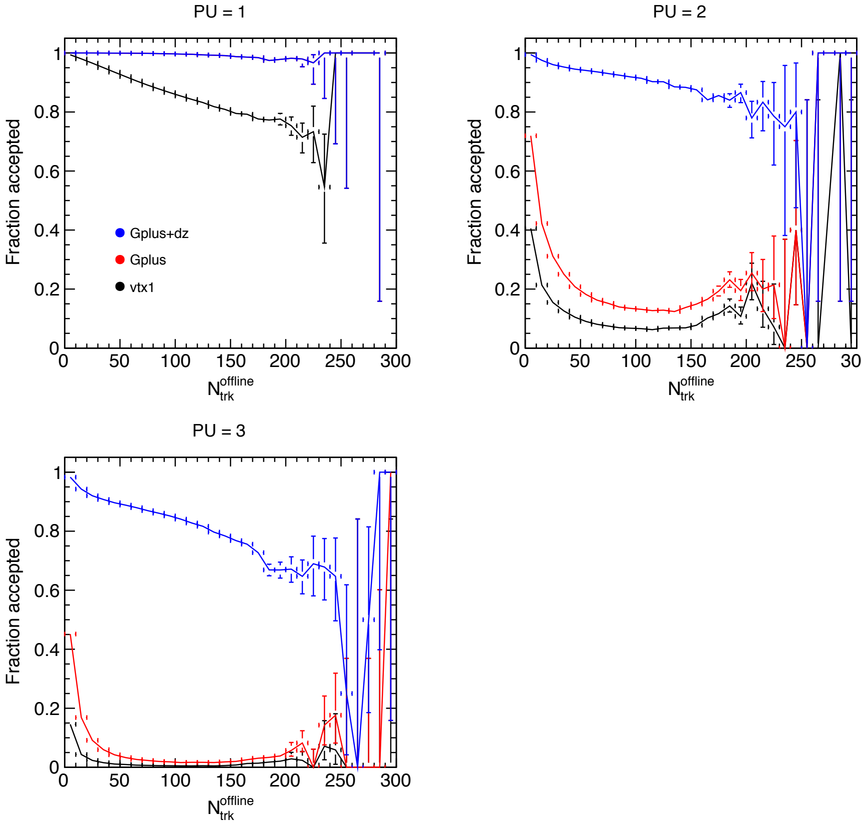

Figure C.11 : The accepted fraction of number of events is shown as a function $N_{\mathrm{trk}}^{\mathrm{offline}}$ with different defined pileup filters for different pileup samples.

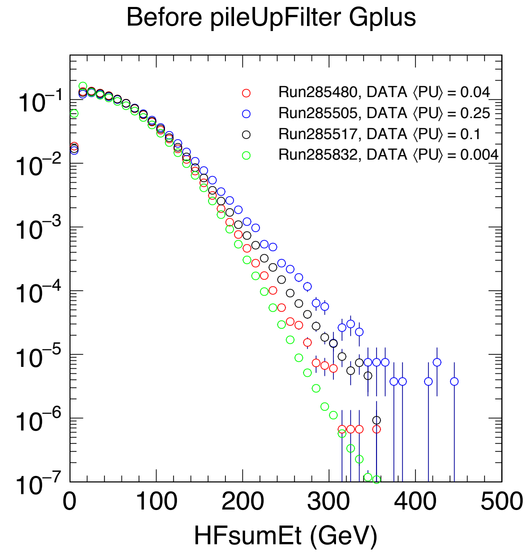

Figure C.12 : The HF sum E_{T} distributions with different pileup runs before the $pileupFilter\_pPb8TeV\_Gplus$ are shown.

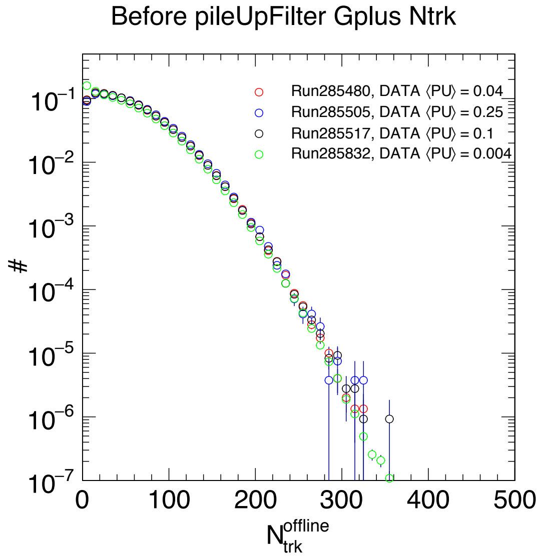

Figure C.13 : The $N_{\mathrm{trk}}^{\mathrm{offline}}$ distributions with different pileup runs before the $pileupFilter\_pPb8TeV\_Gplus$ are shown.

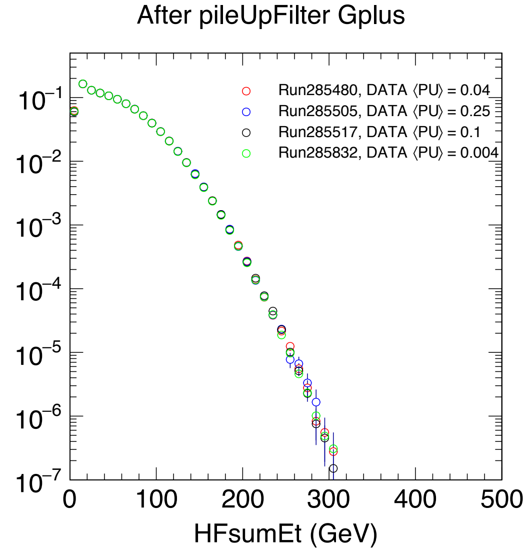

Figure C.14 : The HF sum E_{T} distributions with different pileup runs after the $pileupFilter\_pPb8TeV\_Gplus$ are shown.

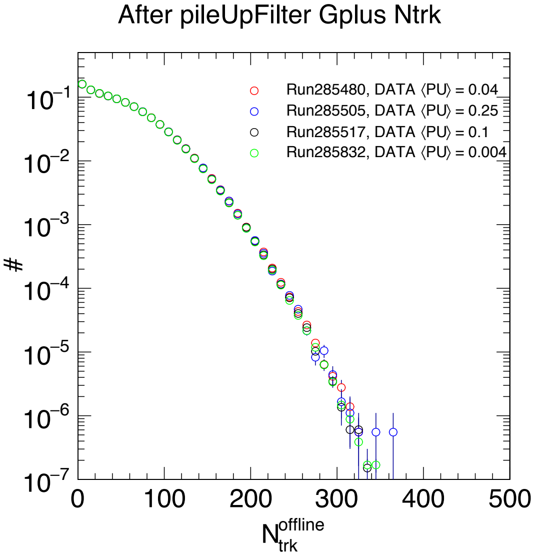

Figure C.15 : The $N_{\mathrm{trk}}^{\mathrm{offline}}$ distributions with different pileup runs after the $pileupFilter\_pPb8TeV\_Gplus$ are shown.

have 2 real collisions. In EPOS pileup = 2 samples, there are 10% chances that the algorithm fails to reconstruct a valid vertex, given there are two real collisions in the event. With the possible highest pileup scenario in the data (25%), the probability of having at least 2 real collisions in a MinBias sample, is around 11%, assuming the pileup follows Poisson statistics. Therefore, the vertex merging probability after pileup filters is around 1.1%.

Bibliography

[1] G. Aad *et al.*, “Observation of a new particle in the search for the Standard Model Higgs boson with the ATLAS detector at the LHC,” *Phys. Lett. B*, vol. 716, 2012.

[2] S. Chatrchyan *et al.*, “Observation of a new boson at a mass of 125 GeV with the CMS experiment at the LHC,” *Phys. Lett. B*, vol. 716, 2012.

[3] G. Baym, “The Hadronization Transition in the Early Universe,” *Nucl. Phys. A*, vol. 447, p. 463C, 1986.

[4] M. H. Seymour, “Quantum chromodynamics,” in *2004 European School of High-Energy Physics, Sant Feliu de Guixols, Spain, 30 May - 12 June 2004*, pp. 49–94, 2005.

[5] D. J. Gross and F. Wilczek, “Ultraviolet behavior of non-abelian gauge theories,” *Phys. Rev. Lett.*, vol. 30, p. 1343, Jun 1973.

[6] H. D. Politzer, “Reliable perturbative results for strong interactions?,” *Phys. Rev. Lett.*, vol. 30, p. 1346, Jun 1973.

[7] R. C. Group, “Measurement of the Inclusive Jet Cross Section using the Midpoint Algorithm in Run II at CDF,” 2006.

[8] K. Safarik, “Heavy ion physics,” in *High-energy physics. Proceedings, European School, ESHEP’99, Casta-Papiernicka, Slovak Republic, August 22-September*

4, 1999, pp. 267–288, 1999.

[9] E. V. Shuryak, “Theory of Hadronic Plasma,” *Sov. Phys. JETP*, vol. 47, p. 212, 1978. [Zh. Eksp. Teor. Fiz.74,408(1978)].

[10] J. C. Collins and M. J. Perry, “Superdense Matter: Neutrons Or Asymptotically Free Quarks?,” *Phys. Rev. Lett.*, vol. 34, p. 1353, 1975.

[11] N. Cabibbo and G. Parisi, “Exponential Hadronic Spectrum and Quark Liberation,” *Phys. Lett. B*, vol. 59, p. 67, 1975.

[12] B. A. Freedman and L. D. McLerran, “Fermions and Gauge Vector Mesons at Finite Temperature and Density. 3. The Ground State Energy of a Relativistic Quark Gas,” *Phys. Rev. D*, vol. 16, p. 1169, 1977.

[13] K. Fukushima and T. Hatsuda, “The phase diagram of dense QCD,” *Rept. Prog. Phys.*, vol. 74, p. 014001, 2011.

[14] M. Fukugita, M. Okawa, and A. Ukawa, “Finite-size scaling study of the deconfining phase transition in pure su(3) lattice gauge theory,” *Nuclear Physics B*, vol. 337, no. 1, p. 181, 1990.

[15] G. ’t Hooft, “Naturalness, chiral symmetry, and spontaneous chiral symmetry breaking,” *NATO Sci. Ser. B*, vol. 59, p. 135, 1980.

[16] W. Busza, K. Rajagopal, and W. van der Schee, “Heavy Ion Collisions: The Big Picture, and the Big Questions,” 2018.

[17] P. Romatschke and U. Romatschke, “Relativistic Fluid Dynamics Out of Equilibrium,” 2017.

[18] H. Song and U. W. Heinz, “Causal viscous hydrodynamics in 2+1 dimensions for relativistic heavy-ion collisions,” *Phys. Rev. C*, vol. 77, p. 064901, 2008.

[19] Y. V. Kovchegov, “AdS/CFT applications to relativistic heavy ion collisions: a brief review,” *Rept. Prog. Phys.*, vol. 75, p. 124301, 2012.

[20] B. I. Abelev *et al.*, “Observation of charge-dependent azimuthal correlations and possible local strong parity violation in heavy ion collisions,” *Phys. Rev. C*, vol. 81, p. 054908, 2010.

[21] S. Chatrchyan *et al.*, “Observation and studies of jet quenching in PbPb collisions at nucleon-nucleon center-of-mass energy = 2.76 TeV,” *Phys. Rev.*, vol. C84, p. 024906, 2011.

[22] S. Salur, “First Direct Measurement of Jets in s(NN)**(1/2) = 200-GeV Heavy Ion Collisions by STAR,” *Eur. Phys. J.*, vol. C61, pp. 761–767, 2009.

[23] J. Adams *et al.*, “Experimental and theoretical challenges in the search for the quark gluon plasma: The STAR Collaboration’s critical assessment of the evidence from RHIC collisions,” *Nucl. Phys.*, vol. A757, pp. 102–183, 2005.

[24] K. Adcox *et al.*, “Formation of dense partonic matter in relativistic nucleus-nucleus collisions at RHIC: Experimental evaluation by the PHENIX collaboration,” *Nucl. Phys.*, vol. A757, pp. 184–283, 2005.

[25] I. Arsene *et al.*, “Quark gluon plasma and color glass condensate at RHIC? The Perspective from the BRAHMS experiment,” *Nucl. Phys. A*, vol. 757, p. 1, 2005.

[26] B. B. Back *et al.*, “The PHOBOS perspective on discoveries at RHIC,” *Nucl. Phys. A*, vol. 757, p. 28, 2005.

[27] S. Chatrchyan *et al.*, “Indications of suppression of excited Υ states in PbPb collisions at $\sqrt{s_{NN}} = 2.76$ TeV,” *Phys. Rev. Lett.*, vol. 107, p. 052302, 2011.

[28] A. Adare *et al.*, “J/ψ Production vs Centrality, Transverse Momentum, and Rapidity in Au+Au Collisions at $\sqrt{s_{NN}} = 200$ GeV,” *Phys. Rev. Lett.*, vol. 98, p. 232301, 2007.

[29] H. Satz, “Colour deconfinement and quarkonium binding,” *J. Phys. G*, vol. 32, p. R25, 2006.

[30] A. Mocsy and P. Petreczky, “Color screening melts quarkonium,” *Phys. Rev. Lett.*, vol. 99, p. 211602, 2007.

[31] C.-Y. Wong, “Heavy quarkonia in quark-gluon plasma,” *Phys. Rev. C*, vol. 72, p. 034906, 2005.

[32] J.-F. Paquet, C. Shen, G. Denicol, M. Luzum, B. Schenke, S. Jeon, and C. Gale, “Thermal and prompt photons at RHIC and the LHC,” *Nucl. Phys. A*, vol. 956, p. 409, 2016.

[33] S. Chatrchyan *et al.*, “Measurement of isolated photon production in pp and PbPb collisions at $\sqrt{s_{NN}} = 2.76$ TeV,” *Phys. Lett. B*, vol. 710, pp. 256–277, 2012.

[34] J. Adam *et al.*, “Direct photon production in Pb-Pb collisions at $\sqrt{s_{NN}} = 2.76$ TeV,” *Phys. Lett.*, vol. B754, pp. 235–248, 2016.

[35] S. Afanasiev *et al.*, "Measurement of Direct Photons in Au+Au Collisions at $\sqrt{s_{NN}} = 200$ GeV," *Phys. Rev. Lett.*, vol. 109, p. 152302, 2012.

[36] A. Adare *et al.*, "Direct photon production in d+Au collisions at $\sqrt{s_{NN}} = 200$ GeV," *Phys. Rev. C*, vol. 87, p. 054907, 2013.

[37] A. Adare *et al.*, "Observation of direct-photon collective flow in $\sqrt{s_{NN}} = 200$ GeV Au+Au collisions," *Phys. Rev. Lett.*, vol. 109, p. 122302, 2012.

[38] B. I. Abelev *et al.*, "Long range rapidity correlations and jet production in high energy nuclear collisions," *Phys. Rev. C*, vol. 80, p. 064912, 2009.

[39] A. Adare *et al.*, "Dihadron azimuthal correlations in Au+Au collisions at s(NN)**(1/2) = 200-GeV," *Phys. Rev. C*, vol. 78, p. 014901, 2008.

[40] B. Alver *et al.*, "High transverse momentum triggered correlations over a large pseudorapidity acceptance in Au+Au collisions at $\sqrt{s_{NN}} = 200$ GeV," *Phys. Rev. Lett.*, vol. 104, p. 062301, 2010.

[41] B. Alver *et al.*, "System size dependence of cluster properties from two-particle angular correlations in Cu+Cu and Au+Au collisions at s(NN)**(1/2) = 200-GeV," *Phys. Rev.*, vol. C81, p. 024904, 2010.

[42] S. Chatrchyan *et al.*, "Measurement of higher-order harmonic azimuthal anisotropy in PbPb collisions at $\sqrt{s_{NN}} = 2.76$ TeV," *Phys. Rev. C*, vol. 89, p. 044906, 2014.

[43] L. McLerran and V. Skokov, "Comments About the Electromagnetic Field in Heavy-Ion Collisions," *Nucl. Phys. A*, vol. 929, p. 184, 2014.

[44] U. Gursoy, D. Kharzeev, and K. Rajagopal, “Magnetohydrodynamics, charged currents and directed flow in heavy ion collisions,” *Phys. Rev. C*, vol. 89, no. 5, p. 054905, 2014.

[45] S. K. Das, S. Plumari, S. Chatterjee, J. Alam, F. Scardina, and V. Greco, “Directed Flow of Charm Quarks as a Witness of the Initial Strong Magnetic Field in Ultra-Relativistic Heavy Ion Collisions,” *Phys. Lett. B*, vol. 768, p. 260, 2017.

[46] K. Hattori and D. Satow, “Electrical Conductivity of Quark-Gluon Plasma in Strong Magnetic Fields,” *Phys. Rev. D*, vol. 94, no. 11, p. 114032, 2016.

[47] K. Tuchin, “On viscous flow and azimuthal anisotropy of quark-gluon plasma in strong magnetic field,” *J. Phys. G*, vol. 39, p. 025010, 2012.

[48] R. K. Mohapatra, P. S. Saumia, and A. M. Srivastava, “Enhancement of flow anisotropies due to magnetic field in relativistic heavy-ion collisions,” *Mod. Phys. Lett. A*, vol. 26, p. 2477, 2011.

[49] T. D. Lee, “A theory of spontaneous T violation,” *Phys. Rev. D*, vol. 8, p. 1226, 1973.

[50] T. D. Lee and G. C. Wick, “Vacuum stability and vacuum excitation in a spin-0 field theory,” *Phys. Rev. D*, vol. 9, p. 2291, 1974.

[51] P. D. Morley and I. A. Schmidt, “Strong P, CP, T violations in heavy-ion collisions,” *Z. Phys. C*, vol. 26, p. 627, 1985.

[52] D. Kharzeev, R. D. Pisarski, and M. H. G. Tytgat, “Possibility of spontaneous parity violation in hot QCD,” *Phys. Rev. Lett.*, vol. 81, p. 512, 1998.

[53] S. L. Adler, “Axial vector vertex in spinor electrodynamics,” *Phys. Rev.*, vol. 177, pp. 2426–2438, 1969.

[54] J. S. Bell and R. Jackiw, “A PCAC puzzle: pi0 –¿ gamma gamma in the sigma model,” *Nuovo Cim. A*, vol. 60, p. 47, 1969.

[55] D. E. Kharzeev, J. Liao, S. A. Voloshin, and G. Wang, “Chiral magnetic and vortical effects in high-energy nuclear collisions — a status report,” *Prog. Part. Nucl. Phys.*, vol. 88, p. 1, 2016.

[56] D. E. Kharzeev, L. D. McLerran, and H. J. Warringa, “The effects of topological charge change in heavy ion collisions: ’Event by event P and CP violation’,” *Nucl. Phys. A*, vol. 803, p. 227, 2008.

[57] D. Kharzeev, “Parity violation in hot QCD: Why it can happen, and how to look for it,” *Phys. Lett. B*, vol. 633, p. 260, 2006.

[58] D. Kharzeev and A. Zhitnitsky, “Charge separation induced by P-odd bubbles in QCD matter,” *Nucl. Phys. A*, vol. 797, p. 67, 2007.

[59] D. T. Son and A. R. Zhitnitsky, “Quantum anomalies in dense matter,” *Phys. Rev. D*, vol. 70, p. 074018, 2004.

[60] M. A. Metlitski and A. R. Zhitnitsky, “Anomalous axion interactions and topological currents in dense matter,” *Phys. Rev. D*, vol. 72, p. 045011, 2005.

[61] D. E. Kharzeev and H.-U. Yee, “Chiral magnetic wave,” *Phys. Rev. D*, vol. 83, p. 085007, 2011.

[62] Y. Burnier, D. E. Kharzeev, J. Liao, and H.-U. Yee, “Chiral magnetic wave at finite baryon density and the electric quadrupole moment of quark-gluon

plasma in heavy ion collisions," *Phys. Rev. Lett.*, vol. 107, p. 052303, 2011.

[63] S. A. Voloshin, "Parity violation in hot QCD: How to detect it," *Phys. Rev. C*, vol. 70, p. 057901, 2004.

[64] B. Abelev *et al.*, "Charge separation relative to the reaction plane in Pb-Pb collisions at $\sqrt{s_{NN}} = 2.76$ TeV," *Phys. Rev. Lett.*, vol. 110, p. 012301, 2013.

[65] F. Wang, "Effects of cluster particle correlations on local parity violation observables," *Phys. Rev. C*, vol. 81, p. 064902, 2010.

[66] A. Bzdak, V. Koch, and J. Liao, "Azimuthal correlations from transverse momentum conservation and possible local parity violation," *Phys. Rev. C*, vol. 83, p. 014905, 2011.

[67] S. Schlichting and S. Pratt, "Charge conservation at energies available at the BNL Relativistic Heavy Ion Collider and contributions to local parity violation observables," *Phys. Rev. C*, vol. 83, p. 014913, 2011.

[68] A. Bzdak, V. Koch, and J. Liao, "Charge-dependent correlations in relativistic heavy ion collisions and the chiral magnetic effect," *Lect. Notes Phys.*, vol. 871, p. 503, 2013.

[69] L. Adamczyk *et al.*, "Observation of charge asymmetry dependence of pion elliptic flow and the possible chiral magnetic wave in heavy-ion collisions," *Phys. Rev. Lett.*, vol. 114, p. 252302, 2015.

[70] J. Adam *et al.*, "Charge-dependent flow and the search for the chiral magnetic wave in Pb-Pb collisions at $\sqrt{s_{NN}} = 2.76$ TeV," *Phys. Rev. C*, vol. 93, p. 044903, 2016.

[71] A. Bzdak and P. Bozek, “Contributions to the event-by-event charge asymmetry dependence for the elliptic flow of π^+ and π^- in heavy-ion collisions,” *Phys. Lett. B*, vol. 726, p. 239, 2013.

[72] Y. Hatta, A. Monnai, and B.-W. Xiao, “Elliptic flow difference of charged pions in heavy-ion collisions,” *Nucl. Phys. A*, vol. 947, p. 155, 2016.

[73] V. Khachatryan *et al.*, “Observation of long-range near-side angular correlations in proton-proton collisions at the LHC,” *JHEP*, vol. 09, p. 091, 2010.

[74] G. Aad *et al.*, “Observation of long-range elliptic azimuthal anisotropies in $\sqrt{s} = 13$ and 2.76 TeV pp collisions with the ATLAS detector,” *Phys. Rev. Lett.*, vol. 116, p. 172301, 2016.

[75] V. Khachatryan *et al.*, “Measurement of long-range near-side two-particle angular correlations in pp collisions at $\sqrt{s}$ =13 TeV,” *Phys. Rev. Lett.*, vol. 116, no. 17, p. 172302, 2016.

[76] V. Khachatryan *et al.*, “Evidence for collectivity in pp collisions at the LHC,” *Phys. Lett.*, vol. B765, pp. 193–220, 2017.

[77] S. Chatrchyan *et al.*, “Observation of long-range near-side angular correlations in pPb collisions at the LHC,” *Phys. Lett. B*, vol. 718, p. 795, 2013.

[78] B. Abelev *et al.*, “Long-range angular correlations on the near and away side in pPb collisions at $\sqrt{s_{NN}} = 5.02$ TeV,” *Phys. Lett. B*, vol. 719, p. 29, 2013.

[79] G. Aad *et al.*, “Observation of associated near-side and away-side long-range correlations in $\sqrt{s_{NN}} = 5.02$ TeV proton-lead collisions with the ATLAS detector,” *Phys. Rev. Lett.*, vol. 110, p. 182302, 2013.

[80] R. Aaij *et al.*, "Measurements of long-range near-side angular correlations in $\sqrt{s_{\mathrm{NN}}} = 5\mathrm{TeV}$ proton-lead collisions in the forward region," *Phys. Lett.*, vol. B762, pp. 473–483, 2016.

[81] V. Khachatryan *et al.*, "Long-range two-particle correlations of strange hadrons with charged particles in pPb and PbPb collisions at LHC energies," *Phys. Lett.*, vol. B742, pp. 200–224, 2015.

[82] B. B. Abelev *et al.*, "Long-range angular correlations of π, K and p in p–Pb collisions at $\sqrt{s_{NN}} = 5.02$ TeV," *Phys. Lett. B*, vol. 726, p. 164, 2013.

[83] S. Chatrchyan *et al.*, "Multiplicity and transverse momentum dependence of two- and four-particle correlations in pPb and PbPb collisions," *Phys. Lett. B*, vol. 724, p. 213, 2013.

[84] G. Aad *et al.*, "Measurement of long-range pseudorapidity correlations and azimuthal harmonics in $\sqrt{s_{_{NN}}} = 5.02$ TeV proton-lead collisions with the ATLAS detector," *Phys. Rev.*, vol. C90, no. 4, p. 044906, 2014.

[85] V. Khachatryan *et al.*, "Evidence for Collective Multiparticle Correlations in p-Pb Collisions," *Phys. Rev. Lett.*, vol. 115, no. 1, p. 012301, 2015.

[86] K. Dusling, W. Li, and B. Schenke, "Novel collective phenomena in high-energy proton–proton and proton–nucleus collisions," *Int. J. Mod. Phys.*, vol. E25, no. 01, p. 1630002, 2016.

[87] V. Khachatryan *et al.*, "Observation of charge-dependent azimuthal correlations in pPb collisions and its implication for the search for the chiral magnetic effect," *Phys. Rev. Lett.*, vol. 118, no. 12, p. 122301, 2017.

[88] B. Alver, M. Baker, C. Loizides, and P. Steinberg, “The PHOBOS Glauber Monte Carlo.” 2008.

[89] V. Khachatryan *et al.*, “Multiplicity and rapidity dependence of strange hadron production in pp, pPb, and PbPb collisions at the LHC,” *Phys. Lett.*, vol. B768, pp. 103–129, 2017.

[90] B. Alver and G. Roland, “Collision geometry fluctuations and triangular flow in heavy-ion collisions,” *Phys. Rev.*, vol. C81, p. 054905, 2010. [Erratum: Phys. Rev.C82,039903(2010)].

[91] G. Aad *et al.*, “Measurement of event-plane correlations in $\sqrt{s_{NN}} = 2.76$ TeV lead-lead collisions with the ATLAS detector,” *Phys. Rev. C*, vol. 90, p. 024905, 2014.

[92] J. Schukraft, A. Timmins, and S. A. Voloshin, “Ultra-relativistic nuclear collisions: event shape engineering,” *Phys. Lett. B*, vol. 719, p. 394, 2013.

[93] L. Evans and P. Bryant, “Lhc machine,” *Journal of Instrumentation*, vol. 3, no. 08, p. S08001, 2008.

[94] “cern-accelerators-optics.”

[95] T. Sakuma and T. McCauley, “Detector and Event Visualization with SketchUp at the CMS Experiment,” *J. Phys. Conf. Ser.*, vol. 513, p. 022032, 2014.

[96] D. Sprenger, M. Weber, R. Adolphi, R. Brauer, L. Feld, K. Klein, A. Ostaptchuk, S. Schael, and B. Wittmer, “Validation of Kalman Filter alignment algorithm with cosmic-ray data using a CMS silicon strip tracker endcap,” *JINST*, vol. 5, p. P06007, 2010.

[97] G. Giurgiu, D. Fehling, P. Maksimovic, M. Swartz, and V. Chiochia, “Pixel Hit Reconstruction with the CMS Detector,” 2008.

[98] S. Cittolin, “The data acquisition and reduction challenge at the Large Hadron Collider,” *Phil. Trans. Roy. Soc. Lond.*, vol. A370, pp. 950–964, 2012.

[99] M. Gyulassy and X.-N. Wang, “HIJING 1.0: A Monte Carlo program for parton and particle production in high-energy hadronic and nuclear collisions,” *Comput. Phys. Commun.*, vol. 83, p. 307, 1994.

[100] T. Pierog, I. Karpenko, J. M. Katzy, E. Yatsenko, and K. Werner, “EPOS LHC: Test of collective hadronization with data measured at the CERN Large Hadron Collider,” *Phys. Rev.*, vol. C92, no. 3, p. 034906, 2015.

[101] I. P. Lokhtin, L. V. Malinina, S. V. Petrushanko, A. M. Snigirev, I. Arsene, and K. Tywoniuk, “Heavy ion event generator HYDJET++ (HYDrodynamics plus JETs),” *Comput. Phys. Commun.*, vol. 180, pp. 779–799, 2009.

[102] S. Agostinelli *et al.*, “GEANT4: A Simulation toolkit,” *Nucl. Instrum. Meth.*, vol. A506, pp. 250–303, 2003.

[103] S. Chatrchyan *et al.*, “Description and performance of track and primary-vertex reconstruction with the CMS tracker,” *JINST*, vol. 9, no. 10, p. P10009, 2014.

[104] R. Fruhwirth, “Application of Kalman filtering to track and vertex fitting,” *Nucl. Instrum. Meth.*, vol. A262, pp. 444–450, 1987.

[105] S. Porteboeuf, T. Pierog, and K. Werner, “Producing Hard Processes Regarding the Complete Event: The EPOS Event Generator,” in *Proceedings, 45th Ren-*

contres de Moriond on QCD and High Energy Interactions: La Thuile, Italy, March 13-20, 2010, pp. 135–140, Gioi Publishers, Gioi Publishers, 2010.

[106] S. Chatrchyan *et al.*, “Azimuthal anisotropy of charged particles at high transverse momenta in PbPb collisions at $\sqrt{s_{NN}} = 2.76$ TeV,” *Phys. Rev. Lett.*, vol. 109, p. 022301, 2012.

[107] S. Chatrchyan *et al.*, “Measurement of the elliptic anisotropy of charged particles produced in PbPb collisions at $\sqrt{s}_{NN}$=2.76 TeV,” *Phys. Rev.*, vol. C87, no. 1, p. 014902, 2013.

[108] A. M. Sirunyan *et al.*, “Constraints on the chiral magnetic effect using charge-dependent azimuthal correlations in pPb and PbPb collisions at the LHC,” 2017.

[109] B. I. Abelev *et al.*, “Azimuthal charged-particle correlations and possible local strong parity violation,” *Phys. Rev. Lett.*, vol. 103, p. 251601, 2009.

[110] I. Selyuzhenkov and S. Voloshin, “Effects of non-uniform acceptance in anisotropic flow measurement,” *Phys. Rev. C*, vol. 77, p. 034904, 2008.

[111] A. Bilandzic, C. H. Christensen, K. Gulbrandsen, A. Hansen, and Y. Zhou, “Generic framework for anisotropic flow analyses with multiparticle azimuthal correlations,” *Phys. Rev. C*, vol. 89, p. 064904, 2014.

[112] J. Adam *et al.*, “Event shape engineering for inclusive spectra and elliptic flow in Pb-Pb collisions at $\sqrt{s_{NN}} = 2.76$ TeV,” *Phys. Rev. C*, vol. 93, p. 034916, 2016.

[113] S. Chatrchyan *et al.*, "Centrality dependence of dihadron correlations and azimuthal anisotropy harmonics in PbPb collisions at $\sqrt{s_{NN}} = 2.76$ TeV," *Eur. Phys. J. C*, vol. 72, p. 2012, 2012.

[114] Z.-W. Lin, C. M. Ko, B.-A. Li, B. Zhang, and S. Pal, "A multi-phase transport model for relativistic heavy ion collisions," *Phys. Rev. C*, vol. 72, p. 064901, 2005.

[115] G.-L. Ma and B. Zhang, "Effects of final state interactions on charge separation in relativistic heavy ion collisions," *Phys. Lett. B*, vol. 700, p. 39, 2011.

[116] G. J. Feldman and R. D. Cousins, "A unified approach to the classical statistical analysis of small signals," *Phys. Rev. D*, vol. 57, p. 3873, 1998.

[117] S. Acharya *et al.*, "Constraining the magnitude of the Chiral Magnetic Effect with Event Shape Engineering in Pb-Pb collisions at $\sqrt{s_{\mathrm{NN}}} = 2.76$ TeV," *Phys. Lett. B*, vol. 777, p. 151, 2018.

[118] A. M. Sirunyan *et al.*, "Challenges to the chiral magnetic wave using charge-dependent azimuthal anisotropies in pPb and PbPb collisions at $\sqrt{s_{_{NN}}}$= 5.02 TeV," 2017.

[119] A. Bilandzic, R. Snellings, and S. Voloshin, "Flow analysis with cumulants: Direct calculations," *Phys.Rev.*, vol. C83, p. 044913, 2011.

[120] C. Adler *et al.*, "Elliptic flow from two and four particle correlations in Au+Au collisions at s(NN)**(1/2) = 130-GeV," *Phys.Rev.*, vol. C66, p. 034904, 2002.

[121] W.-T. Deng, X.-G. Huang, G.-L. Ma, and G. Wang, "Test the chiral magnetic effect with isobaric collisions," *Phys. Rev. C*, vol. 94, p. 041901, 2016.

[122] R. J. M. Snellings, H. Sorge, S. A. Voloshin, F. Q. Wang, and N. Xu, “Novel rapidity dependence of directed flow in high-energy heavy ion collisions,” *Phys. Rev. Lett.*, vol. 84, pp. 2803–2805, 2000.

[123] L. Adamczyk *et al.*, “Beam-Energy Dependence of the Directed Flow of Protons, Antiprotons, and Pions in Au+Au Collisions,” *Phys. Rev. Lett.*, vol. 112, no. 16, p. 162301, 2014.